Mechanical and Optical Characterization of a Tissue Surrogate Polymer Gel

by

Raj Krishna Abhiram Pasumarthy

A thesis submitted to the Graduate Faculty of
Auburn University
in partial fulfillment of the
requirements for the Degree of
Master of Science

Auburn, Alabama
August 6, 2016

Keywords: experimental mechanics, optical metrology, mechanical properties, stress concentration, puncture mechanics

Approved by

Hareesh V Tippur, Chair, McWane Professor of Mechanical Engineering
Jeffrey C Suhling, Quina Distinguished Professor of Mechanical Engineering
Robert L Jackson, Professor of Mechanical Engineering

Abstract

Hydrogels and polymer gels are widely used for simulating the mechanical response of human or animal tissue to understand the effects of trauma on organs, design body armor, detect tumors robotically, simulate surgical procedures and test the effectiveness of firearms. Polymer gels are preferred to hydrogels for environmental stability, low cost, and ease of altering sample composition, shape and dimensions and do not have moisture evaporation issues. Motivated by these, a transparent polymer gel is studied in this work as a tissue simulant.

The composition of the polymer gel is first assessed using FTIR spectroscopy. This is followed by mechanical characterization studies comprising of tension, compression and shear tests at different crosshead speeds to evaluate strain rate dependency. Uniaxial tension tests are conducted to evaluate stress-strain responses and failure properties. Highly compliant nature of the gel, however, demands special specimen sizing and end tabbing techniques to prevent premature specimen damage. Digital Image Correlation method is used for measuring two orthogonal strains during tensile tests. The stress-strain data are modeled as Mooney-Rivlin, Neo-Hookean and Yeoh hyperelastic materials. Compression tests are performed as well on cylindrical samples for completeness. The gel elastic modulus is found to increase modestly (103 to 141 kPa) over strain rates 0.0004 to 0.04 /sec whereas the Poisson's ratio is in the range 0.46 to 0.48. However, both failure stress and failure strain increased by nearly 100% in the same range of strain rates, the latter being unexpected relative to conventional engineering materials. Shear tests are also conducted to obtain the corresponding shear moduli and to independently compare with the ones from tension tests.

Optical transparency of the polymer gel is a feature useful for visualization and quantification of mechanical fields using full-field optical techniques. Accordingly, its

elasto-optical constant that accounts for the combined density changes and Poisson effects is quantified using Digital Gradient Sensing (DGS) method by measuring angular deflections of light rays propagating through a diametrically compressed circular gel disk. The elasto-optical constants ranged from -1.47 to -1.18 mm^2/N over the strain rates considered. The feasibility of studying stress concentration effects using DGS is demonstrated by performing experimental and numerical simulations on a classical Flamant loading configuration.

Lastly, preliminary work towards understanding the mechanics of needle-tissue surrogate gel interaction is carried out at two different insertion/retraction rates. Significant strain rate effects and hysteresis are observed both in terms of measured stress gradients and global force measurements. During needle insertion, forces increased monotonically and are compressive. During retraction, however, forces not only decreased but turned tensile before becoming zero. Non-uniform stress distribution in the vicinity of the needle with a high concentration of stresses is evident from the optical measurements.

Acknowledgements

I would like to express my deepest and sincere gratitude to my advisor, Dr. Hareesh V. Tippur, for his academic guidance, support and motivation throughout my thesis program. I consider the time I spent in the "Failure characterization and optical techniques" laboratory to be of immense value for my personal and professional advancement. I thank Dr. Jeffrey C. Suhling and Dr. Robert L. Jackson for their willingness to serve on my committee.

I gratefully acknowledge grants from NSF (grant # CMMI - 1232821) and ARO (grant # W911NF-12-1-0317) for extending financial support for this research. I would like to thank my colleagues Balamurugan, Amith, Robert, Austin and Chengyun for their support and encouragement during my research.

Lastly, and most of all, I would like to thank God Saibaba for his blessings and express my gratitude to parents, sister and friends for their enduring love and immense moral support to successfully complete my thesis. I dedicate this thesis to them.

Table of Contents

List of Tables

List of Figures

Chapter 1: Introduction

1.1 Motivation

Hydrogels and polymer gels are often used to mimic the mechanical behavior of human or animal tissue. In the field of terminal ballistics, it is used to test the effectiveness of firearms [1]. In wound ballistics, which is a part of terminal ballistics since the mid-19th century beginning with the treatment of battlefield injuries [2], the focus is on the effect of projectiles that penetrates living tissues [3]. Blunt trauma causes significant adverse effects on thoracic organs, and understanding these effects is important in the design of protective equipment such as body armor used in impact events. Tissue surrogates such as ballistic gels play a vital role in mimicking the effects on soft tissue subjected to extreme pressure and velocity [4, 5]. Gels can also be used as breast tissue surrogate material to automate early detection of cancer [6].

The wildlife management and hunting communities have also developed broad knowledge about adequate ammunition to incapacitate animals [7]. The composition of the gel selected is usually based on the natural tissue whose response is to be studied and behavior to be replicated. Tissue simulant (or tissue phantom) should be picked in such a way that it has the ability to reproduce the physical effects of bullet–tissue interaction and should stop the bullet at the same depth as a living tissue would. Gelatin can be formulated to simulate various types of soft tissues. Although it can simulate the density and viscosity of

a living tissue, it lacks the structural complexity and heterogeneity of natural tissue. In addition, the human and animal anatomy contains organs, muscle, and fat supported by a skeleton. Despite this, gels are widely employed as tissue surrogates instead of the actual biological tissues [8].

Polymer gels are preferred over hydrogels which contain water in the composition. Hydrogels pose many difficulties such as short shelf life as they are associated with evaporation problems even at room temperature and/or during long duration experiments. Further, hydrogels typically need low temperature storage. As observed by Moy et al. [9], testing hydrogels pose other problems such as oozing from the gel during experiments complicating the test procedures. Unlike hydrogels, polymer gels offer environmental stability, easy storage and longer shelf life. Further, some polymer gels can be readily melted and reused.

Polymer gels have many more applications and some are shown in the figure below. Figure 1.1(a) shows a gel block into which bullets of different sizes have been fired into. The penetrated block and the cavities formed as a result of a bullet entering the rectangular gel block from one side, traveling the entire length and leaving from the other side are evident. The cavities formed by the bullet in the gel block are studied to predict deformation in a tissue which has similar properties. Figure 1.1(b) shows a structure made of ballistic polymer gel which can be used for testing and simulating human torso. Figure 1.1(c) shows the application of polymer gel to simulate the behavior of human tissue when a hypodermic needle penetrates the tissue.

(a)

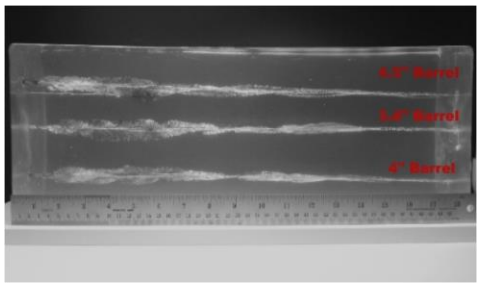

(c)

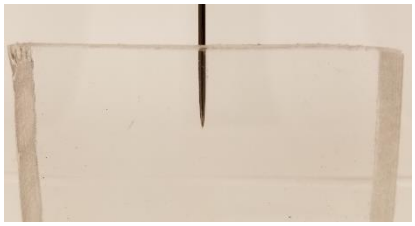

(b)

Figure 1.1: Some examples of ballistic gel applications: (a) Ballistic gel block used in fire arm testing, (b) Ballistic gel torso used for body armor development, (c) Needle penetrated into polymer gel to simulate tissue puncture.

Mechanical and optical characteristics of ballistic polymer gels are generally proprietary or unknown for them to be useful as tissue surrogates in scientific investigations. In this research, first the mechanical characterization is performed followed by optical characterization of a commercially procured 20% polymer gel. As the gel studied has superior transparency, full-field optical measurement techniques can be utilized for visualizing and quantifying mechanical quantities when subjected to loads. Accordingly, the feasibility of a Digital Gradient Sensing (DGS) method sensitive to angular deflections of light rays passing through the transparent polymer gel subjected to mechanical loading are measured and related to the stress gradients for future adaptation of the methodology for detailed experimental mechanics study of polymer gels as a tissue surrogate.

1.2 Literature Review

Tensile testing of soft gels requires substantial effort in gripping and avoiding local failure if traditional techniques are used. Subhash et al. [10] employed a shoulder supported tensile specimen as shown in Fig. 1.2 (top) to study Agarose gels. Tension samples with concentrations of 1.5%, 2.0%, 2.5%, 3.0%, 3.5% and 4.0% (w/w) were prepared from a mixture of DNA analysis-grade agarose powder and deionized water. A random speckle pattern was created by using MATLAB software and transferred onto the gage area of the

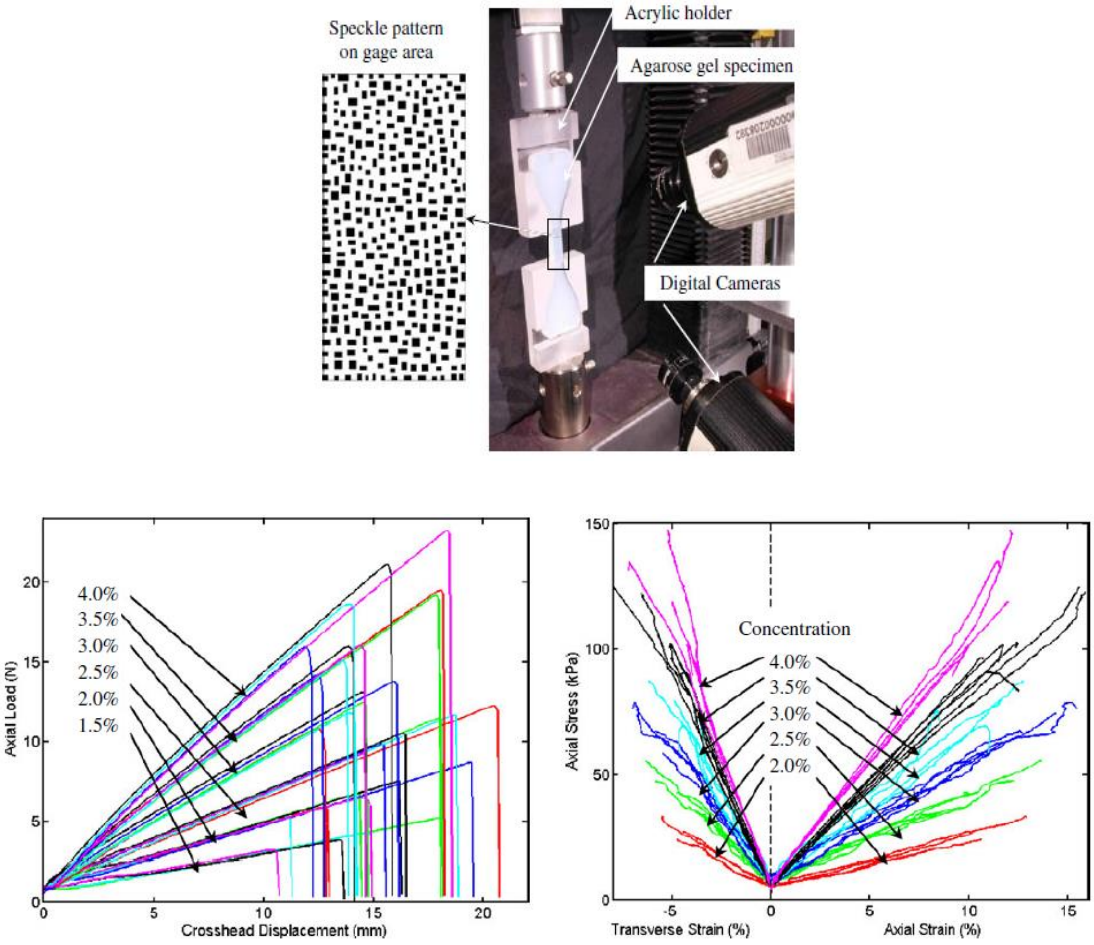

Figure 1.2: Experimental setup for tension tests (top), load vs displacement and axial stress vs strain responses (bottom) for Agarose gel (Reproduced from Ref. [10])

specimen. Digital Image Correlation was performed to obtain both axial and lateral strains over the entire field. It was observed that both tensile strength and modulus of the gel increased linearly with an increase in agarose concentration, see Fig. 1.2 (bottom).

A rigid inclusion (steel sphere) embedded in a tissue phantom made of Knox brand gelatin and water (5:3 ratio) to simulate lesion (breast cancer) using mechanical indentation

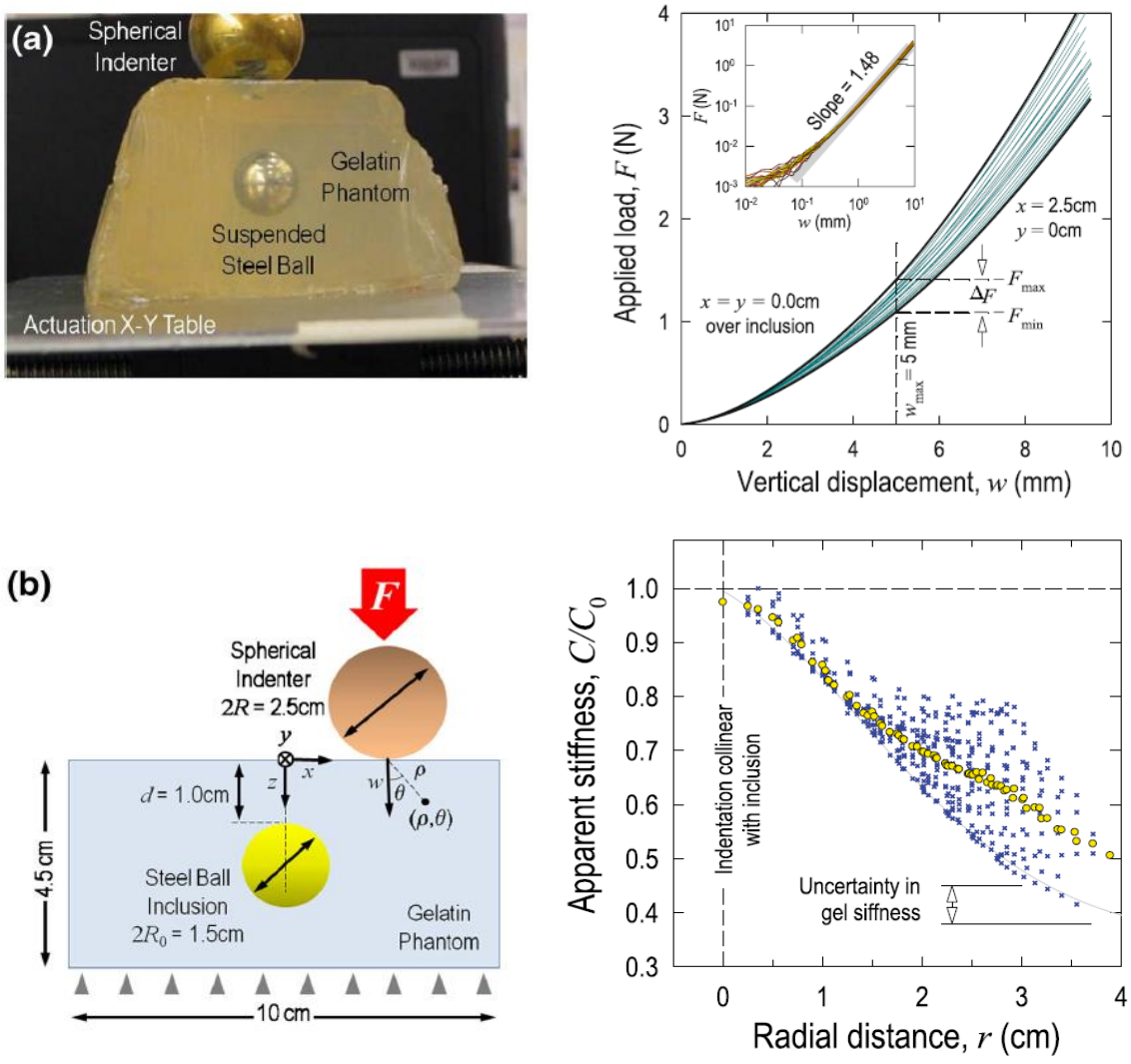

Figure 1.3: Photograph and schematic of phantom gel sample (left), force vs displacement response and normalized stiffness vs radial distance plots (right) (Reproduced from Ref. [9])

is reported in Ref. [9]. An array of indents (2.5 mm steps in the *x*- and *y*-directions) using a rigid indenter were made over an assigned area (50 mm x 50 mm) of the surface of the phantom, while the force, *F*, was measured as a function of instantaneous indentation depth, *w* (up to 10 mm in the *z*-direction). When the local stress field interacted with a sufficiently shallow inclusion, the mechanical response *F*(*w*) yielded an augmented apparent stiffness *C*. The average slope of the logarithmic plot was measured as *n*. If *F*, *w* and *n* are known quantities, then at each (*x, y*) location stiffness *C* can be obtained and normalized with the maximum value C_o exactly on the top of the inclusion i.e., the origin. A 2D spatial map of *C* shows the presence, location, depth, and geometry of the simulated lesion.

Resistance to puncture is vital for elastomeric materials used in protective clothing (e.g., neoprene gloves). This is very important in medical applications where transmission of diseases needs prevention. Rounded tip probes are usually used to test puncture resistance behavior instead of medical needles [11]. As shown in Fig. 1.4, in case of puncture probes, the elastomer punctures occurs suddenly after reaching the failure strain where as it is gradual in case of medical needles. Failure load is high in case of probes compared to the medical needles. The sharpness of medical needles causes a cutting behavior and hence puncture resistance offered is less.

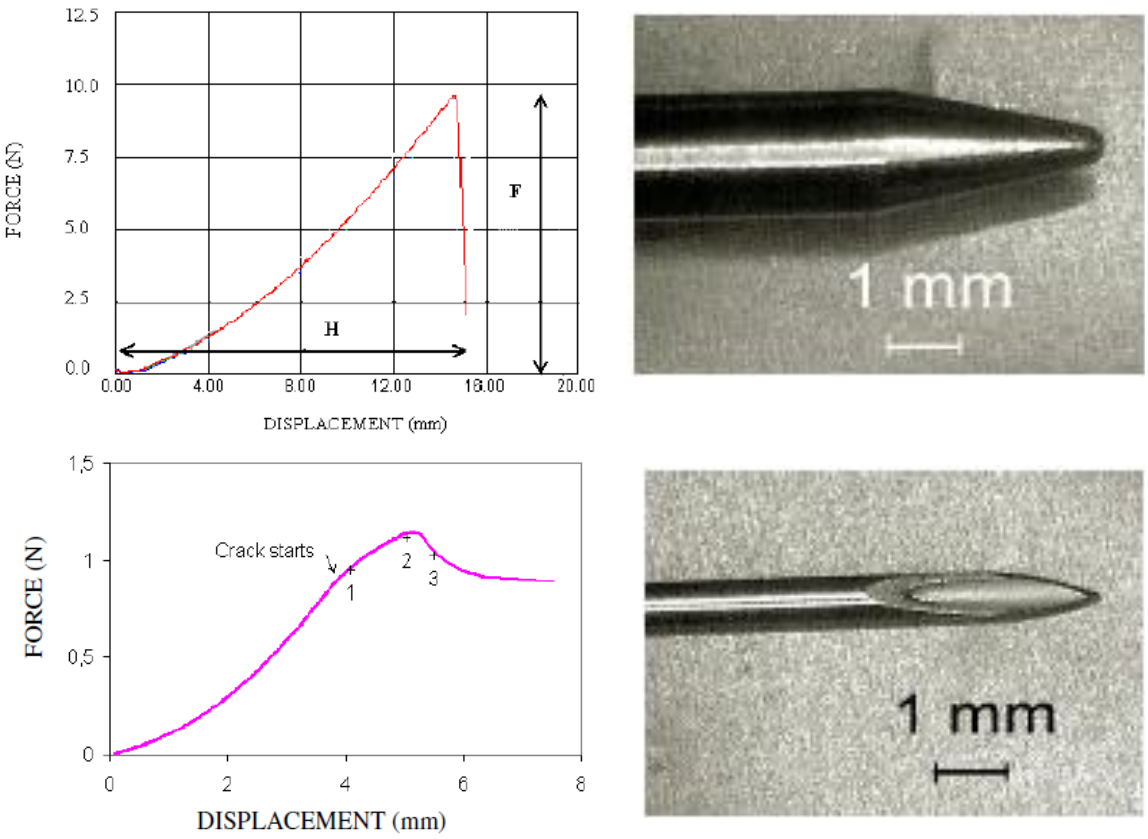

Figure 1.4: Force vs displacement response and photograph of blunt needle (top), force vs displacement response and photograph of medical needle (bottom) (Reproduced from Ref. [11])

Modeling forces during needle insertion into soft tissue with a high degree of positional accuracy is very important to simulate robot assisted surgical procedures [12]. Okamura et al., [13] have used one degree of freedom robot equipped with a load-cell and needle attachment to obtain force data during tests. Percutaneous therapies have a lot of value as they reduce patient discomfort during surgery and also reduce the recovery time [14]. In these situations, as direct visual observation of the area of interest is not possible in real time, accurate positioning of the needle without affecting neighboring regions is very critical. Okamura et al., simulated bovine liver biopsy with needle insertion used to treat tumors. As shown in Fig. 1.5, during needle insertion into bovine liver tissue, multiple

peaks occur in force vs displacement response. First peak corresponds to the initial puncture of the tissue. Subsequent variations in force are due to tissue inhomogeneity and puncture of other interior structures including veins and arteries. They also observed that when the needle is retracted, a drop in the measured force to negative values occurs before becoming zero.

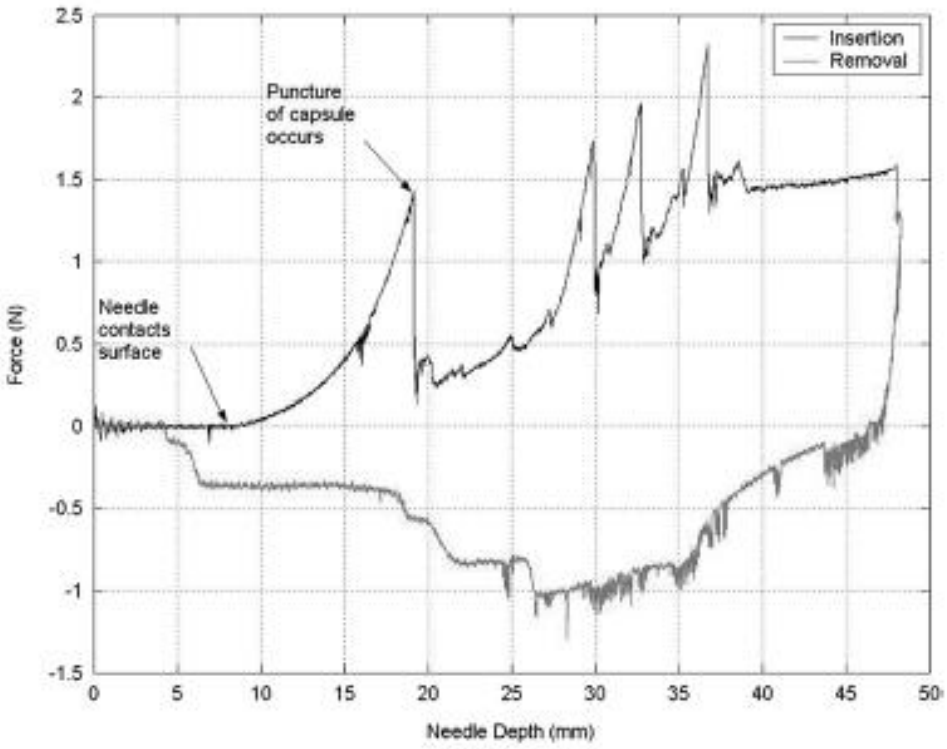

Figure 1.5: Force vs displacement response during needle insertion into bovine liver (left) and photograph of bovine liver (right) (Reproduced from Ref. [13])

A proper understanding of the mechanics of needle-tissue interaction is equally important to optimize needle design, achieve accurate robotic steering and automation of surgical procedures. Shan et al. [15] compared the force vs displacement responses of PolyVinyl Alcohol (PVA) hydrogel and porcine liver as they both have similar biomechanical response and microstructure [16]. In their work, as shown in Fig. 1.6, PVA phantom was placed in a test chamber and a horizontal actuator equipped with a six DOF

force/torque sensor was used to measure forces acting on the needle. A servomotor was used to drive the needle at different velocities.

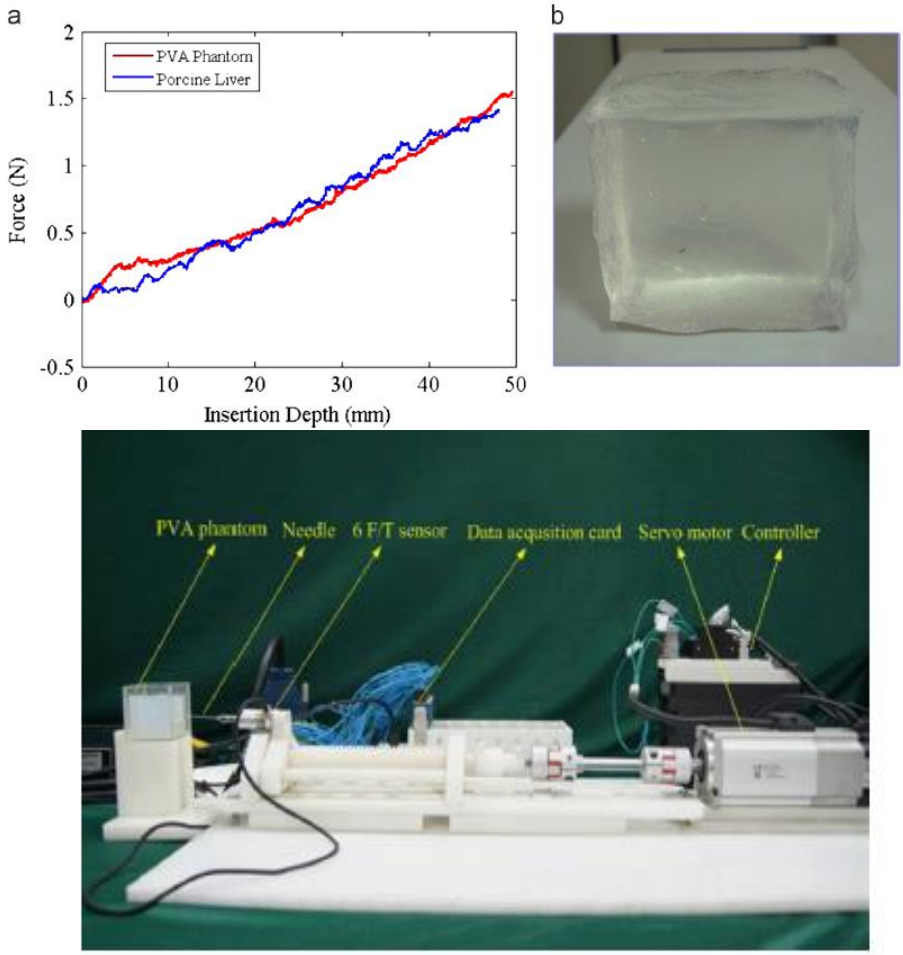

Figure 1.6: Force vs displacement responses and photograph of PVA phantom (top), experimental setup (bottom) (Reproduced from Ref. [15])

The effect of needle sizes, shapes and tip geometries on cutting force vs displacement response of PVA phantom is shown in Fig. 1.7. Larger needles increase the cutting forces. Different needle tip shapes have different distribution of forces at the tip of the needle. The stiffness is observed to increase remarkably with the diameter. The fluctuations in force vs displacement response increased with increase in the bevel angle.

The blunt needle tip initially has higher stiffness whereas conical tip has higher insertion force growth rate.

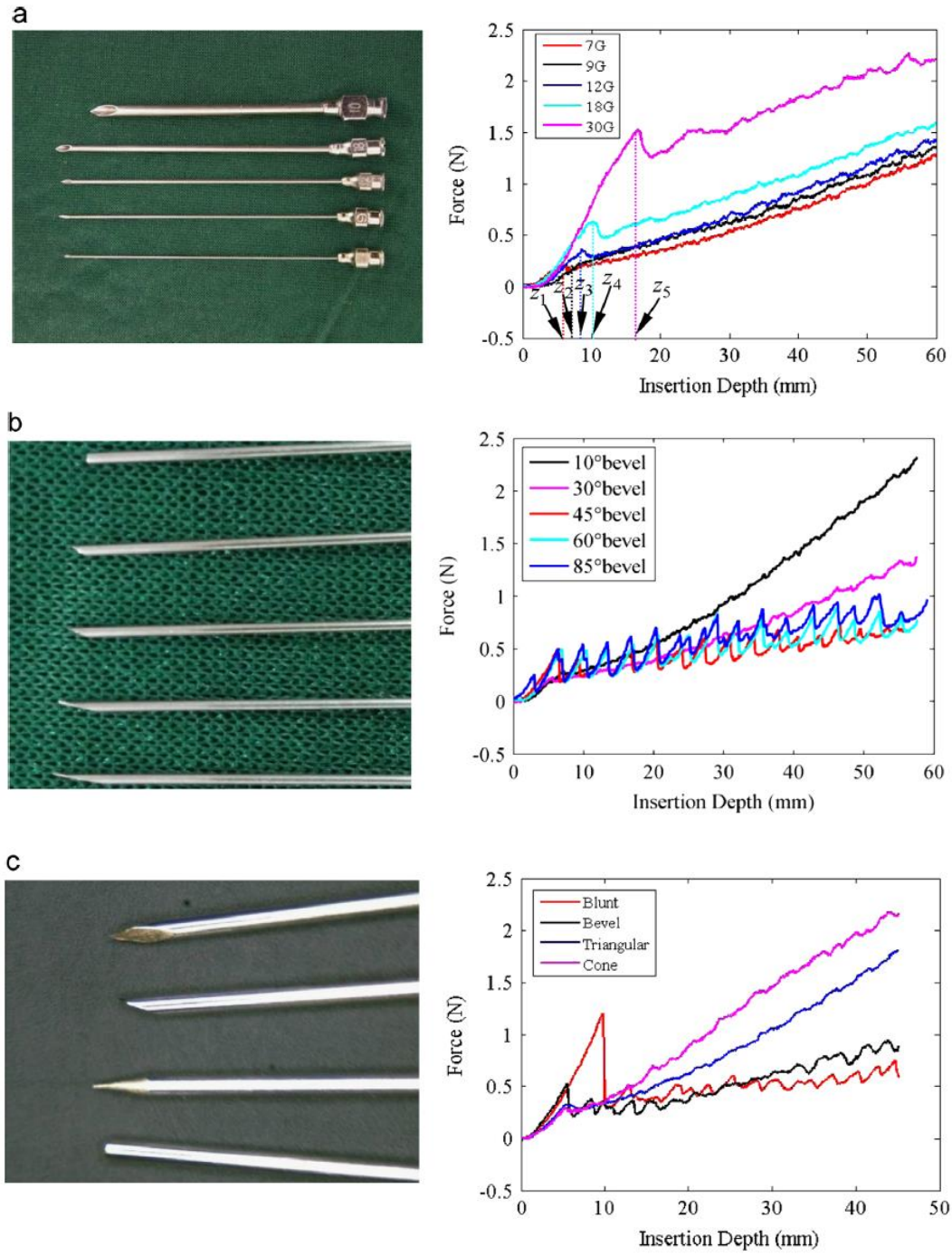

Figure 1.7: Insertion forces vs displacement responses at 4 mm/sec with needles of different (a) diameters, (b) bevel angle, (c) tip shapes (Reproduced from Ref. [15])

In addition to the size and shape of the needle tip, tissue anisotropy has been shown to have significant influence on needle-tissue interaction forces during penetration. According to Mahvash et al., a needle traversing an internal tissue can cause rupture if the stiffness of the new tissue layer is significantly lower than the current tissue layer [17]. As shown in Fig. 1.8, out of the three force vs displacement responses for trocar needle insertion into pig liver at 1 mm/sec, there is variation in rupture force due to tissue inhomogeneity. A pig heart was considered in another analysis and punctured at 1 mm/sec with trocar and bevel type of needles using a linear actuator. A difference in the force response between both the two needle types was observed similar to the observation made by Shan et al. [15].

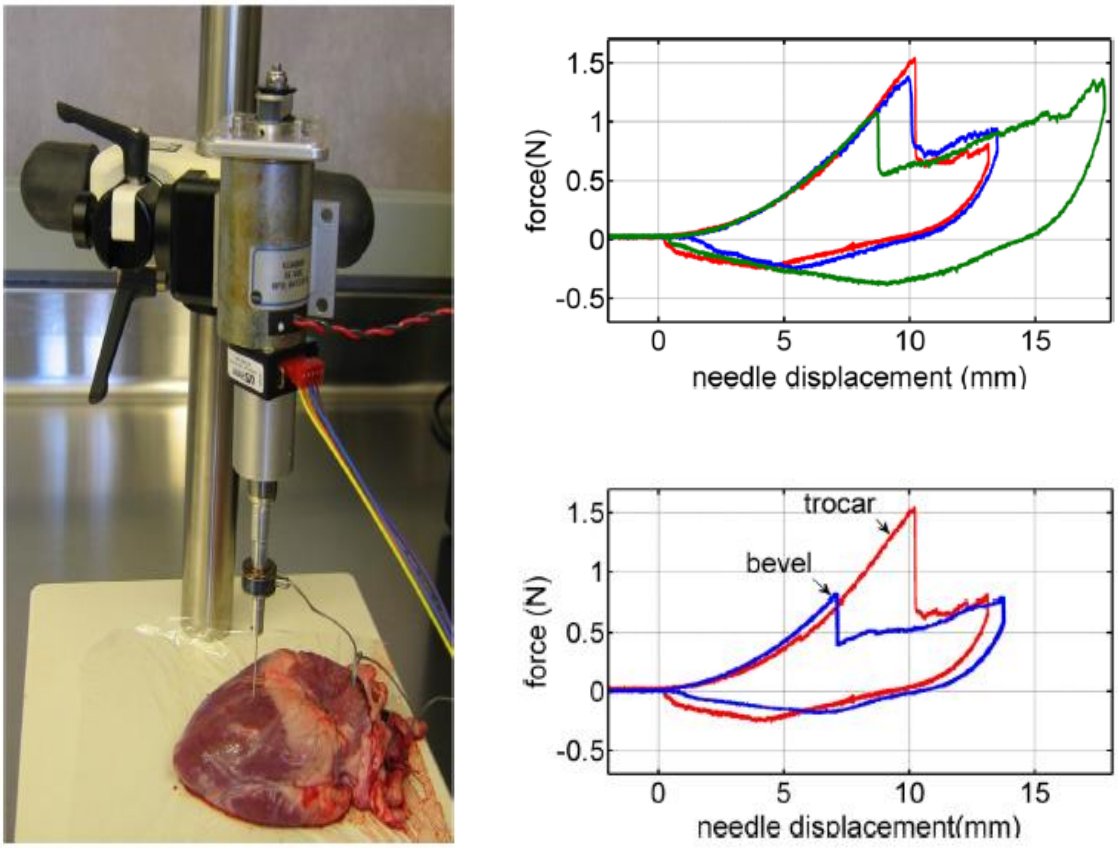

Figure 1.8: Experimental setup with linear actuator and pig heart (left), force, velocity and accelerations responses with respect to time (Reproduced from Ref. [17])

Van Gerwen et al. categorized needle insertion into soft tissues into four stages (Fig. 1.9) based on the needle tip position relative to the tissue boundary [18]. In the first stage, Fig. 1.9(a), needle tip has not yet contacted the tissue. When the needle traverses further toward a tissue, needle tip contacts the tissue as in Fig. 1.9(b). Further movement of the needle results in displacement of the boundary without penetration. This is also known as tenting [19]. As the needle is displaced further into the tissue, the stresses at the tip of the needle exceed a critical value [20]. This initiates a crack in the tissue and the needle will start to penetrate the tissue as in Fig. 1.9(c). The crack growth will be stable or unstable depending on the local tissue properties, tissue toughness and strain energy stored due to deformation. In the fourth stage, Fig. 1.9(d), transition in contact between the tissue and the needle occurs from its tip to the shaft resulting in an increase in the axial force as

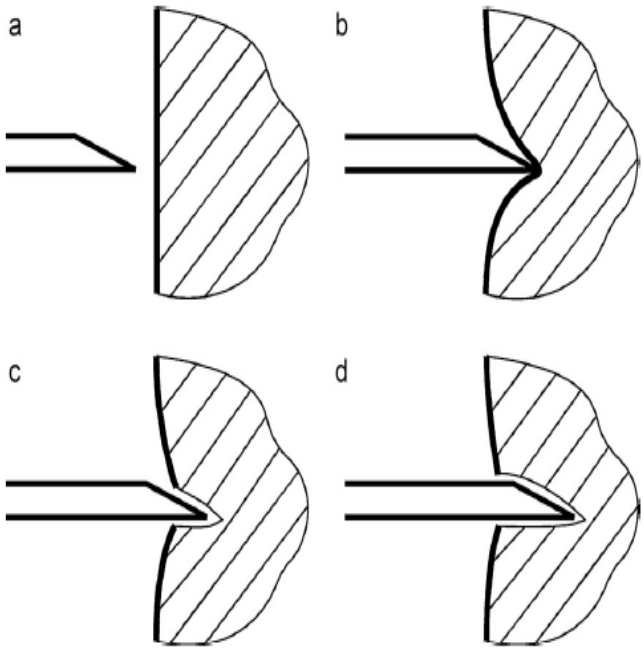

Figure 1.9: Basic stages in needle insertion, (a) no interaction, (b) boundary displacement, (c) tip insertion, (d) tip and shaft insertion (Reproduced from Ref. [18])

a hole in the tissue is wedged open. Contact area between the tip and the tissue is almost constant whereas it increases between the shaft and the tissue. Force is nearly constant after this unless there is inhomogeneity in the tissue as observed by Hing et al. with porcine liver [21]. They have also [21, 22] assumed that the force during insertion of the needle into a porcine liver includes both frictional and cutting forces which increases and reaches a peak value. When the needle is retracted, force due to friction between the needle and tissue alone needs to be dealt with as puncture has already occurred. When this force is subtracted from the insertion force, cutting forces can be isolated.

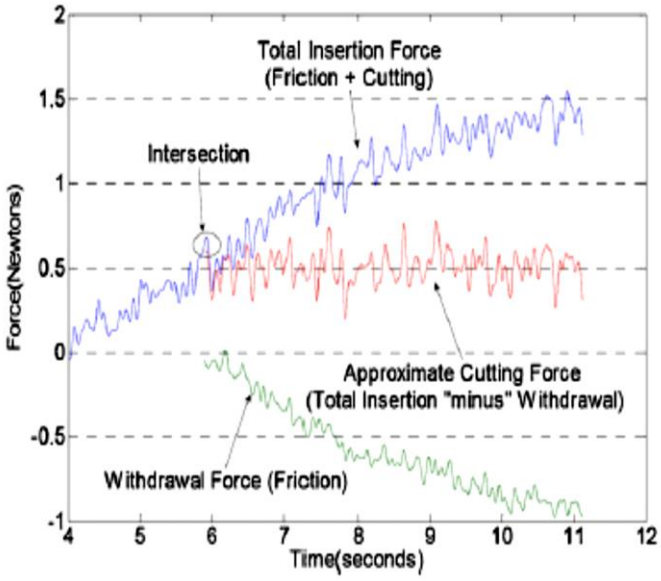

Figure 1.10: Cutting force estimation by subtracting withdrawal force from insertion force at 13 mm/sec in porcine liver ex vivo (Reproduced from Ref. [21])

DiMaio et al. used axial force measurement and tissue displacement responses in combination with finite element models to estimate load distribution along the length of the needle [23]. They used a 17 G Tuohy needle to puncture Poly Vinyl Chloride (PVC) phantom at different velocities as shown in Fig. 1.11. The load distribution was uniform along the shaft of the needle except for a peak value near the tip of the needle. According

to Van Gerwen et al. [18] this peak force might be due to cutting or rupture behavior at the tip and the uniform part is due to friction between the phantom and the needle.

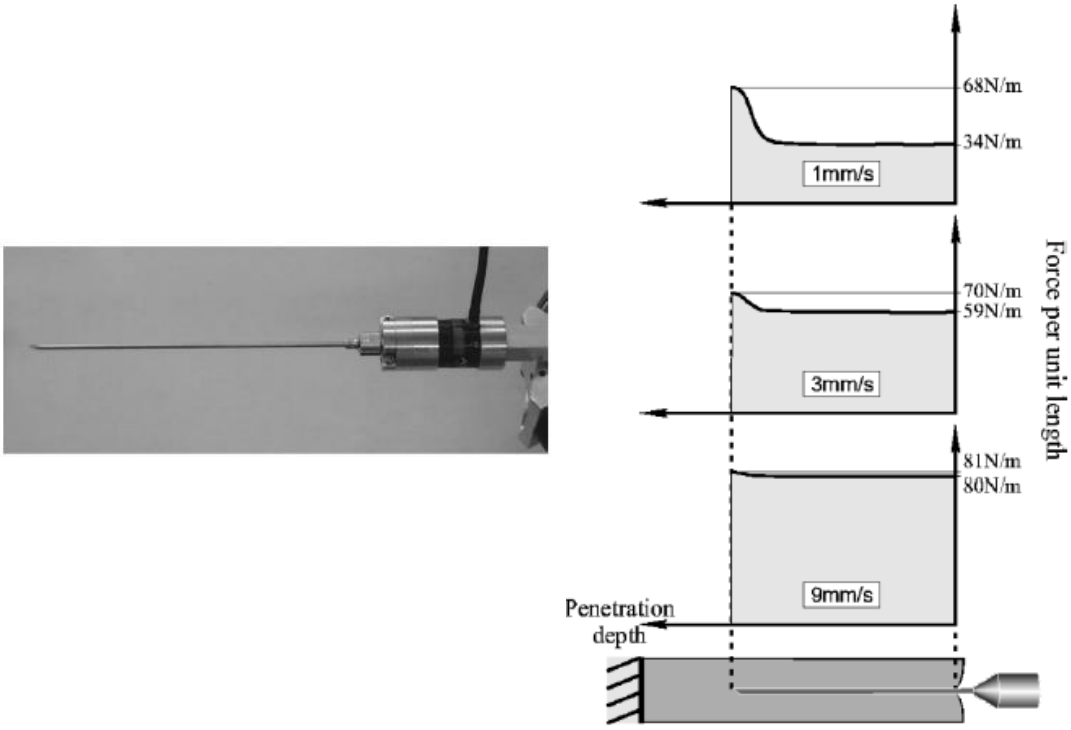

Figure 1.11: Photograph of 17 G Tuohy epidural needle (left) and estimated force distribution along the needle shaft during insertions in Poly Vinyl Chloride (PVC) phantom at various velocities (right) (Reproduced from Ref. [23])

1.3 Objectives

As evident from the literature review, there is significant interest as well as numerous gaps and challenges yet to be addressed for understanding the mechanical behavior of tissue surrogates and the mechanics of needle-tissue interaction. The works in the literature generally consider global reaction forces and displacements without much information on the local interaction forces/stresses essential for understanding the underlying mechanics. Hence, the primary objective of this thesis is to first mechanically characterize a polymer

gel tissue surrogate, then determine its optical properties to be able to study stress concentration problems and initiate studies on the mechanics of needle-tissue interaction via full-field optical methods. Some of the specific tasks to be tackled are:

- Develop sample preparation methods essential for characterizing mechanical behavior of a transparent polymer gel tissue surrogate material,
- Evaluate the optical and physical characteristics such as refractive index, density of the polymer gel,
- Mechanically characterize the polymer gel by performing tension, compression and shear tests,
- Demonstrate the feasibility of implementing full-field optical methods such as Digital Gradient Sensing (DGS) method to study transparent polymer gel tissue surrogates,
- Perform experiments using DGS to evaluate elasto-optical constant of the polymer gel material,
- Demonstrate DGS for optically studying stress concentration problems in polymer gels by performing (a) line-load acting on the edge of a planar sheet (Flamant problem), and (b) circular cut-out in a tensile sheet,
- Demonstrate the feasibility of using DGS to study needle-gel tissue surrogate puncture.

1.4 Thesis Layout

This thesis is organized into ten chapters including the current one. Chapter 2 includes details regarding material description, sample preparation techniques to obtain transparent polymer gel specimens with good surface finish and working principle of Digital Image Correlation (DIC) method. Chapter 3 presents information about experimental setup and special gripping ideas for tension tests. The governing equations of hyperelastic models to extract the tensile modulus and to determine the Poisson ratio are also included in this chapter. Chapter 4 consists of shear tests to extract the shear modulus and compare with the counterpart obtained from the tensile modulus and Poisson's ratio. Chapter 5 includes details on the compression experiments to determine the modulus of the polymer gel in the compressive loading configuration.

Chapter 6 presents the application of DGS to disk under diametral compression problem and evaluate the optical properties including its elasto-optical constant and refractive index. Chapters 7 and 8 present particulars about the application of DGS technique to study stress concentration problems such as a line-load acting on the edge of a planar sheet and a circular cut-out in a tensile sheet, respectively. Chapter 9 shows the feasibility of employing DGS method to study puncture behavior in the polymer gel phantom due to needle insertion. Chapter 10 provides major conclusions of this work and some potential future directions for research.

Chapter 2: Materials and Methods

In this chapter, details regarding the chemistry of the polymer gel and tests used for this purpose are described first. Then, sample preparation steps are discussed in detail. Subsequently, properties of the gel such as its density and refractive index are determined using conventional techniques. Lastly, particulars about the working principle of Digital Image Correlation (DIC) used for mechanical characterization are provided.

2.1 Material Description

The material employed in this research in a ballistic polymer gel which has superior characteristics when compared to hydrogels as detailed in the previous chapter. Fourier Transform InfraRed (FTIR) spectroscopy was carried out to estimate the composition of the polymer gel. (FTIR is a technique used to obtain an infrared spectrum of absorption or emission of a solid, liquid or gas [24, 25] whereas spectroscopy is the study of interaction of matter with electromagnetic radiation. Typically the infrared spectrum of a sample is compared to a bank of reference spectra of known substances to determine the composition of the sample tested. As shown in Fig. 2.1, the polymer gel used in this work had a best match with Tygon soft tubing compound which is a clean, flexible material and has good chemical resistance. Tygon has many applications and is widely used in dialysis equipment, chemo therapy, drug delivery, electrical insulation, adhesive dispensing, fertilizer and pesticide dispensing.

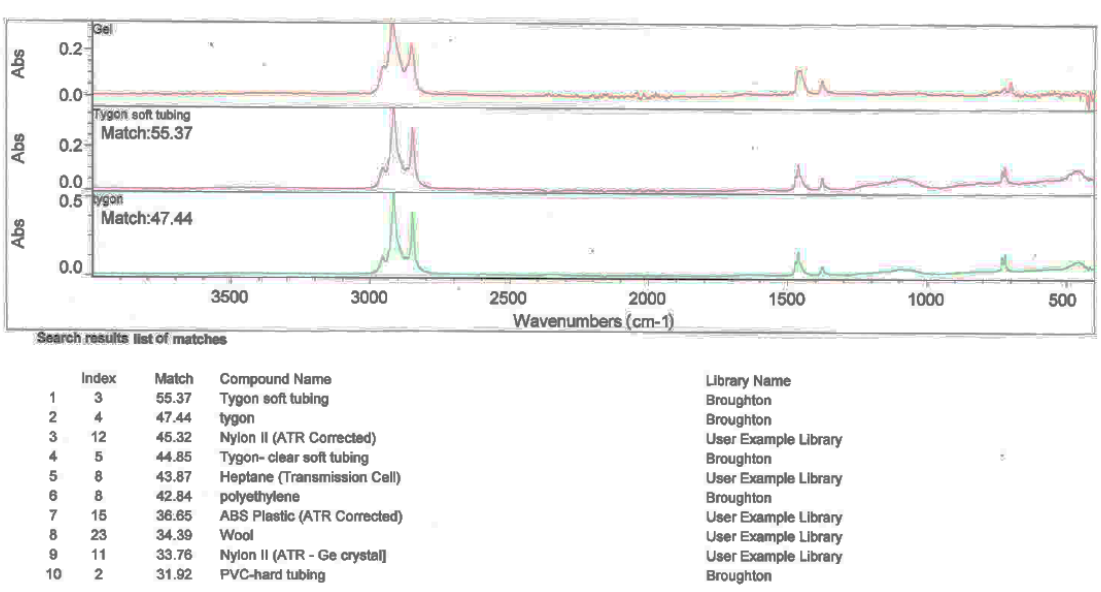

	Index	Match	Compound Name	Library Name
1	3	55.37	Tygon soft tubing	Broughton
2	4	47.44	tygon	Broughton
3	12	45.32	Nylon II (ATR Corrected)	User Example Library
4	5	44.85	Tygon- clear soft tubing	Broughton
5	8	43.87	Heptane (Transmission Cell)	User Example Library
6	8	42.84	polyethylene	Broughton
7	15	36.65	ABS Plastic (ATR Corrected)	User Example Library
8	23	34.39	Wool	User Example Library
9	11	33.76	Nylon II (ATR - Ge crystal)	User Example Library
10	2	31.92	PVC-hard tubing	Broughton

Figure 2.1: Fourier Transform InfraRed (FTIR) spectrum of polymer gel with best match with Tygon soft tubing material.

2.2 Sample Preparation

Commercially available 20% polymer gel block was purchased (Clear Ballistics, LLC, AR). Based on the size and number of samples to be prepared, small chunks of polymer gel were cut from the block and placed in a glass beaker (Fig. 2.2(a)). The beaker was heated to 110^{o}C for 2 to 3 hours to melt the gel uniformly (Fig. 2.2(b)). Rectangular molds made of polycarbonate and coated with a mold release agent Frekote NC 770 were prepared while the gel was being melted. The mold release was recommended by the manufacturer as it would not contaminate the polymer gel. The application of the mold release agent was vital as it allowed the polymer gel removal easily from the mold without tears and other type of surface damage. Duct tape and binder clips were used to seal the mold to avoid leakage of molten polymer gel during cooling. Spacers, also made of strips

of polycarbonate, were used to achieve uniform thickness and prevent squeezing of the gel when clamped. The thickness of the spacers used were same as the desired thickness of the samples. After pouring the molten polymer into the mold, it was placed back in the vacuum oven for degasing. In this process, air bubbles trapped in the mold were released using the vacuum pump by creating a negative pressure of -1 atm. However, degasing was done intermittently to minimize gel overflow from the mold at 110^{o}C. The resulting gel sheet, Fig. 2.2(c), is free from trapped air bubbles. It was cooled for 8 hours at room temperature and then gel sheet was separated from the mold. A Proxxon thermocut hot-wire cutter was used to cut samples of required shape as shown in Fig. 2.2(d). Alternatively, heated foil

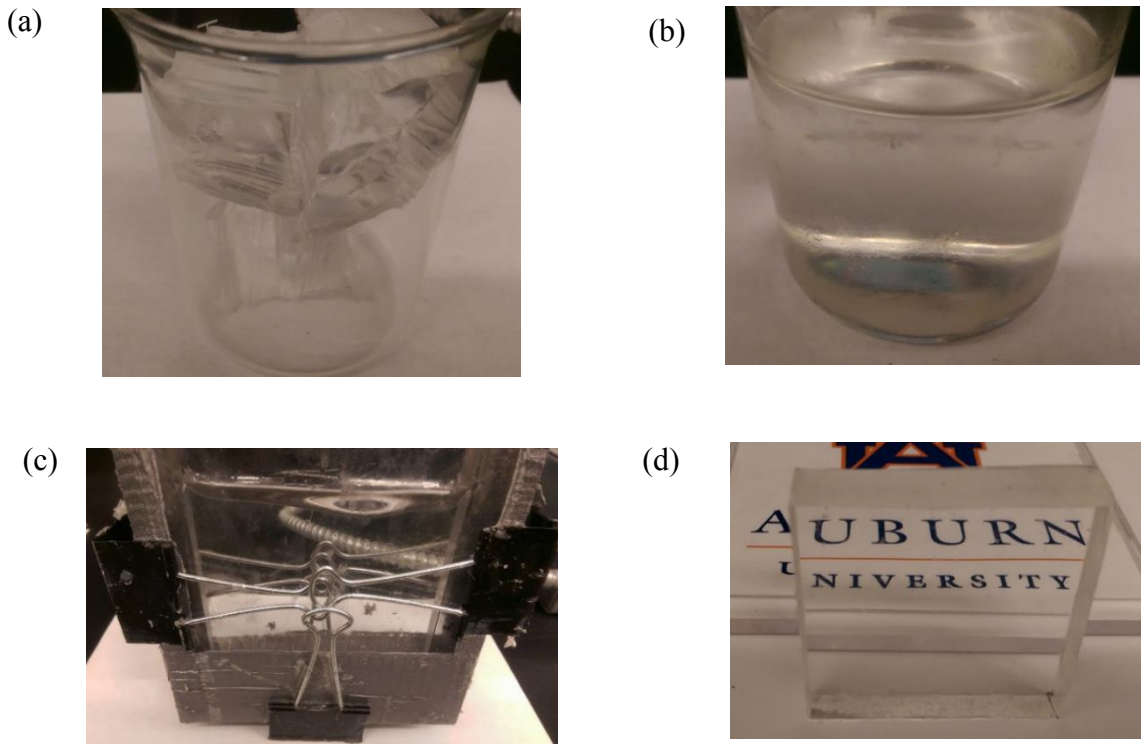

Figure 2.2: (a) Small pieces of polymer gel cut from large block and placed in a beaker, (b) Polymer gel in molten form after heating in an oven, (c) Polycarbonate mold with molten polymer gel, (d) Transparent rectangular polymer gel block cut with good right angled faces using a wire cutter.

strips or hollow tubes were also used to obtain samples of different shapes needed during this research.

2.3 Mass Density

10% and 20% ballistic polymer gel blocks were extracted and their mass and volume were measured. This information was used to determine the density of the polymer gel. The values of density for both 10 % and 20 % ballistic polymer gels are tabulated as shown below:

Gel	Density, ρ (kg/m^3)
10 %	844.4
20 %	866.7

Table 2. 1: Density values for 10 % and 20 % ballistic polymer gels.

2.4 2D Digital Image Correlation (DIC) using ARAMIS:

The ARAMIS 2D Digital Image Correlation (DIC) software was employed for performing optical measurements. It involves a random speckle pattern applied to the surface of the object to create unique identifiable optical features. This speckle pattern is captured by a digital camera before and after deformation of the object. The pattern recorded under no-load conditions serves as the reference (undeformed) image. When load is applied on the sample, the speckle pattern is distorted and is photographed as the

deformed image. The reference and deformed images are correlated, during which features or speckles present on an object are identified and their relative movements are tracked as displacements or deformations. For this purpose, each digitized image consisting of pixels is divided into 'facets' or 'sub-images' comprising of a user-defined group of pixels. The images contain information about the gray scale distribution (say, as 8 bit or 0-255 levels, or 10 bit 0-1023 levels) on the specimen surface in a discrete form at each pixel location. While correlating the images, for every sub-image (intensity distribution) in the undeformed or reference image, the corresponding sub-image in the deformed image is

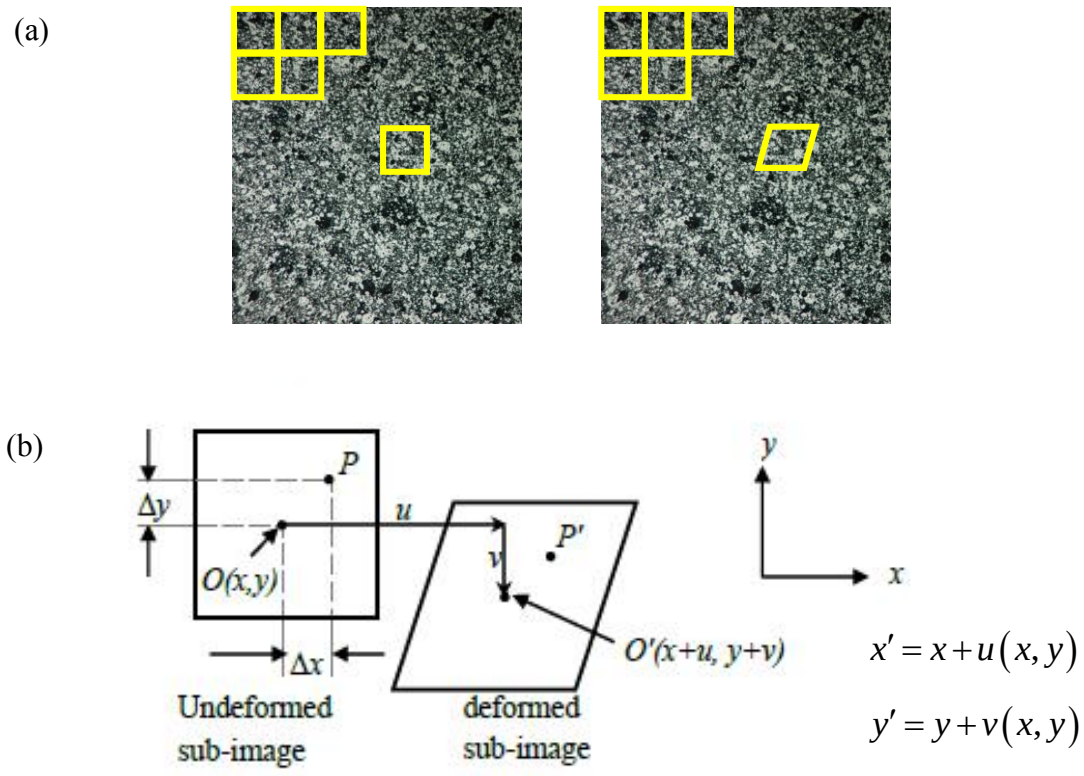

Figure 2.3: Working principle of 2D DIC. (a) Undeformed (left) and deformed (right) speckle images segmented into sub-images (top), (b) Sub-image displacement mapping scheme (bottom)

located by performing grayscale correlation. For example, Fig. 2.3 explains the working principle of 2D DIC. Here two images each of 2048 x 2048 pixels are segmented into an array of sub-images. Based on gray scale intensity distribution, each sub-image in the reference image is located in the deformed image. Due to the application of external load to the object, sub-image in the undeformed state centered at O (x, y) is displaced to O' ($x+u$, $y+v$) by distances u and v in the x- and y-directions, respectively. The displacement components u and v can be obtained by affine transformations.

Chapter 3: Mechanical Characterization – Tensile Behavior

This chapter details tension tests conducted to determine the elastic properties of the polymer gel including tensile elastic modulus and Poisson's ratio. The tensile strength and failure strains are also evaluated. The experimental setup is discussed first. Then the experimental details as well as challenges regarding sample preparation and specimen gripping are discussed. The effect of strain rate is on different measured parameters measured during tests are reported.

3.1 Experimental Setup

A photograph of the experimental setup used for tension tests is shown in Fig. 3.1. It consists of a dog-bone shaped sample coated with speckles, illuminated by LED lamps and photographed using a digital camera. The tension samples glued to polycarbonate end tabs were gripped in an Instron 4465 universal testing machine for performing tests at three different crosshead speeds 0.02, 0.2 and 2 mm/sec.

A Point Grey digital camera (Grasshopper3 GS3-U3-41C6M) fitted with 18-108 mm focal length zoom lens was used to record images. The speckle pattern on the sample surface was illuminated using two cool LED light sources to avoid heating of the sample. The digital camera was focused on the speckles and a reference image (undeformed image) was recorded before the sample was loaded. As the crosshead was displaced, the speckle

images (deformed images) were recorded at regular time intervals (4-10 frames/sec) at different loading rates until the sample failed. The digitized speckle images (2048 x 2048 pixels) recorded at different load levels were correlated with the one corresponding to the reference condition using ARAMIS.

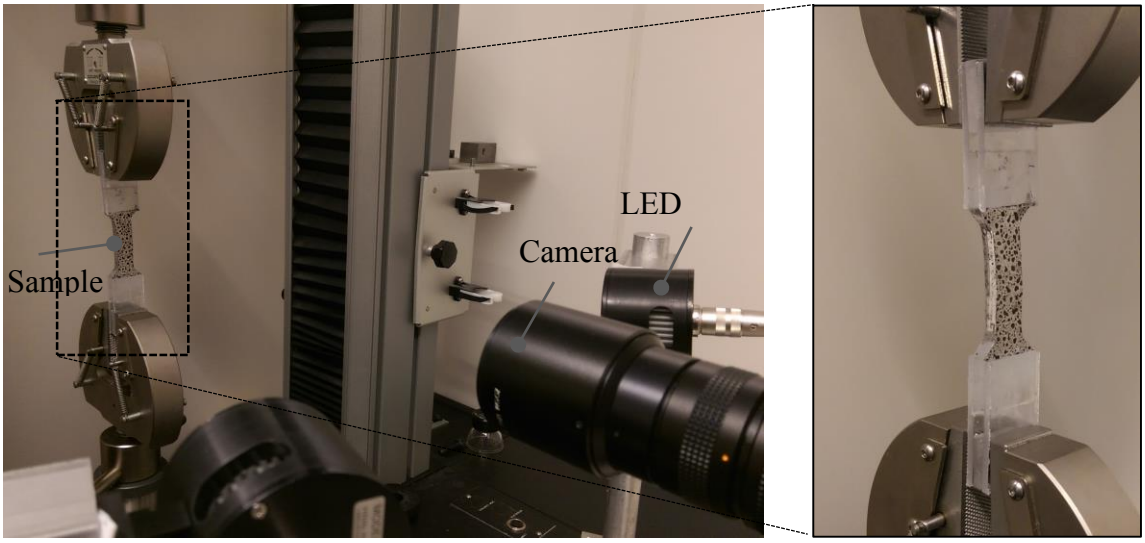

Figure 3.1: Photograph of the experimental setup used for tension test on polymer gel (left), the close-up (right) shows tensile test sample with speckle pattern.

3.2 Sample Preparation

Rectangular gel sheets of required thickness free from air bubbles, with good transparency and surface finish were prepared as discussed in the last chapter. As shown in Fig. 3.2, two aluminum foil strips were machined and bent to dog-bone shape with the

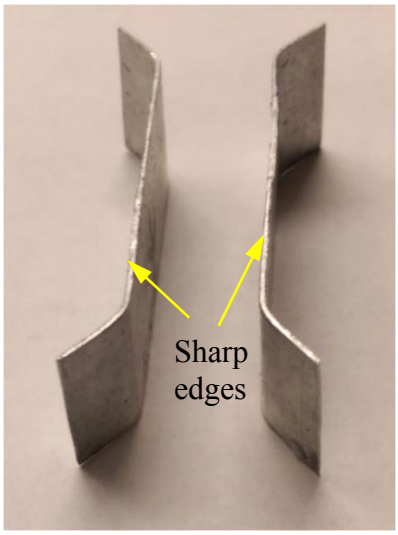

Figure 3.2: Aluminum foils used to cut tensile test samples

required dimensions. One edge of each strip was sharpened like a knife to precisely cut the gel sheet. The foil strips were heated to 80^{o}C in an oven and carefully pressed into the gel sheet in the thickness direction at right angles. As shown in Fig. 3.3, the required dog-bone gel specimens were obtained with square edges and good surface finish.

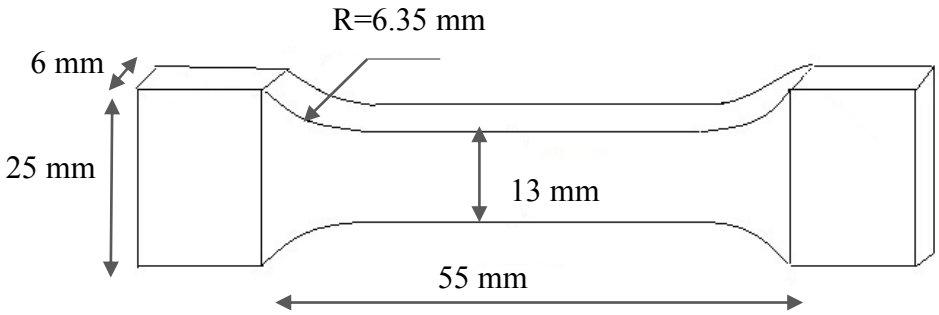

Figure 3.3: Schematic of tension sample.

3.3 Designing Sample Grips

As polymer gel employed was highly compliant, direct gripping using standard Instron grips for performing tension tests caused the skin to tear. It also led to nicks which

caused premature failure of samples in the grips. An alternative solution was developed to resolve this problem. In order to hold the sample in position, polycarbonate end tabs were glued to the dog-bone specimen ends. Different end tab configurations with various glues (super glue, gorilla glue, Loctite 3092, Loctite 401, Loctite 454, Loctite 406 and Loctite 380) and different end tab shapes shown in Fig. 3.4 (top) were tested. After many trials with different configurations and glues, a particular configuration shown in Fig. 3.4 (bottom), with Loctite 401 glue served the purpose. Here, the end tabs were made of polycarbonate and glued (red lines) to the sample ends.

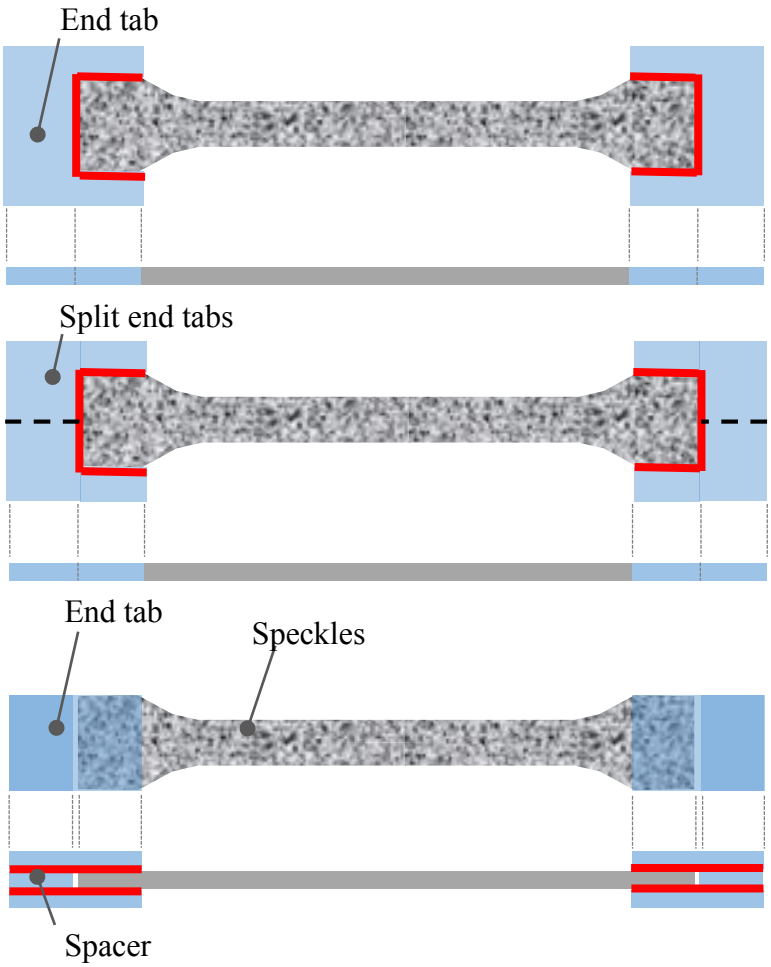

Figure 3.4: Unsuccessful (top, middle) and successful design configurations of tensile dog-bone specimens with polycarbonate end-tabs and spacers (bottom).

Spacers used between the end tabs were also made of polycarbonate and had the same thickness as that of the sample preventing squeezing of the sample (thickness wise compression) in end tab regions. The entire combination was gripped in the loading machine *only in the location of spacers*.

3.4 Speckles

3.4.1 Speckle Pattern

The implementation of 2D DIC requires a speckle pattern applied to the surface of the test specimen. It typically consists of random black and white patterns. Unlike general DIC techniques used for studying conventional materials where alternative black and white spray paint is used to accomplish this, additional care was needed for gel samples. Accordingly, a low viscosity FW Acrylic Artists' ink was used to create speckles on gel samples. The acrylic ink was preferred to standard spray paint approach in order to prevent reinforcement and hence the mechanical response of the gel. Further, disjointed speckles were deposited to further mitigate this problem. As the gel sample had good transparency, only the black ink was sufficient to create random speckles on the sample.

As shown in Fig. 3.6, the speckle pattern should be random such that the light intensity distribution (gray scale) of each sub-image is unique from its neighbor. The number of pixels in a sub-image is defined by the user. In this figure sub-image size is 15 x 15 pixels (red box) with a step size of 13 pixels in both the horizontal and vertical directions (blue box). As each sub-image displaces, the amount of deformation is measured

relative to the reference image. Based on the relative movement of the speckle pattern between images, quantities such as displacement and strain are evaluated.

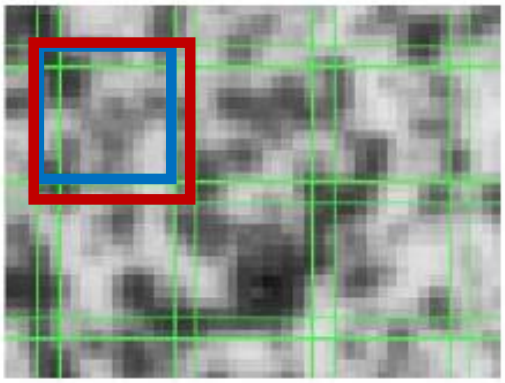

Figure 3.5: Sub-images with overlap viewed over speckle pattern (Reproduced from [26])

3.4.2 Size of Speckles

The choice of speckle size for a particular test depends on various factors such as spatial resolution of the images (pixel count and pixel count/unit length), area of interest and deformation magnitude. Speckle pattern is randomly distributed over the entire image area. The smallest speckle size should be atleast the size of 4 pixels. However, speckle size should not be very large because there is a trade-off in terms of minimum measurable displacement. Both the speckle sizes chosen in this work were selected by taking these factors into account. The area containing speckles was used for analysis using ARAMIS software. As shown in Fig. 3.6, the area outside the speckles i.e., the shaded region

corresponding to the gripping region that contains no data points for analysis were excluded.

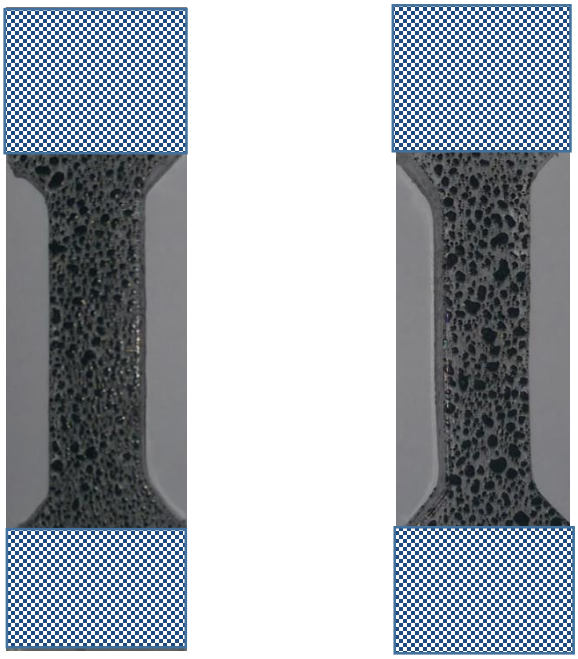

Figure 3.6: Fine (left), coarse (right) speckle patterns on a dog-bone tensile test samples used.

Tension tests were performed using an Instron 4465 machine fitted with 50 N load-cell at a crosshead speed of 2 mm/sec on both the samples types shown in Fig. 3.6 and images were recorded at 4 frames/sec using a Point Grey camera with 2048 x 2048 pixel resolution. As the maximum longitudinal strains were estimated to be around 200%, the sub-image size of 105 x 35 pixels (105 pixels in horizontal direction and 35 pixels in vertical direction) with a sub-image step of 20 pixels in the *x*- and *y*-directions was chosen for both the experiments so that all the sub-images in the region of interest were correlated over the entire deformation history. After performing 2D image correlation using

ARAMIS, axial and transverse strains were obtained from a point in the center of the sample within the gage length free from edge effects. The load data obtained from the testing machine and initial cross-sectional area of the sample were used to evaluate the engineering axial stress. From Fig. 3.7, it can be seen that good repeatability exists in the engineering axial stress-axial strain response with the two speckle sizes (fine and coarse) used. In each of these plots, the last data point corresponds to specimen failure in the gage section.

Due to a relatively large deformation at failure (around 200% strain) the coarser speckles were selected for subsequent experiments such that the speckles could be correlated until the last deformed stage of the sample.

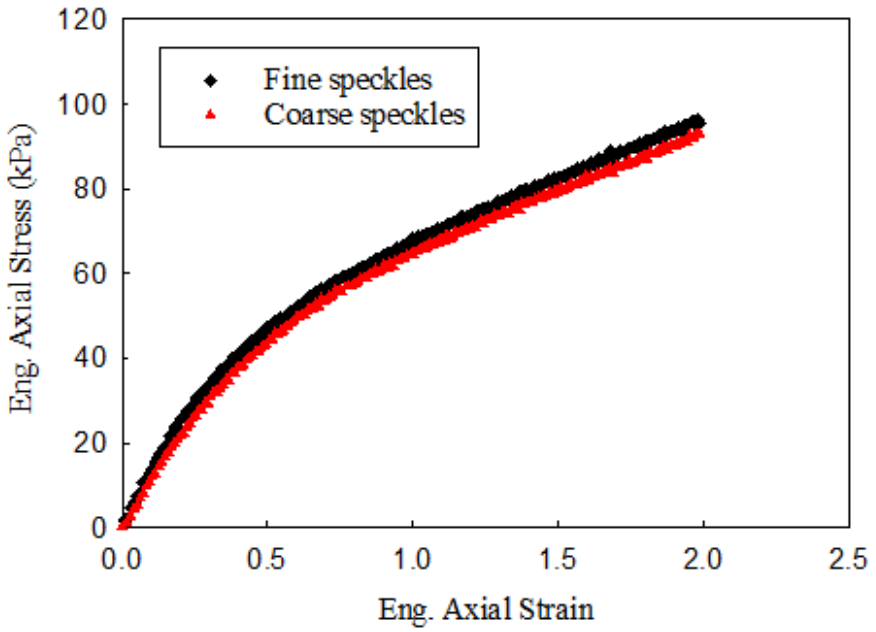

Figure 3.7: Engineering axial stress – axial strain response from tension tests at 2 mm/sec crosshead speed for fine and coarse speckles.

3.4.3 Consistency of Speckle Pattern

In DIC, consistency of speckle pattern is important for obtaining full-field results. If some regions in the area of interest have relatively large/small speckles or higher/lower density of speckles (Fig. 3.8), the speckle pattern is said to be inconsistent. It is also

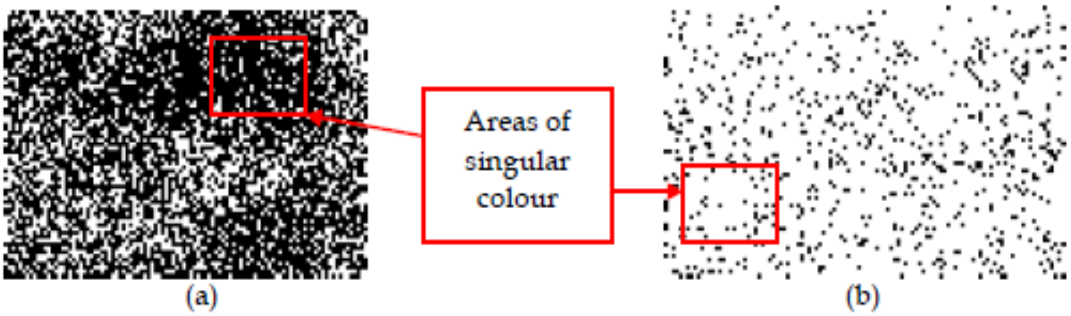

Figure 3.8: Examples of poor speckle pattern consistency (a) too much black, (b) too much white (Reproduced from [27])

important for the speckle pattern to be random such that no two sub-images are identical and all the required sub-images are correlated. In both the situations, there is a risk of information loss as these regions may not get correlated during analysis.

Figure 3.8(a) shows a speckle pattern with too many speckles resulting in large dark areas. On the other hand, Fig. 3.8(b) shows a speckle pattern with too few dark speckles producing large white areas. Hence, consistency of speckle pattern is important to ensure that all regions are correlated and there is no loss of information.

3.4.4 Speckle Application Technique

For DIC, it is also vital to apply the speckles randomly to the test surface besides size and uniformity. To determine the most appropriate speckle pattern application

technique for performing tension tests on the gel, a variety of methods such as (a) random pattern printed with black ink on a white paper and transfer onto the gel sample, (b) manually create dots directly on the sample with a marker, (c) air brush speckles with a compressor operating at different pressures, (d) plucking the bristles of a tooth brush dipped in ink, were tried. The easiest and the best way to achieve this was found to be method (d). A clean brush was partly dipped in ink so that an optimum amount of ink was imbibed into the gaps between the bristles. Then the brush was brought near the sample surface and the bristles were slowly plucked by a finger so as to spray ink on to the sample surface. After some trials, the amount of ink, the distance between the sample and brush were understood and varied to achieve different speckle sizes.

3.5 Effect of Sub-image Size

The number of pixels chosen for each sub-image determines the sub-image size. Smaller sub-images correspond to higher data resolution as each one corresponds to a data point in the field during analysis. However if the sub-image size is smaller than the ideal, the sub-image will be not be recognized during correlation and measurement accuracy will be compromised. Typically, the minimum sub-image size selected is such that all the sub-images in the image are capable of providing deformation and strain information during correlation. Larger sub-image size produces higher averaging effect when compared to

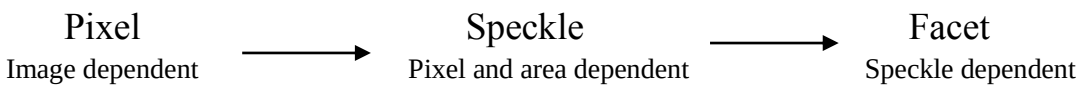

Figure 3.9: Relation between pixel, speckle and sub-image (Reproduced from [27])

smaller sub-image size. The size of the speckle pattern applied which is dependent on image resolution is also important as it dictates the minimum sub-image size that can be used.

When images with large deformations (up to 200 % strain in the axial direction) are to be correlated, there is a criteria based on which sub-image size is to be selected. In this case, the final length of the sample in the axial (maximum strain) direction is three times the initial length. Therefore, in order to achieve correlation until failure, the sub-image chosen should be rectangular such that the ratio of pixels in *x*- and *y*-directions is approximately 3:1. By doing so, the sub-images initially rectangular, deform into a square, at the last stage of deformation. This plays a crucial role in achieving satisfactory correlation of speckles.

When deformations are large, the image analysis software may not correlate throughout the load cycle (or load history) by just taking the first undeformed image as the reference image for all stages of deformed images. To circumvent this problem, each image can be set as the reference image for the next. This approach was adopted in this work when needed. This was done as follows: 1. Import all images into ARAMIS, 2. Select all stages (images) except the first (i.e., stage 0), 3. Right-click and set as reference. Despite this, note that the values such as displacements and strains reported by the image analysis software as output are with respect to the reference (no-load) image and not with respect to the previous image.

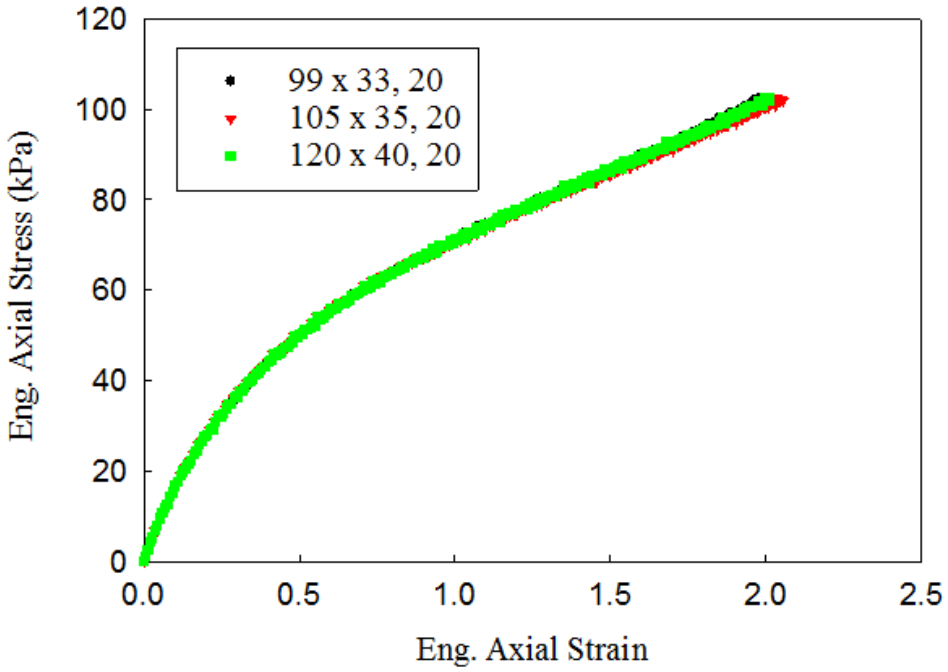

Figure 3.10: Engineering axial stress–axial strain response from tension tests at 2 mm/sec for three different 3:1 sub-image sizes.

By taking these factors into account, three different facet sizes were selected and speckle correlation was performed. The engineering axial stress vs axial strain response for 2 mm/sec crosshead speed is compared in Fig. 3.10. A good agreement is observed between different sub-image sizes and hence any of these facet sizes should be sufficient to extract the result.

3.6 Effect of Sub-image Overlap

Another factor available to the user is the number of overlapping pixels during image correlation. Some overlap is always desirable because more data points from the

same image can be generated for improving measurement accuracy. However, more than 50% overlap is generally undesirable.

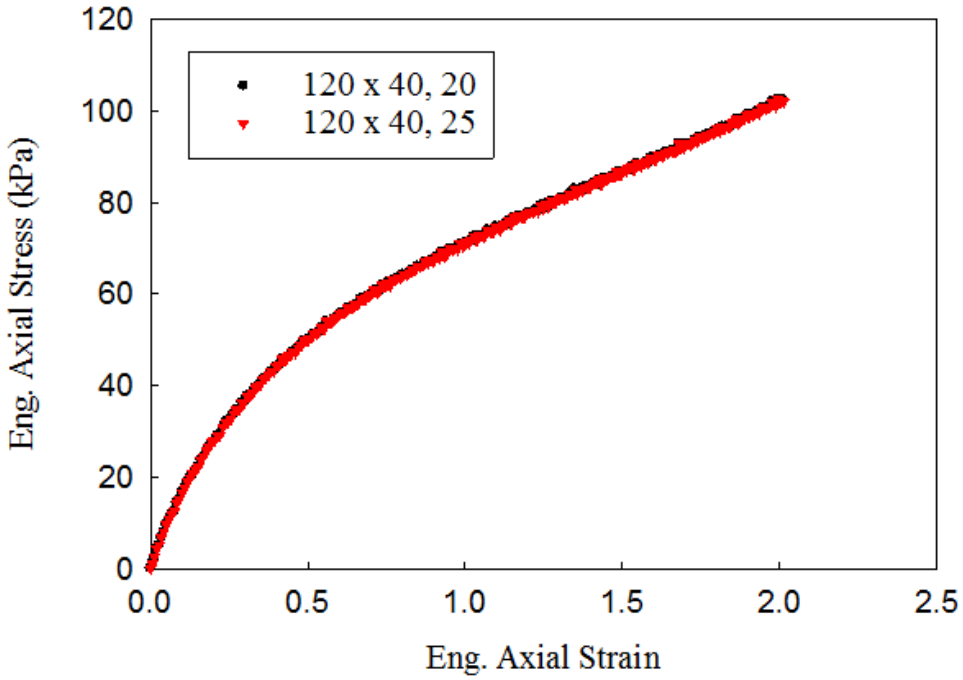

Figure 3.11: Engineering axial stress–axial strain response from tension tests at 2 mm/sec for two different overlaps but identical sub-images.

Figure 3.11 shows engineering axial stress vs axial strain response obtained using two different sub-image steps or pixel overlaps. Evidently, there is a good agreement between all of them suggesting the choice of any of these overlaps is reasonable to achieve convergence of the result.

3.7 Effect of Crosshead Speed

Figure 3.12(a) and 3.12(b) show the effect of crosshead speed on the engineering and true stress-strain responses, respectively. We can observe that with an increase in the crosshead speed or the strain rate, the gel material stiffens and ultimate stress increases. It is important to note that failure strain also increases with an increase in crosshead speed. This is an interesting and rather peculiar behavior of this polymer gel unlike other conventional engineering materials which typically show a reduction in failure strain with an increase in the ultimate stress and strain rate. Interestingly, a similar response has been reported by Moy et al. [6] who have studied a different hydrogels (20% by mass 250 bloom type-A ordinance gelatin with 40˚C ultra-pure filtered water).

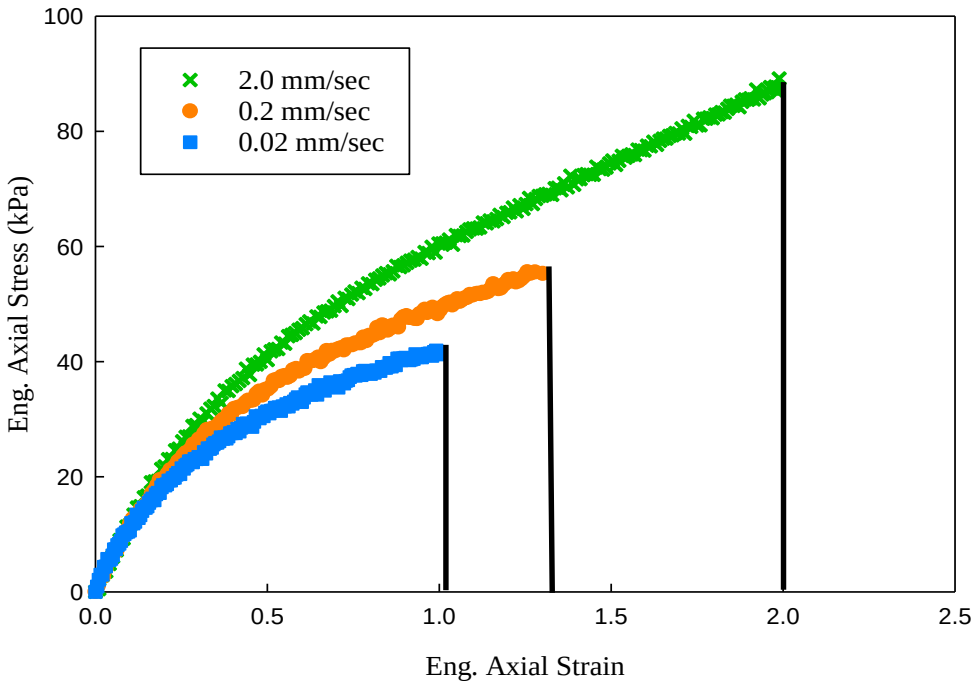

Figure 3.12(a): Engineering stress-strain response of the polymer gel at three different crosshead speeds.

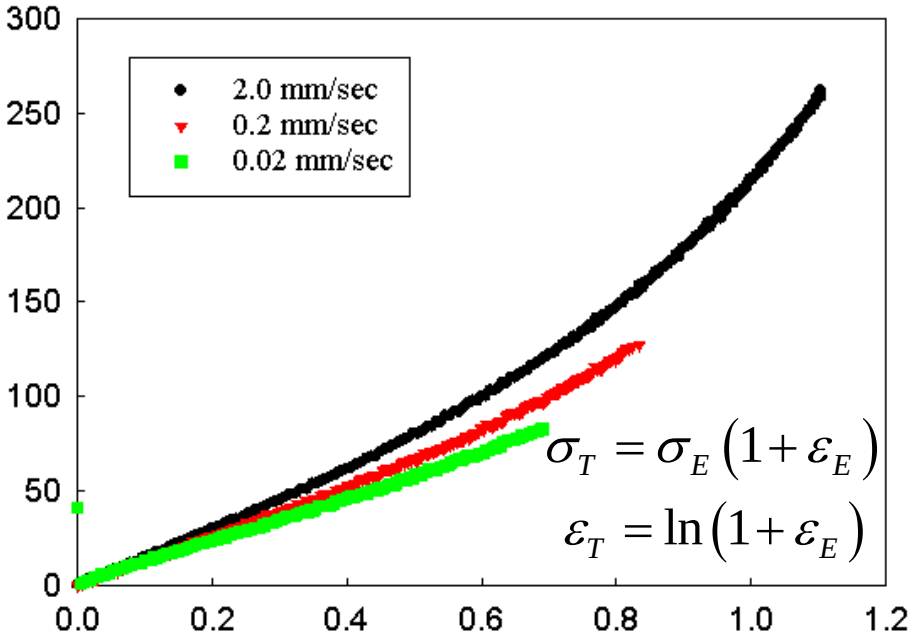

Figure 3.12(b): True stress-strain response of the polymer gel at three different crosshead speeds.

3.8 Experimental Repeatability

The repeatability of experiments was investigated by performing tension tests on multiple dog-bone samples. Experiments were performed with the setup shown earlier. The speckle images were recorded at 10 frames/sec and at a crosshead speed of 2 mm/sec. The sub-image size selected was 150 x 50 pixels and sub-image step was 30 pixels (scale factor = 0.045 mm/pixel) so that all the images were correlated in all the experiments until failure occurred. As noted earlier, the engineering axial stress was calculated from the load-cell data and the nominal sample dimensions whereas engineering axial strains were measured

from DIC. These responses are plotted in Fig. 3.13. It can be observed that there is a good agreement between the tests suggesting a high degree of experimental repeatability.

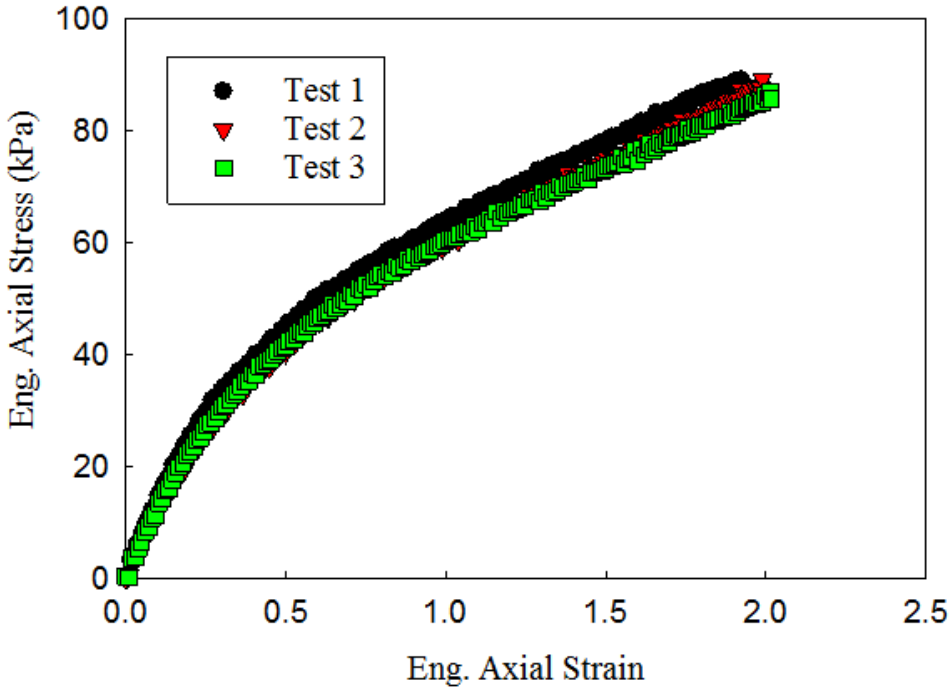

Figure 3.13: Engineering stress-strain responses to check repeatability of tension tests.

3.9 Comparison of Crosshead Strain with DIC

The gel material being highly compliant, many optical and gripping strategies had to be employed during experimentation. Hence, an independent evaluation of strains was carried out to increase the confidence level in measured axial strains before utilizing transverse strains for Poisson's ratio evaluation. A comparison of measured strains from the crosshead displacement and DIC were made for tension tests on dog-bone samples. The experiment was performed with the setup discussed earlier. Images were recorded at 10 frames/sec and a crosshead speed of 2 mm/sec. The sub-image size used during DIC

analysis was 150 x 50 pixels, and sub-image step size was 30 pixels. The engineering axial stress was calculated from the load data and sample dimensions. The crosshead axial strain was measured from (a) the crosshead displacement records and the initial gage length of the sample, and (b) DIC strain after correlating speckle images with the reference image. These responses are plotted in Fig. 3.14. It can be observed that there is quite a good agreement between the two responses which implies that there is no slipping of the sample within the grips or in the end tab regions. Hence strains measured from DIC are reliable and can be used to extract transverse strains as well.

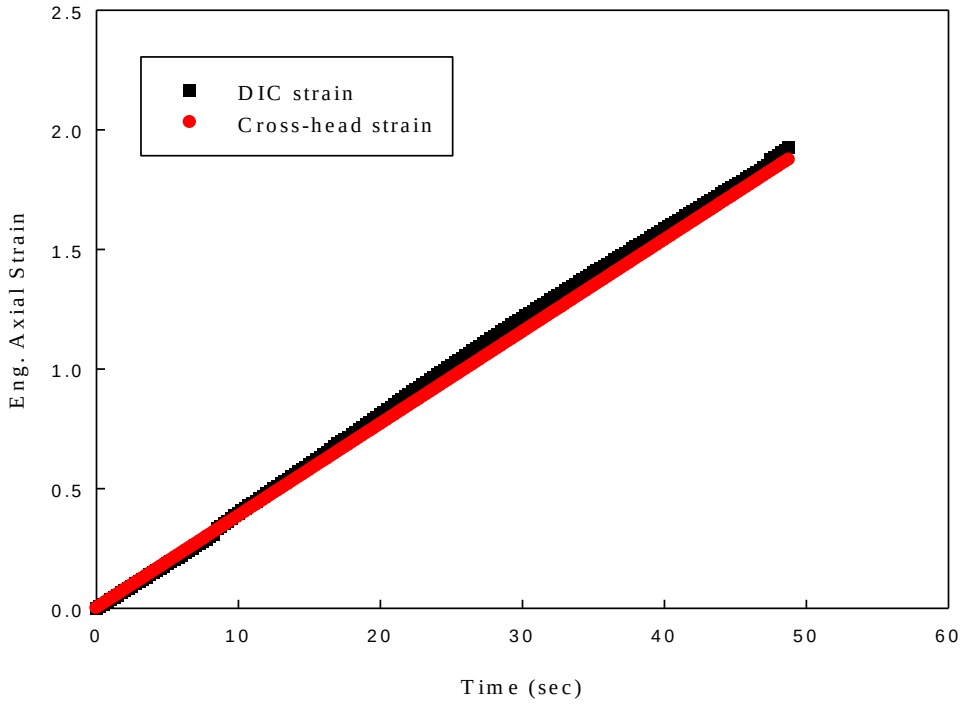

Figure 3.14: Comparison of strains obtained from crosshead displacement and Digital Image Correlation (DIC).

3.10 Tensile Elastic Modulus

From the engineering stress-strain responses, it can be seen that the polymer gel exhibits a nonlinear behavior. It is also known from the manufacturer that the material is

isotropic. As the gel material is incompressible (say, like rubber), its Poisson's ratio is close to 0.5. Based on these, concepts of hyperelasticity were used to determine the elastic modulus of the gel. Generally stress-strain relations for a hyperelastic material are developed from strain energy density functions. Three commonly used hyperelastic models were considered for evaluating gel elastic properties and model the overall stress-strain response. General hyperelastic stress-strain relation for isotropic material [28, 29, 30] is of the form,

$$[\sigma] = \frac{1}{J}[F]\left[\frac{\partial W}{\partial \varepsilon}\right][F]^T \tag{3.1}$$

where J is the Jacobian, $\left(J = \det[F]\right)$, σ, ε, W and F are Cauchy's engineering stress, engineering strain, strain energy density function and deformation gradient tensor, respectively.

For an incompressible material with nonlinear elastic and large deformations, stress-strain relation can be deduced to the form,

$$[\sigma] = -p^*[I] + 2\frac{\partial W}{\partial I_1^B}[B] - 2\frac{\partial W}{\partial I_2^B}[B]^{-1} \tag{3.2}$$

where p^* is a function of load, B, I_1^B and I_2^B are Finger deformation tensor, first and second invariants of Finger deformation tensor, respectively.

If the strain energy density function is known, the above expression can be simplified further to obtain stress-strain relations for an uniaxial tension test. Strain energy density functions from three different models namely Neo-Hookean, Mooney-Rivlin and Yeoh models are as given below [31-34]:

Neo-Hookean model: $$W = c_{10}\left(I_1^B - 3\right) \tag{3.3}$$

Mooney-Rivlin model: $$W = c_{10}\left(I_1^B - 3\right) + c_{01}\left(I_2^B - 3\right) \tag{3.4}$$

Yeoh model: $$W = c_1\left(I_1^B - 3\right) + c_2\left(I_1^B - 3\right)^2 + c_3\left(I_1^B - 3\right)^3 \tag{3.5}$$

When p^*, B, I_1^B , I_2^B and partially differentiated quantities of strain energy density function W are known, the expressions for engineering stress-engineering strain can be obtained [35] as shown below:

Neo-Hookean model: $$\sigma = 2((1+\varepsilon)^2 - \frac{1}{(1+\varepsilon)})(c_{10}) \tag{3.6}$$

Mooney-Rivlin model: $$\sigma = 2((1+\varepsilon)^2 - \frac{1}{(1+\varepsilon)})(c_{10} + \frac{c_{01}}{(1+\varepsilon)}) \tag{3.7}$$

Yeoh model $$\sigma = 2((1+\varepsilon)^2 - \frac{1}{(1+\varepsilon)})(c_1 + 2c_2((1+\varepsilon)^2 + \frac{2}{(1+\varepsilon)} - 3) + 3c_3((1+\varepsilon)^2 + \frac{2}{(1+\varepsilon)} - 3)^2) \quad (3.8)$$

In the above three equations, σ and ε are known stress and strain quantities from tension tests and $C_{10}, C_{01}, C_1, C_2, C_3$ are the unknown constants to be determined to evaluate the elastic modulus of the material. They are extracted using linear least-squares analysis of the data (in MATLAB). Based on the resulting R-square value, the goodness of fit was determined to select the model for this research. Out of the three models, Mooney-Rivlin was the one which had the best value for goodness of fit. Further, Mooney-Rivlin is the most commonly used model in the literature [36-38] for investigating the mechanical behavior of biological tissues. Since a polymer gel was employed here to potentially simulate tissue behavior, this model selection is justifiable. The goodness of fit information for stress-strain responses shown in Fig. 3.12 are presented in Table 3.1.

Cross-head speed (mm/sec)	Goodness of fit (R–square)		
	Neo-Hookean model	Mooney-Rivlin model	Yeoh model
2	0.5317	0.9954	0.9759
0.2	0.6025	0.9962	0.9852
0.02	0.6650	0.9957	0.9888

Table 3.1: Goodness of fit for different hyperelastic models.

In the limit $\varepsilon \to 0,$ the derivative of the stress variation with respect to the strain will yield the elastic modulus, $E\left(=\frac{d\sigma}{d\varepsilon}\right)$. Thus, the elastic modulus can be obtained from the unknown constants for each model as,

Neo-Hookean model: $$E = 6c_{10} \tag{3.9}$$

Mooney-Rivlin model: $$E = 6(c_{10} + c_{01}) \tag{3.10}$$

Yeoh model: $$E = 6c_1 \tag{3.11}$$

Crosshead Speed (mm/sec)	Elastic Modulus *E* (kPa)	Strain Rate $\dot{\varepsilon}$ (/sec)
2	125.42 ± 5.48	0.04
0.2	118.39 ± 3.63	0.004
0.02	111.37 ± 4.17	0.0004

Table 3.2: Elastic modulus dependence on crosshead speed.

The resulting elastic moduli (E) are listed in Table 3.2. The values suggest a modest (~25 kPa) increase of E with strain rate change of two orders of magnitude. The elastic moduli of polymer gel are comparable to that of biological tissues.[12]

[1] Faury, G. "Function–structure relationship of elastic arteries in evolution: from microfibrils to elastin and elastic fibres." Pathologie Biologie 49.4 (2001): 310-325.
[2] Nakano, K., et al. "Myocardial stiffness derived from end-systolic wall stress and logarithm of reciprocal of wall thickness. Contractility index independent of ventricular size." Circulation 82.4 (1990): 1352-1361.

3.11 Initial Poisson's Ratio

From the tension tests described earlier, axial strains and transverse strains were obtained from DIC from each image. Engineering axial strain and transverse strain responses are plotted for different crosshead speeds in Fig. 3.15.

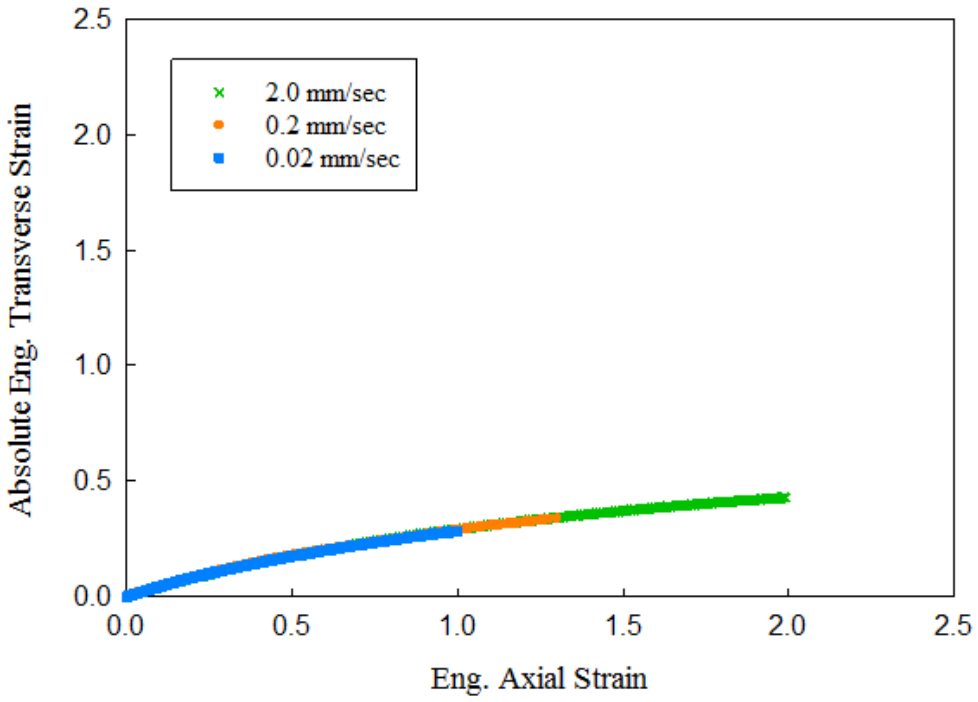

Figure 3.15: Engineering transverse strain vs axial strain response at different cross-head speeds.

The initial linear region was used in each of the above plots to obtain the Poisson's ratio of the gel by performing a linear regression analysis. That is, the response was fitted to a straight line and the slope of the line indicates the Poisson's ratio of the polymer gel.

Thus obtained value of Poisson's ratio are shown in Table 3.3. As expected, the values are close to 0.5, suggesting the gel response nearly incompressible.

Crosshead Speed (mm/sec)	Poisson's Ratio υ	Strain Rate $\dot{\varepsilon}$ (/sec)
2	0.46 ± 0.009	0.04
0.2	0.48 ± 0.009	0.004
0.02	0.46 ± 0.013	0.0004

Table 3.3: Poisson's ratio values at different crosshead speeds.

3.12 Ultimate Stress and Failure Strain

From the tension tests, ultimate stresses and failure strains were recorded for different experiments and are shown in Table 3.4. It is observed that both the values increased with an increase in the crosshead speed. Increase in the ultimate stress is to be expected, but the increase in failure strain is an interesting behavior of the polymer gel. Nearly a 100% increase in the failure strain at 2 mm/sec relative to the 0.02 mm/sec is evident.

Crosshead Speed (mm/sec)	Ultimate Stress (kPa)	Failure Strain
2	87.16 ± 1.33	1.97 ± 0.04
0.2	54.48 ± 0.83	1.25 ± 0.08
0.02	42.69 ± 2.29	0.99 ± 0.01

Table 3.4: Ultimate stress and failure strains at different crosshead speeds.

Chapter 4. Shear Response

This chapter deals with shear tests conducted on the polymer gel to determine its shear modulus. First, the experimental setup is discussed and details regarding sample preparation and gripping method are provided. Later, the effect of strain rate on shear modulus is quantified. Finally, these experimental values of shear moduli are compared with those using the elastic moduli and Poisson's ratios from tension tests.

4.1 Sample Preparation

Figure 4.1: Photograph of hot wire cutter used to cut polymer gel samples.

Void-free rectangular gel sheets of required thickness were prepared first as discussed in the previous chapter. A hotwire cutter (Thermocut – Proxxon, see Fig.4.1) was

employed to cut the gel samples to required dimensions. The specimen dimensions used were 25x12.5x12.5 mm^3. A hotwire with an operating temperature range of 100^oC - 200^oC was selected based on the thickness of the sample.

4.2 Experimental Setup

A photograph of the experimental setup is shown in Fig. 4.2. Rectangular gel samples glued to polycarbonate holders were gripped in an Instron 4465 universal testing machine. The shear tests were performed at three different crosshead speeds of 0.02, 0.2 and 2 mm/sec, same as the ones used for tension tests.

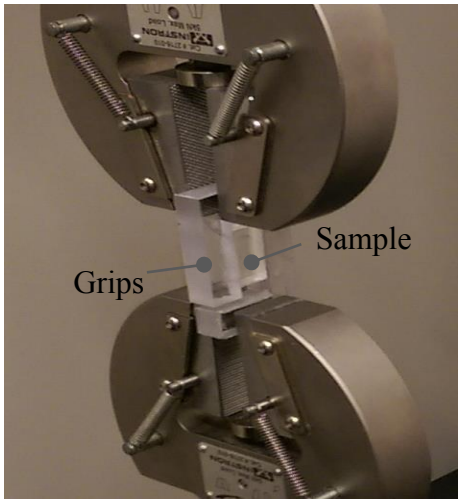

Figure 4.2: Shear test sample gripped using conventional Instron grips.

Holders for the shear specimen were made using polycarbonate sheets, machined to L-shape with dimensions shown in Fig. 4.3. The shape was selected such that the horizontal portion of these holders could be gripped using the standard Instron tension

grips. Holders were designed such that the applied tensile force was transmitted to the sample as a shear force via the glued faces of the gel sample. As in the tension tests, Loctite 401 acrylic adhesive was used to create a good bond between the sample and the polycarbonate holders. The red vertical lines in the figure denote the glued portion of the sample.

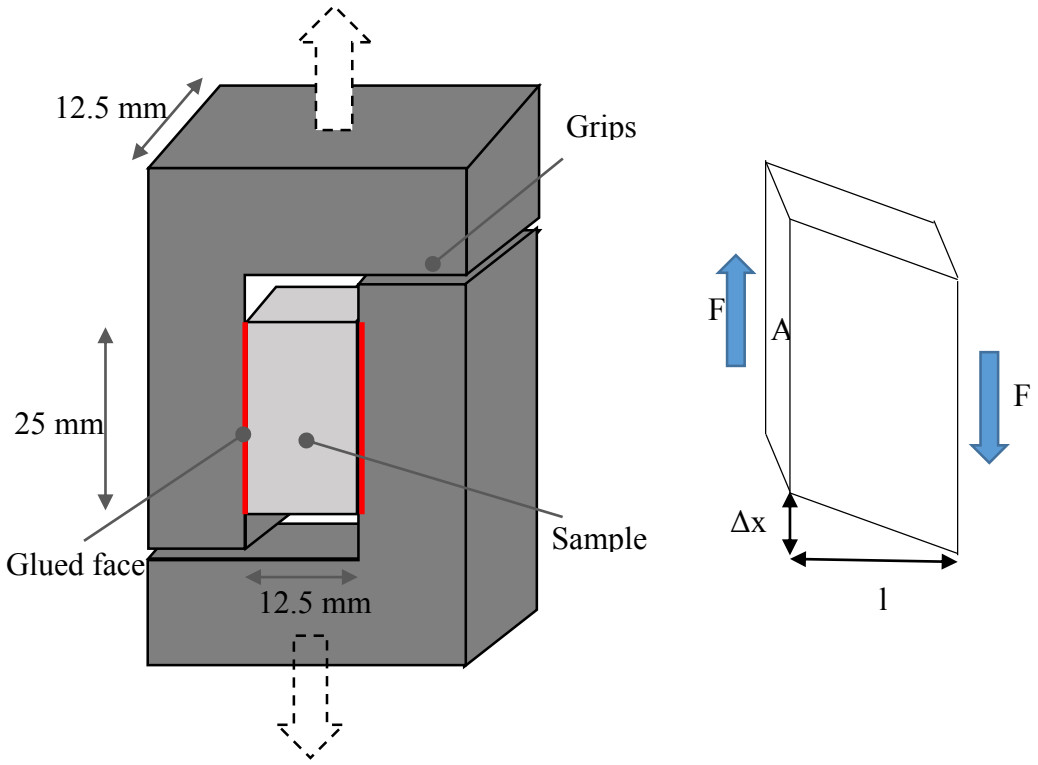

Figure 4.3: Sample holder design (top), shear force acting on the sample (bottom).

As the load increased gradually at different crosshead speeds, the sample underwent shear deformation. It is important to note that all tests were conducted only until the bond (glue) between the holder and the sample failed. *None of the samples actually failed during shear tests.*

4.3 Shear Stress-Shear Strain Response

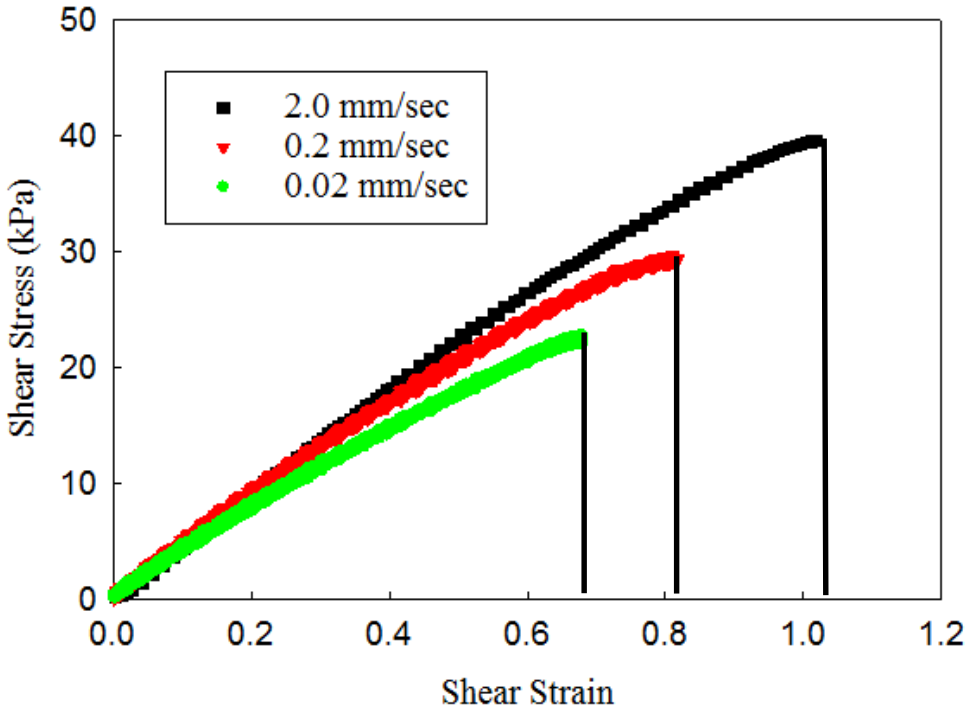

Figure 4.4: Effect of crosshead speed on shear stress-shear strain response of gel. The dotted lines indicate failure of the holder-sample adhesive and not the sample.

Shear tests were performed on an Instron 4465 fitted with 50 N load-cell at three crosshead speeds namely 0.02, 0.2 and 2 mm/sec. The load data obtained from the testing machine and cross-sectional area of the sample on which shear force acted were used to evaluate the shear stress. The dimensions of the sample and the vertical displacement of the crosshead were used to obtain the shear strain. Again, all the tests were conducted until the bond (glue) between the holders and the sample showed debonding, indicated by the dotted lines in the graphs in Fig.4.4.

4.4 Experimental Repeatability

Repeatability of the shear tests was examined. Multiple experiments were performed with the setup discussed previously at a crosshead speed of 2 mm/sec. The shear stress was calculated from the measured load data and the sample dimensions, whereas shear strain was obtained from the crosshead displacement. These responses are plotted in Fig. 4.5. It can be observed that there is a reasonably good repeatability between all three tests.

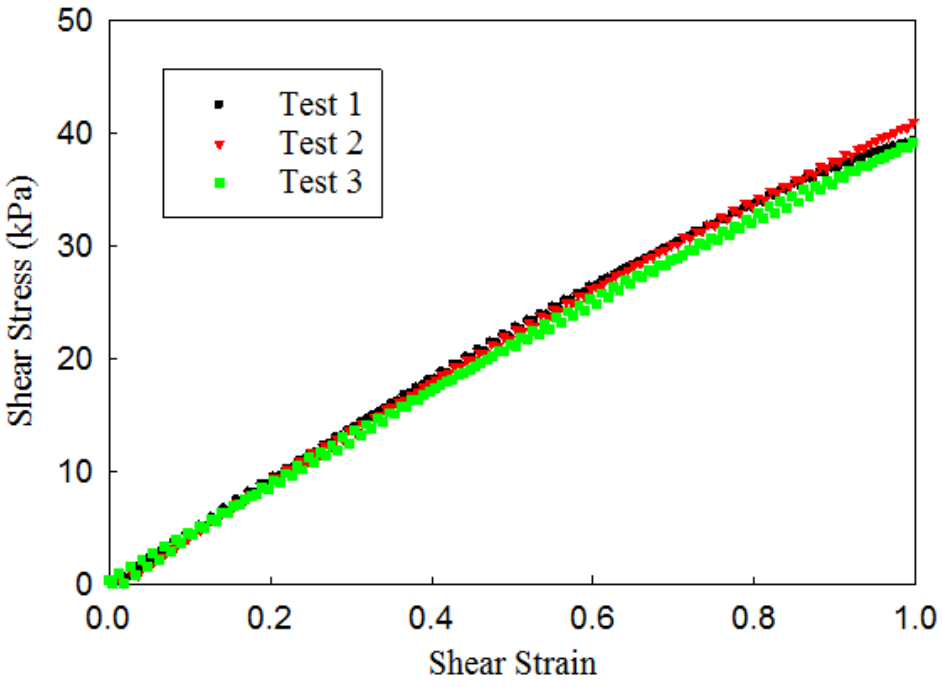

Figure 4.5: Repeatability of shear stress-strain responses.

4.5 Shear Modulus

The gel material being studied is isotropic soft gel, the material is expected to be incompressible (Poisson's ratio close to 0.5). Based on these, concepts of hyperelasticity were used to determine gel shear modulus. Generally shear stress-shear strain relations for a hyperelastic material are developed from strain energy density functions in a way similar to the one discussed in the last chapter for tensile loading.

General stress-strain relation for nonlinear elastic, isotropic material with large deformation from Eqs. (3.1) and (3.2), the expression for shear stress in terms of shear strain can be obtained as,

$$\sigma_{12} = 2\gamma_{12}\left(\frac{\partial W}{\partial I_1^B} + \frac{\partial W}{\partial I_2^B}\right) \tag{4.1}$$

The above expression can be simplified further to the classical shear stress-shear strain relation for a shear test as,

$$\sigma_{12} = G\gamma_{12} \tag{4.2}$$

where the shear modulus,

$$G = 2\left(\frac{\partial W}{\partial I_1^B} + \frac{\partial W}{\partial I_2^B}\right) \tag{4.3}$$

The shear stress was determined using $\sigma_{12} = \frac{F}{A}$ where F is the applied shear force on area A and the shear strain $\gamma_{12} = \frac{\Delta x}{l}$ where Δx is the vertical crosshead displacement determined experimentally and l is width of the sample as shown in Fig. 4.3.

In the above equation, σ_{12} and γ_{12} are measured quantities from tests and G is the unknown quantity to be determined. It can be evaluated directly using least-squares analysis by employing the curve fitting module in MATLAB. The same process was repeated for different crosshead speeds and the respective shear moduli were evaluated for each case. Thus obtained values of *G* are reported in Table 4.1. Also listed in this table are the values obtained from tension tests. The two data sets are in good agreement within acceptable errors confirming the measurements independently.

Crosshead speed (mm/sec)	Shear Modulus *G* (kPa) (Experimental)	Shear Modulus $G = \frac{E}{3}$ (kPa) (from tension tests)
2	41.7 ± 2.1	41.8 ± 1.8
0.2	39.6 ± 1.1	39.5 ± 1.2
0.02	36.7 ± 1.9	37.1 ± 1.4

Table 4.1: Comparison of shear modulus values from shear tests and tension tests at different crosshead speeds.

Chapter 5. Compression Tests

This chapter deals with compression tests performed for evaluating the compressive modulus of the polymer gel. The details regarding sample preparation are provided first and experiments are discussed next. Subsequently, evaluation of compression modulus using hyperelastic material models is described. Lastly, the effect of loading rate on the compression modulus is noted.

5.1 Sample Preparation Details

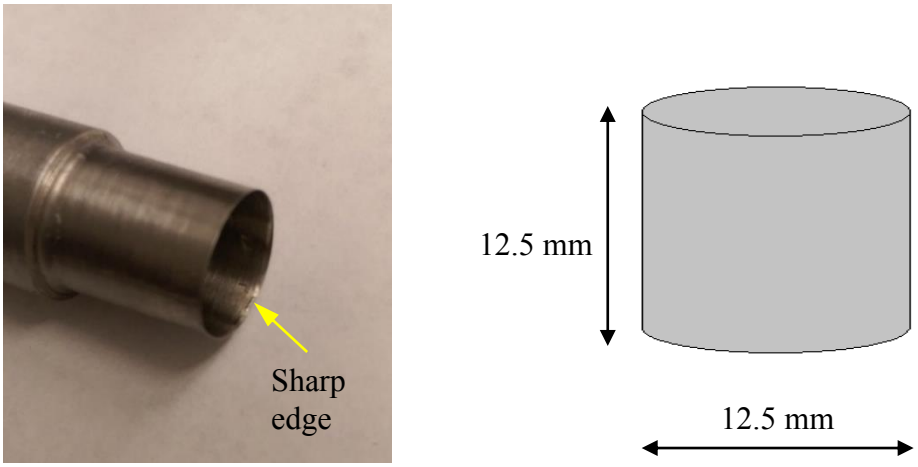

Figure 5.1: Photograph of metal tube with sharpened edge (top), schematic of compression test sample (bottom).

Rectangular gel sheets (12.5 mm thick in this case) devoid of air bubbles and good surface finish were prepared as discussed in Chapter 3. As shown in Fig.5.1, a hollow metal

tube with the required inner diameter (12.5 mm) was machined to make its edge sharp to punch out a cylindrical sample with straight, smooth lateral surface. The punch was first heated to 80^{o}C in an oven and then carefully pressed into the gel sheet laying flat on a polycarbonate substrate. The inner surface of the punch was coated with water which acted as a lubricant between the punch face and gel. As shown in Fig. 5.1, the required cylindrical gel specimens having an aspect ratio of 1 were obtained. Casem et al., have shown that this sample configuration attains equilibrium easily [39].

5.2 Experimental Setup

A photograph of the experimental setup is shown in Fig. 5.2. It consisted of a cylindrical sample compressed between two platens of the testing machine. As in the previous chapters, Instron 4465 universal testing machine was used for performing compression tests at three different crosshead speeds 0.02, 0.2 and 2 mm/sec. The surfaces of the platens were smoothened using 180 grit sand paper and lubricated to minimize friction. This reduced the undesirable barreling effect on the cylindrical sample to achieve a uniaxial state of stress and strain. During tests, the compressive load and crosshead displacement were recorded at regular time intervals (acquisition rate = 4-10 data/sec) using Instron Blue-Hill software for all crosshead speeds.

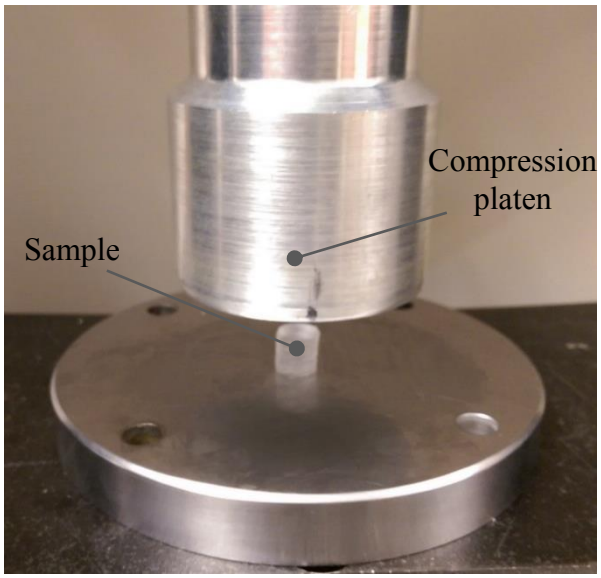

Figure 5.2: Photograph of compression test sample and platens.

5.3 Stress-Strain Response

The tests were performed using an Instron 4465 fitted with a 50 N load cell at three different crosshead speeds namely 0.02, 0.2 and 2 mm/sec. The load data obtained from the load-cell along with the nominal cross-sectional area of the sample were used to evaluate the compressive stress. The original dimensions of the sample and the vertical displacement of the crosshead were used to obtain the compressive strain. Tests were carried out only up to 6 mm of crosshead displacement and not until failure. From Fig. 5.3, we can observe that with an increase in the crosshead speed, material shows a stiffer

response. Casem et al., [39] and Kwon et al. [40] have also observed a similar rate sensitive compressive behavior for gels.

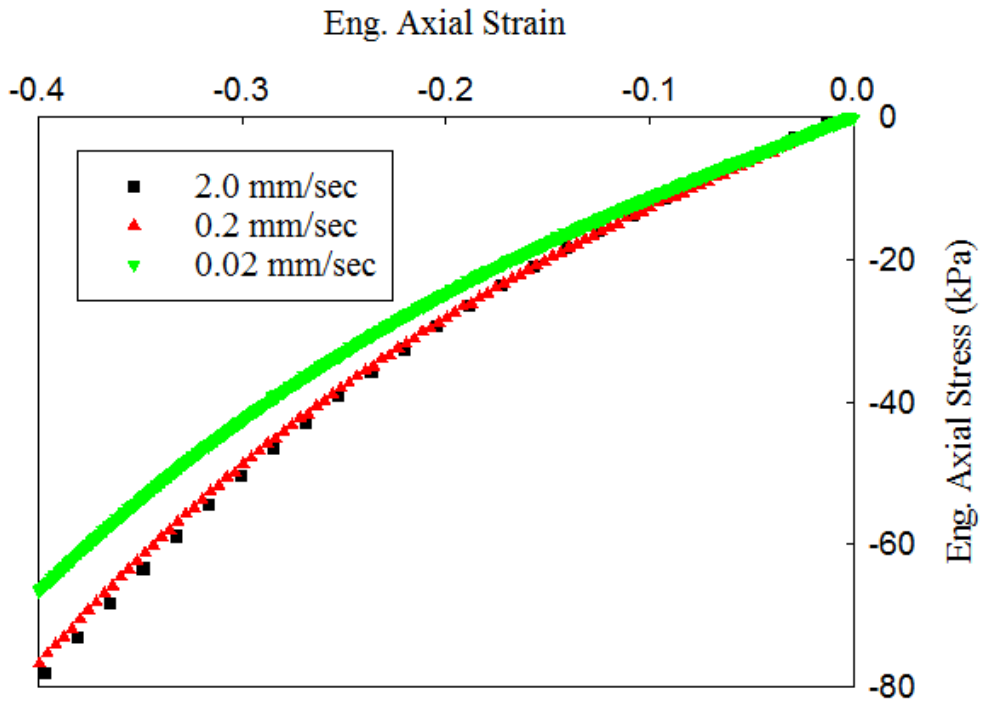

Figure 5.3: Effect of crosshead speed on the compressive stress-strain response of the polymer gel.

5.4 Repeatability

Experiments were repeated for compression tests on cylindrical gel samples to check reproducibility of these tests. The resulting responses are plotted for a crosshead speed of 2 mm/sec in Fig. 5.4. As noted earlier, the tests were stopped at a crosshead displacement of 6 mm (or, a nominal axial strain of 50%). It can be observed that there is a rather good agreement between these tests.

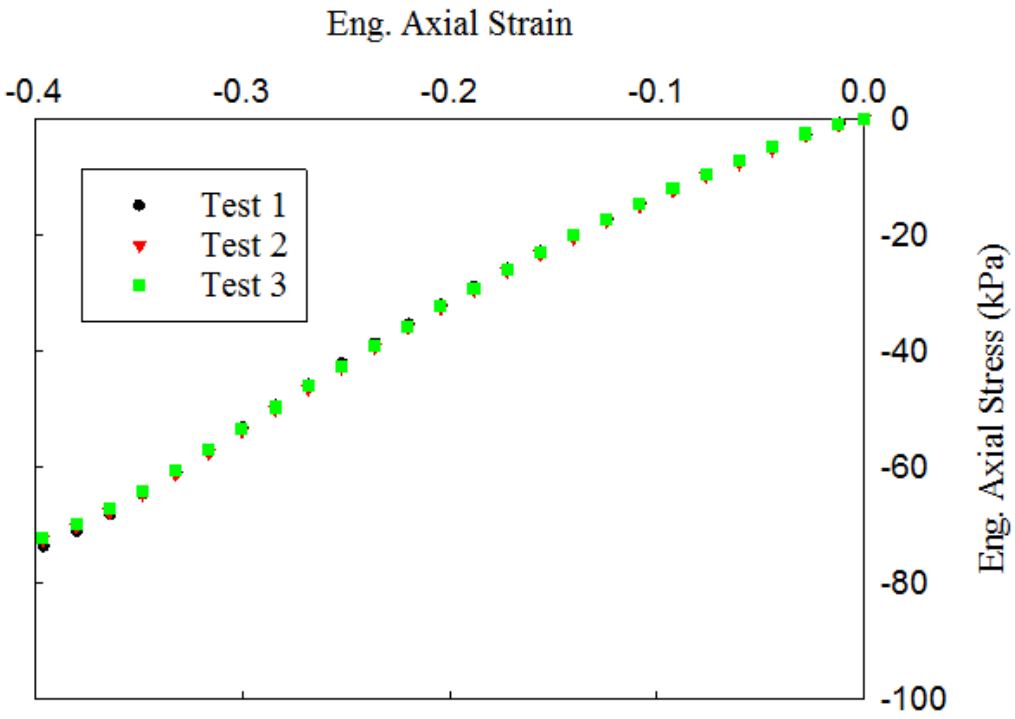

Figure 5.4: Engineering stress-strain responses to check repeatability of compression tests at 2 mm/sec.

5.5 Compression Modulus

As discussed earlier, it is understood that the polymer gel exhibits nonlinear elastic behavior. As its Poisson's ratio is close to 0.5, it is incompressible like rubber. Again, assuming hyperelasticity the compression modulus of polymer gel was determined. If strain energy density function is known, stress-strain relation i.e., Eqn (3.7) for Mooney-Rivlin model can be developed for a hyperelastic material subjected to uniaxial compression experiment similar to the tensile counterpart in Chapter 3. If σ and ε are known quantities from compression tests, then C_{10}, C_{01} are unknown constants which can be determined using least-squares analysis in MATLAB. In the limit $\varepsilon \to 0,$ derivative

of the compressive stress with respect to strain, $\frac{d\sigma}{d\varepsilon} = E$, will yield the compressive modulus (Eqn. (3.10)). Table 5.1 shows good match between compressive and tensile moduli for the polymer gel at different crosshead speeds.

Crosshead Speed (mm/sec)	Compressive Modulus *E* (kPa)	Tensile Modulus *E* (kPa)
2	140.62 ± 4.27	125.42 ± 5.48
0.2	119.23 ± 3.06	118.39 ± 3.63
0.02	103.74 ± 1.08	111.37 ± 4.17

Table 5.1: Compressive modulus dependence on crosshead speed and comparison with the tensile counterparts.

Chapter 6: Opto-Mechanical Characterization

In this chapter, details regarding refractive index measurement are provided first. The working principle of full-field optical method - Digital Gradient Sensing (DGS) - is discussed next. Lastly, specifics about the experiments performed on a disk subjected to diametral compression of the polymer gel samples in conjunction with DGS for determining the elasto-optical constant at various loading rates are presented.

6.1 Refractive Index

Figure 6.1: Abbe refractometer using for evaluating refractive index of polymer gel.

Polymer gel blocks of 10% and 20% composition with good transparency and surface finish were extracted as described earlier and their refractive index (n) was determined using an Abbe refractometer shown in Fig. 6.1.

The gel block whose refractive index is to be determined was placed in between the illuminating and refracting prisms of the refractometer. A lamp (white light) illuminated the sample through the first prism. Light rays undergo refraction that depends on the refractive index of the sample being evaluated. Bright regions are formed where light rays refract into and dark regions correspond to where there is no light. Chromatic aberration knob was used to observe these sharp bright and dark regions. By operating a large dial to position the cross-hairs exactly at the junction of both the regions, the refractive index of the gel blocks was measured. The values are tabulated in Table 6.1.

Gel Type	Refractive Index, *n*
10 %	1.4728 ± 0.0013
20 %	1.4750 ± 0.0008

Table 6.1: Refractive index values for 10 % and 20 % polymer gel blocks.

6.2 Digital Gradient Sensing (DGS) Method

This section deals with the working principle of Digital Gradient Sensing (DGS) method and the experimental setup for measuring the elasto-optical constant for the gel. The significance of the elasto-optical constant is that it accounts for changes in both refractive index and thickness. It allows the optical measurements to be linked with the mechanical fields.

6.2.1 Experimental Setup

The schematic of the experimental setup for DGS method is shown in Fig. 6.2. It consists of a digital camera, a planar transparent test object and a uniformly illuminated speckle target plate. The target is coated with fine mists of black and white paint. The transparent specimen is placed at a distance of Δ from the target. A digital camera is placed behind the specimen at a distance of L (>> Δ) and focused on the target plane through the specimen in the region of interest.

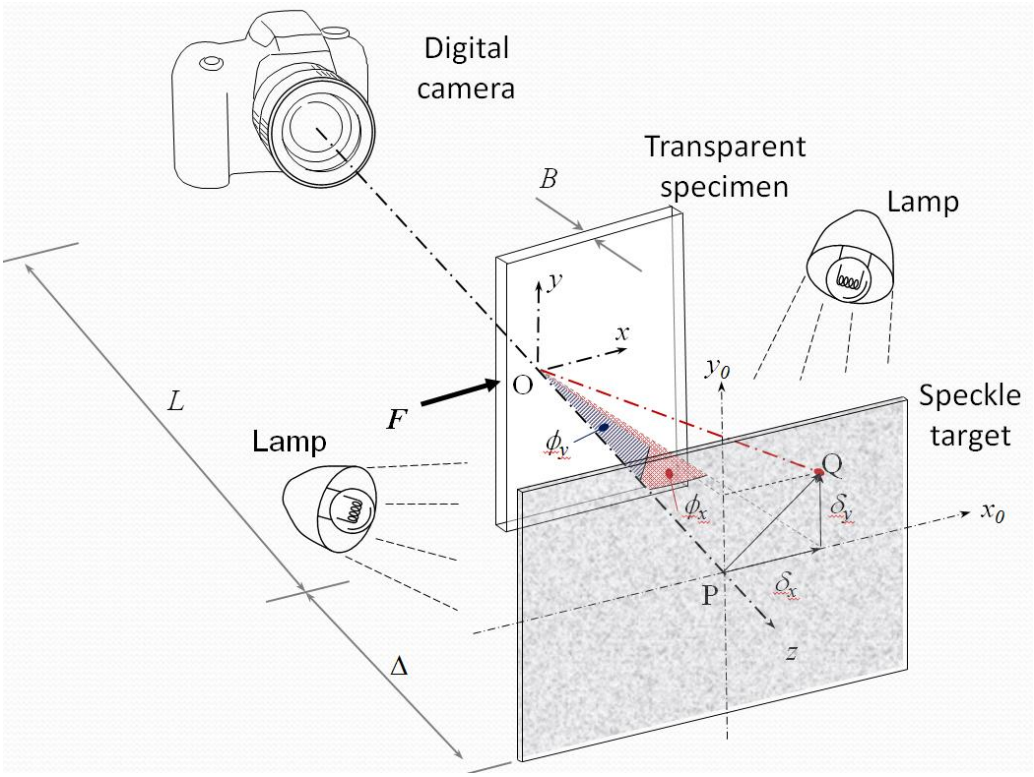

Figure 6.2: Schematic of experimental setup for Digital Gradient Sensing (DGS) method.

6.2.2 Working Principle

During the experiment, speckles on the target plate are photographed normally through the transparent gel specimen of thickness *B* and refractive index *n*. A generic point P on the target plane, corresponding to a point O on the specimen plane is recorded by the camera in the undeformed state of the sample. When the specimen is subjected to force *F*, as shown in Fig. 6.2, refractive index and thickness change throughout the field. Point P on the optical axis observed through the specimen is displaced to a neighboring point Q on the target plane by δ_x and δ_y in the *x*- and *y*-directions, respectively. The quantities δ_x and δ_y are determined by correlating deformed image with respect to the undeformed image using Digital Image Correlation (DIC) technique. If the separation distance Δ between the mid-plane of the specimen and the target is also known, the angular deflections ϕ_x and ϕ_y in the *x*-*z* and *y*-*z* planes can be determined. The optical path change is obtained in terms of normal strain, ε_{zz}, and change in the refractive index, δn, as [41],

$$\delta S(x,y) = 2B(n-1)\int_0^{1/2} \varepsilon_{zz}\; d\left(z/B\right) + 2B\int_0^{1/2} \delta n\; d\left(z/B\right) \tag{6.1}$$

The refractive index change is given by the Maxwell relation (Eq. (6.2)),

$$\delta n(x,y) \approx D_1(\sigma_{xx} + \sigma_{yy} + \sigma_{zz}) \tag{6.2}$$

where D_1 is the stress-optic constant, σ_{xx}, σ_{yy} and σ_{zz} are the normal stresses in the *x*-, *y*- and *z*- directions, respectively.

Using the generalized Hooke's law for an isotropic, linear elastic solid, the normal strain component ε_{zz} is

$$\varepsilon_{zz} = \frac{1}{E}\left[\sigma_{zz} - \upsilon(\sigma_{xx} + \sigma_{yy})\right] \tag{6.3}$$

where *E* is the elastic modulus and υ is the Poisson's ratio of the gel. Now, using Eqs. (6.2), (6.3), Eq. (6.1) can be simplified under plane stress conditions to obtain the expression for optical path change as [41],

$$\delta S(x, y) \approx C_\sigma B(\sigma_{xx} + \sigma_{yy}) \tag{6.4}$$

where C_σ is the elasto-optical constant defined as

$$C_\sigma = D_1 - \frac{\upsilon}{E}(n-1) \tag{6.5}$$

where D_1 is the stress-optical constant, υ is the Poisson's ratio, *E* is the elastic modulus and *n* is refractive index.

After performing a geometrical analysis [41], relationship for the angular deflections ϕ_x and ϕ_y in the *x*-*z* and *y*-*z* planes in terms of the elasto-optical constant and two orthogonal in-plane stress gradients (Eq. (6.6) and Eq. (6.7)) [41] can be obtained as,

$$\phi_x \approx \frac{\delta_x}{\Delta} = C_\sigma B \frac{\partial(\sigma_{xx} + \sigma_{yy})}{\partial x} \tag{6.6}$$

$$\phi_y \approx \frac{\delta_y}{\Delta} = C_\sigma B \frac{\partial(\sigma_{xx} + \sigma_{yy})}{\partial y} \tag{6.7}$$

6.3 Disk under Diametral Compression

Disk under diametral compression is one of the standard geometries used in photoelasticity to measure stress-optic constant of birefringent materials [42]. Since the stress fields are readily available for this geometry, it is possible to compare the experimental results with analytical solutions. Further, this geometry is also used to determine failure properties of materials by some investigators. For example, the tensile strength of brittle materials has been evaluated using this geometry in Refs. [43-44]. Shetty et al. and S. Dong et al. have studied the fracture behavior using disks subjected to diametral compression [45-46].

The details on Digital Gradient Sensing (DGS) experiments performed on a disk subjected to diametral compression of gel samples are as follows: It includes particulars about sample preparation, experimental setup, optical measurements and comparison with analytical expressions are included. As noted earlier, using DGS two orthogonal in-plane stress gradients due to imposed loads were measured as angular deflections of light rays.

The measurements were used to extract the elasto-optical constant for the polymer gel to facilitate optical investigation of stress concentration problems and, subsequently examine the feasibility of the gel as a tissue surrogate to optically study the mechanics of needle insertion/retraction.

6.3.1 Sample Preparation

Rectangular gel sheets (12.5 mm thick) devoid of air bubbles, good transparency and surface finish were prepared as discussed previously. Both the polycarbonate mold faces were detached on either side of the sample and gel sheet was laid flat on one of the faces. A hollow metal tube with an inner diameter of 50 mm was machined to make its edge sharp for punching out a circular disk sample from the sheet. The inner surface of the punch was straight but the outer surface was machined to achieve a sharp edge. The punch

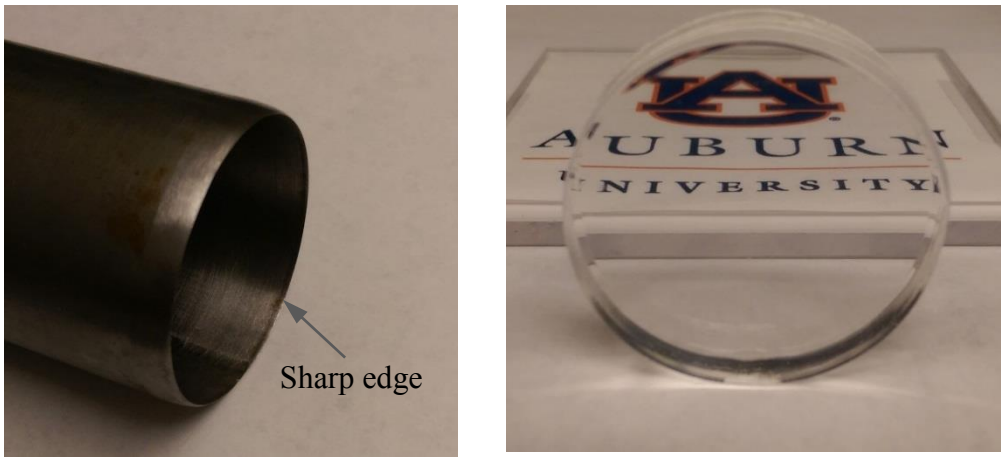

Figure 6.3: Hollow metal tube (left) used to punch out circular disk specimens and the resulting transparent disk shaped gel specimen (right).

was first heated to 80^{o}C in an oven, then pressed into the gel sheet at right angles and care was taken to keep the good transparency unaffected. The inner surface of the punch was

coated with hot water which lubricated the punch face and gel sheet interface. Figure 6.3 shows a photograph of the resulting circular disk specimen of diameter 50 mm.

6.3.2 Experimental Setup

The schematic of the DGS experimental setup used for disk under diametral compression tests is shown in Fig. 6.4. The specimen used for this experiment is a circular disk of diameter 50 mm and thickness 12.5 mm. The specimen was subjected to diametral compression as shown in the figure. An Instron 4465 universal testing machine was used for performing tests at three different crosshead speeds 0.02, 0.2 and 2 mm/sec as in tension, compression and shear tests reported in the earlier chapters. The optical setup

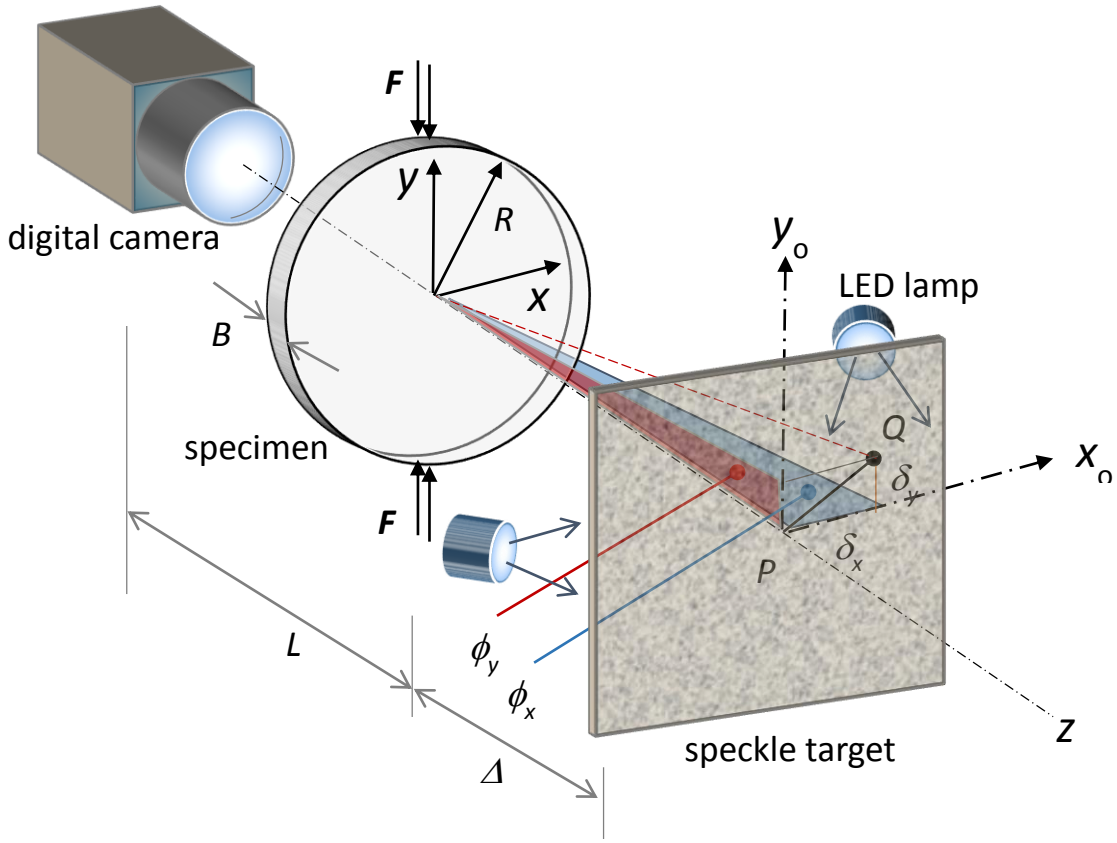

Figure 6.4: Schematic of the experimental setup used for studying polymer gel disk under diametral compression using Digital Gradient Sensing (DGS) method.

consisted of a target plate decorated with random black and white speckles placed at a distance Δ = 32 mm away from the mid-plane of the specimen.

A Point Grey digital camera (Grasshopper3 GS3-U3-41C6M; 2048 x 2048 pixels, monochrome, 10 bit camera) fitted with a 18-108 mm focal length zoom lens was used to record speckles on the target plane. The camera was at a distance of approximately 600 mm from the specimen. The speckle pattern was illuminated using two cool LED lamps to avoid light sources heating the sample during experiments. The digital camera was focused on the speckles through the transparent gel disk and a reference image was recorded before the sample was loaded. To ensure line loading, the disk was compressed by two polycarbonate blocks gripped in the standard testing machine fixtures. As the load increased, speckle images corresponding to different deformed states of the sample were recorded at regular time intervals (1-10 frames/sec) depending on the crosshead speed. The digitized speckle images recorded at different load levels were correlated with the reference image using the image analysis software ARAMIS. As described in the section on DGS methodology (Section 6.2), an array of in-plane speckle displacement components on the target plane (and hence the specimen plane) was evaluated and converted into local angular deflections of light rays ϕ_x and ϕ_y. A facet/sub-image size of 75 x 75 pixels and facet step size of 50 pixels was used to achieve correlation over the entire region of interest (scale factor = 0.026 mm/pixel and the data array size is 39 x 39). A relatively large facet size was needed due to large deformations suffered by the gel, particularly near the two loading points [27].

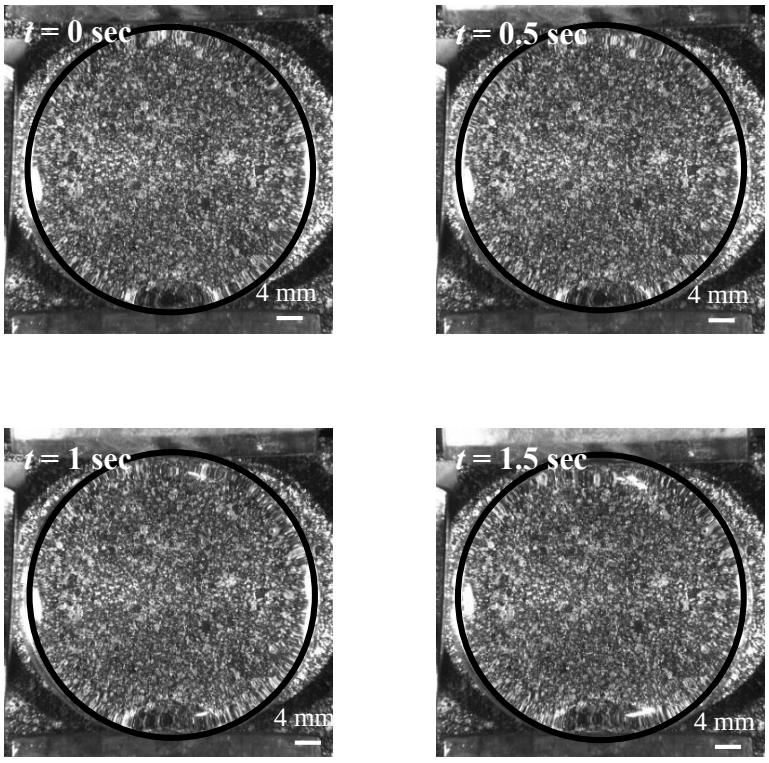

Figure 6.5: Speckle images recorded at different time intervals during the experiment done with a crosshead speed of 2 mm/sec.

6.3.3 Comparison of Measurements with Analytical Solution

When the deformed images of speckle pattern were correlated with the undeformed image using DIC, displacements δ_x and δ_y were obtained in the *x*- and *y*- directions, respectively. Angular deflections in the *x*-*z* and *y*-*z* planes ϕ_x and ϕ_y were obtained from δ_x and δ_y, respectively, and are proportional to stress gradients, see Eqs. (6.6) and (6.7) [41]. Figure 6.6 shows the resulting angular deflection contours of ϕ_x and ϕ_y for an

imposed displacement of 1.5 mm at three crosshead speeds 0.02, 0.2 and 2 mm/sec. An increase in the density of contours with crosshead speed is evident.

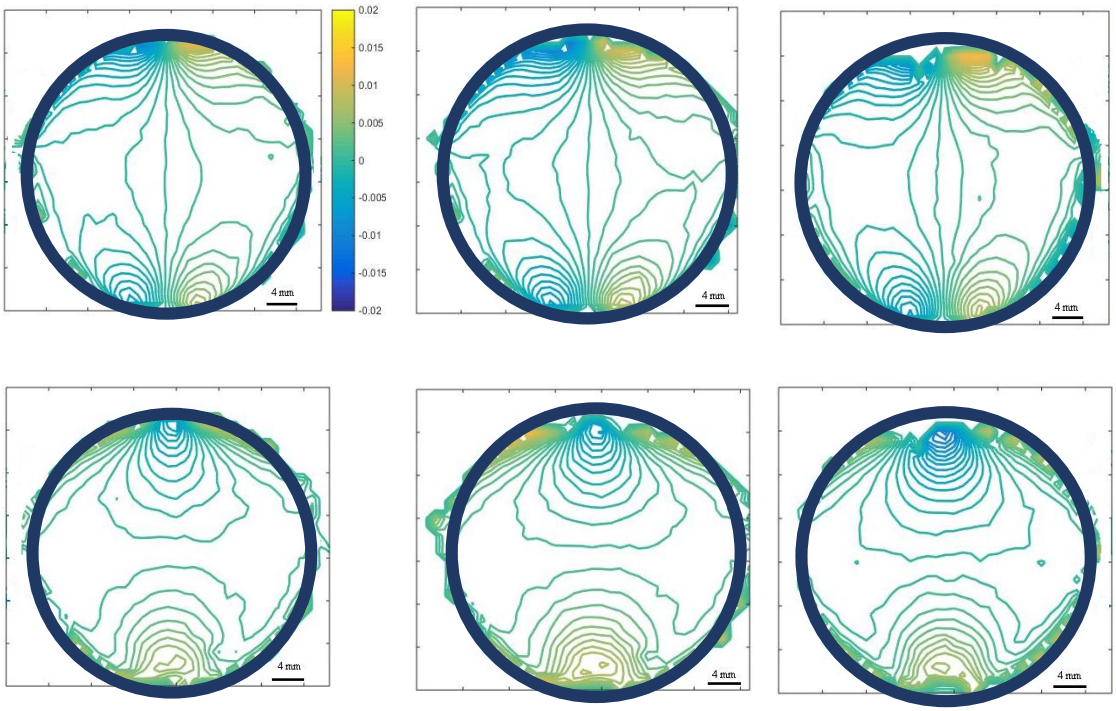

Figure 6.6: Measured ϕ_x (top) and ϕ_y (bottom) contours for a displacement of 1.5 mm at 0.02 (left), 0.2 (middle) and 2 mm/sec (right) respectively. Contour interval=7x10^{-4} radian.

The analytical expressions for normal stresses in an elastic disk under diametral compression [47] are,

$$\sigma_{xx} = -\frac{2F}{\pi}\left[\frac{(R-y)x^2}{r_1^4} + \frac{(R+y)x^2}{r_2^4} - \frac{1}{2R}\right] \tag{6.8}$$

$$\sigma_{yy} = -\frac{2F}{\pi}\left[\frac{(R-y)^3}{r_1^4} + \frac{(R+y)^3}{r_2^4} - \frac{1}{2R}\right]$$

where $r_{1,2} = \sqrt{x^2 + (R \mp y)^2}$, F is the applied load per unit thickness, R is the radius of the circular disk, x and y are the Cartesian coordinates as shown in Fig. 6.4. After the partial

derivatives of $(\sigma_{xx}+\sigma_{yy})$ are obtained, expressions for angular deflections ϕ_x and ϕ_y from Eqs. (6.6) and (6.7) become,

$$\phi_x = C_\sigma B \begin{bmatrix} \frac{2F}{\pi}\left(\frac{4x(R-y)^3}{\left(x^2+(R-y)^2\right)^3}+\frac{4x(R+y)^3}{\left(x^2+(R+y)^2\right)^3}\right)- \\ \frac{2F}{\pi}\left(\frac{2x(R+y)}{\left(x^2+(R+y)^2\right)^2}-\frac{4x^3(R-y)}{\left(x^2+(R-y)^2\right)^3}-\frac{4x^3(R+y)}{\left(x^2+(R+y)^2\right)^3}+\frac{2x(R-y)}{\left(x^2+(R-y)^2\right)^2}\right) \end{bmatrix} \quad (6.9)$$

$$\phi_y = C_\sigma B \begin{bmatrix} \frac{-2F}{\pi}\left(\frac{3(R+y)^2}{\left((R+y)^2+x^2\right)^2}-\frac{3(R-y)^2}{\left((R-y)^2+x^2\right)^2}+ \right. \\ \left. \frac{2(R-y)^3(2R-2y)}{\left((R-y)^2+x^2\right)^3}-\frac{2(R+y)^3(2R+2y)}{\left((R+y)^2+x^2\right)^3}\right)- \\ \frac{2F}{\pi}\left(\frac{x^2}{\left((R+y)^2+x^2\right)^2}-\frac{x^2}{\left((R-y)^2+x^2\right)^2}+ \right. \\ \left. \frac{2x^2(R-y)(2R-2y)}{\left((R-y)^2+x^2\right)^3}-\frac{2x^2(R+y)(2R+2y)}{\left((R+y)^2+x^2\right)^3}\right) \end{bmatrix} \quad (6.10)$$

In Fig. 6.7, the analytical contours from Eqs. (6.9) and (6.10) are plotted and compared with the corresponding experimental ones. Expectedly the analytical contours are highly symmetrical when compared to the experimental contours. These discrepancies can be attributed to deformation of the gel disk due to self weight and frictional contact. The

experimental contours are also distorted along the circumference due to edge effects during image analysis.

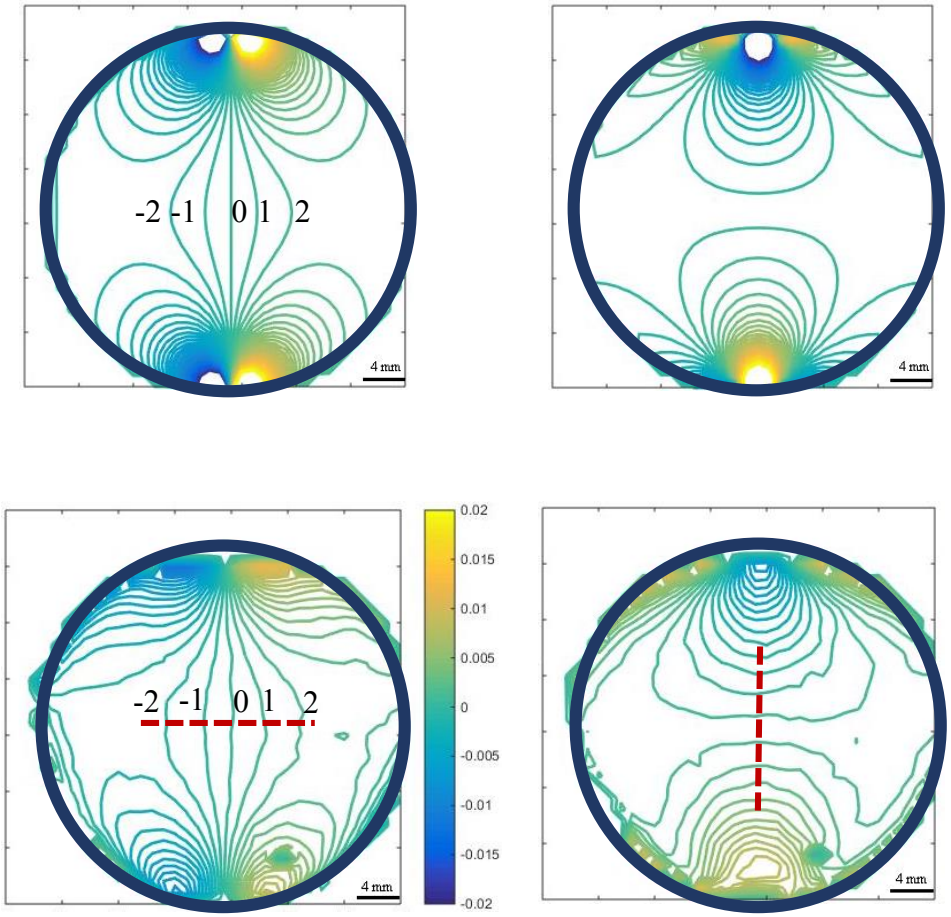

Figure 6.7: Comparison of analytical (top) and experimental (bottom) ϕ_x (left) and ϕ_y (right) contours for 0.02 mm/sec case at a load F = -0.98 N. Contour interval=7.5x10^{-4} radian.

Figure 6.8 shows comparison between experimental and analytical results for a load of 0.98 N. The experimental and analytical angular deflections ϕ_x and ϕ_y are plotted along $\frac{x}{R}$ and $\frac{y}{R}$, respectively, in the central region of the disk where stress concentration effects and edge effects are minimum. A rather good agreement is observed between the analytical

solutions and experimental measurements in the region $\frac{x}{R} = \pm 0.5$ and $\frac{y}{R} = \pm 0.5$ from ϕ_x and ϕ_y respectively at all crosshead speeds.

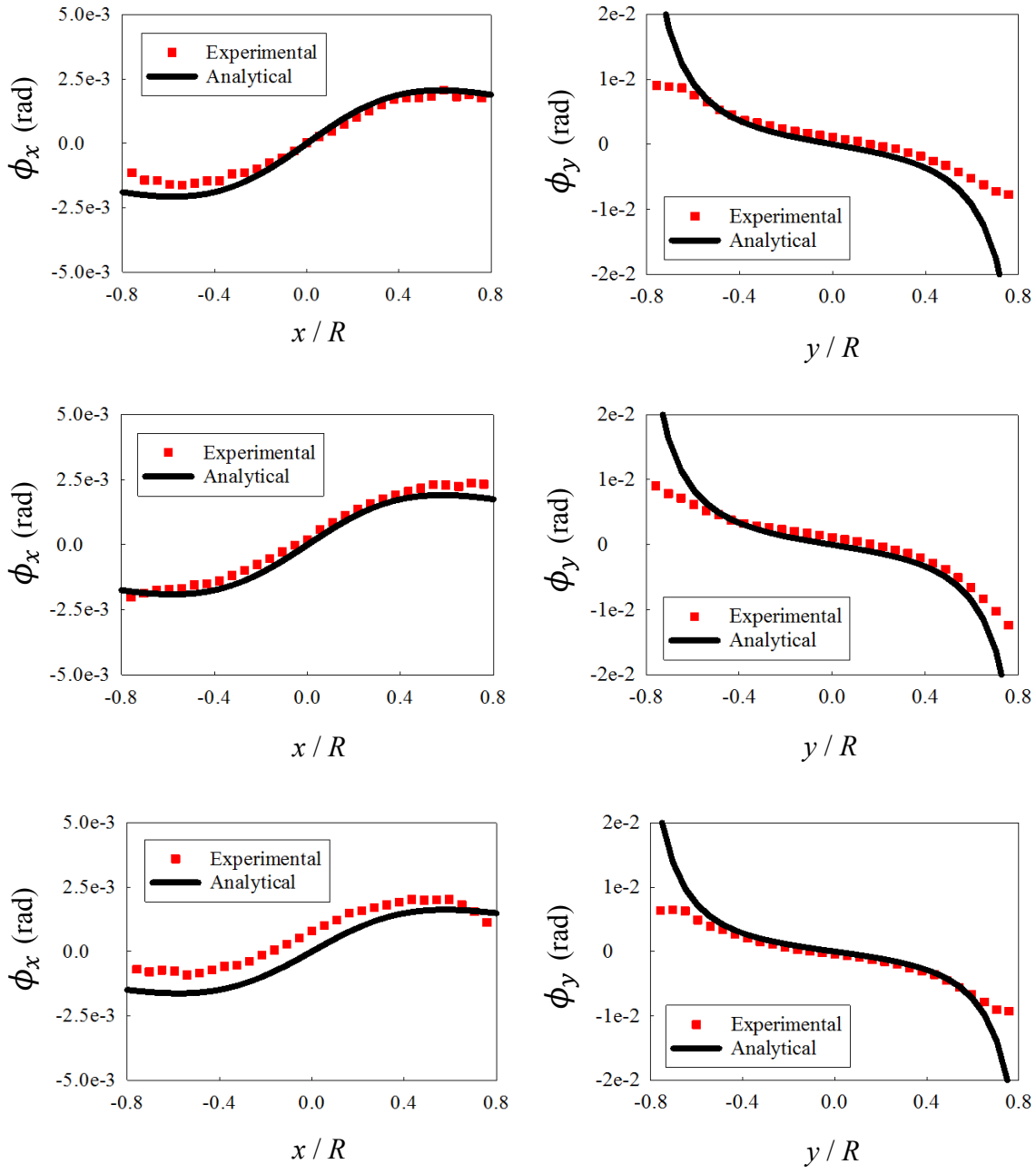

Figure 6.8: Comparison of experimental and analytical ϕ_x (left) and ϕ_y (right) values for 0.02 mm/sec (top), 0.2 mm/sec (middle) and 2 mm/sec (bottom) for a load F = -0.98 N.

6.3.4 Evaluation of Elasto-Optical Constant, C_σ

Angular deflections ϕ_x and ϕ_y for each facet/sub-image were obtained by dividing displacements δ_x and δ_y with Δ after correlating speckle images. The stress gradients at a location can be evaluated if the applied load *F*, thickness *B*, radius *R*, *x*- and *y*-coordinates are known. All the parameters in the expressions for angular deflections (Eqs. (6.9) and (6.10)) are known except the elasto-optical constant C_σ which can be extracted using a linear least-squares analysis separately for both ϕ_x and ϕ_y. The C_σ values were extracted at different load levels and then "averaged". To minimize edge effects, data along the *x*-axis from ϕ_x field and *y*-axis from ϕ_y field over $\pm R/2$ from the center of the disk was used in the least-squares analysis. This data path is indicated by the dotted red lines in Fig. 6.7. The results are tabulated in Table 6.2. The elasto-optical constant varies from -1.18 to -1.47 mm^2/N for a crosshead speed variation between 0.02 and 2 mm/sec. The sign of stress-optical constant can be understood by using Eq. (6.2). When the material is subjected to tension, density decreases and hence the refractive index also decreases. On the other hand, if the material is subjected to compression, density increases and as a result refractive index also increases. In both these cases, the sign of the stress-optic constant will be negative. From Eq. (6.5), as the elastic modulus is increasing with the crosshead speed, it is evident that the elasto-optical constant for the gel should be inversely proportional to the crosshead speed. This can be observed from the C_σ values shown in Table 6.2.

Crosshead speed (mm/sec)	Elasto-optic constant C_σ (mm^2/N)
2.0	-1.18 ± 0.071
0.2	-1.28 ± 0.037
0.02	-1.47 ± 0.061

Table 6.2: Dependence of elasto-optical constant on the crosshead speed.

Chapter 7: Line-Load on a Gel Block Edge: The Flamant Problem

In this chapter, stress concentration due to a line-load acting on the edge of a planar gel sheet, or the so-called Flamant problem, is studied using DGS. Details regarding sample preparation, experimental setup used, measurements made, and comparison between experimental and analytical quantities are included. A finite element analysis has also been undertaken to complement optical measurements.

7.1 Sample Preparation Details

Rectangular gel sheets devoid of air bubbles and smooth surface finish were prepared as discussed in the previous chapters. A hot-wire cutter was used to cut rectangular blocks of dimensions 50 mm x 50 mm x 12.5 mm with square edges as shown in Fig. 7.1.

Figure 7.1: Photograph of a rectangular transparent block used for studying Flamant problem

7.2 Experimental Setup

A schematic of the experimental setup used for studying the effects of a line-load acting on the edge of a planar gel sheet is shown in Fig. 7.2. The specimen resting on a rigid platform was subjected to a line-load using a sharp single edge razor blade held in the Instron 4465 testing machine grips. Tests at three different crosshead speeds, 0.02, 0.2 and 2 mm/sec were performed. The setup also consisted of a digital camera and a target plate painted with random white and black speckles placed at a distance Δ = 32 mm behind specimen mid-plane, as shown.

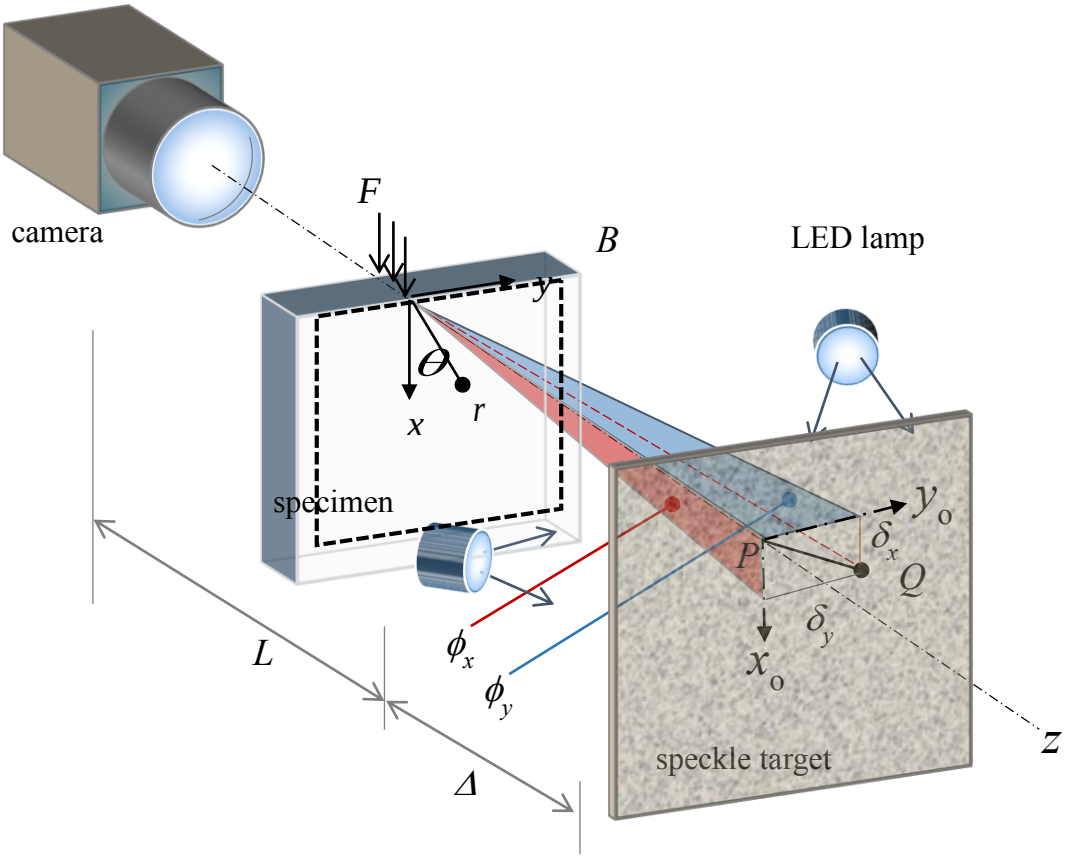

Figure 7.2: Schematic of the experimental setup used for studying stress concentration caused by a line-load acting on the edge of a polymer gel block with DGS.

A Point Grey digital camera (Grasshopper3 GS3-U3-41C6M) fitted with a 18-108 mm focal length zoom lens was used to record speckles on the target plate through the specimen and was situated at a distance of ~600 mm from the specimen. The speckle pattern on the target plate was illuminated using two cool LED light sources to prevent heating of the sample during experiment. A reference image was recorded before the sample was loaded. The sharp edge of the razor blade held in one of the grips of the testing machine was displaced into the gel block at a prescribed crosshead speed. As the load

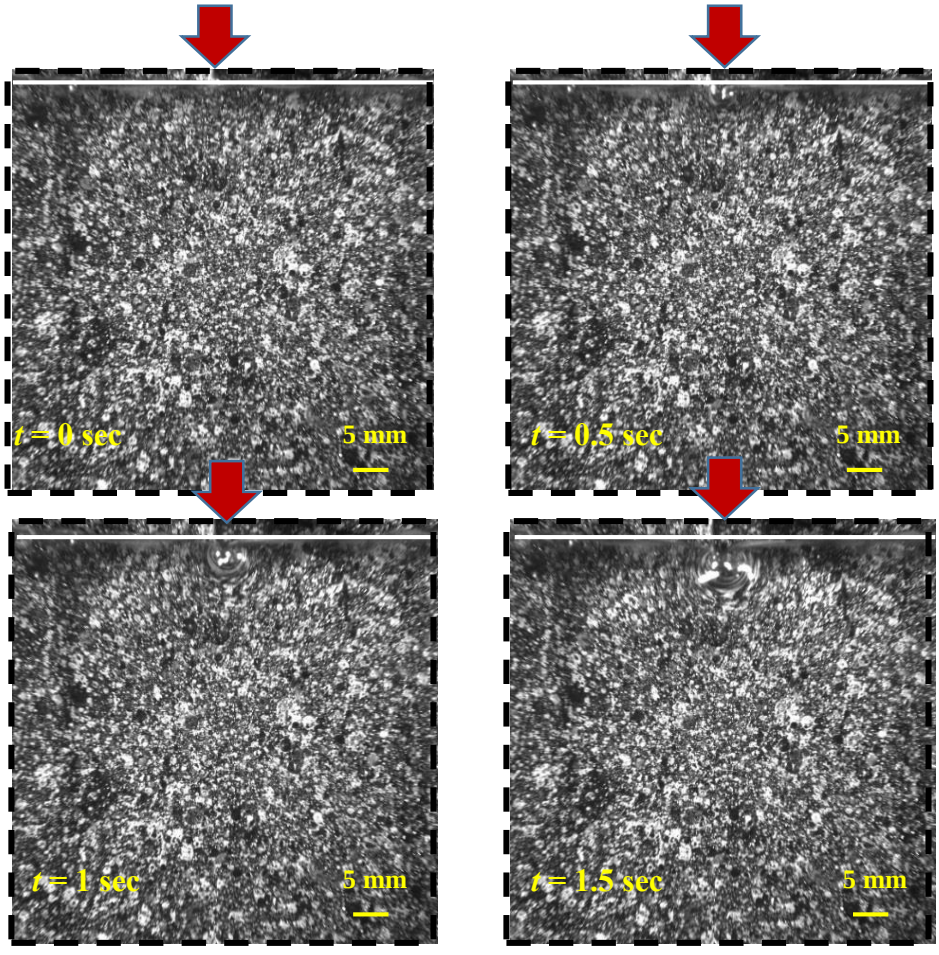

Figure 7.3: Speckle images taken at different time intervals during the experiment done at a crosshead speed of 2 mm/sec (red arrow indicates loading point and yellow box indicates specimen deformation due to applied load).

increased, speckle images corresponding to various deformed states of the gel block were recorded at regular time intervals (1-10 frames/sec) depending on the crosshead speed. A few representative speckle images from this experiment are shown in Fig. 7.3. The red arrow represents the loading point. White horizontal line represents the edge of the sample. Yellow box highlights the region of severe deformations near the tip of the razor blade. The speckles appear blurry near the loading point due to large deformation, whereas they appear relatively unaffected at far-away locations.

The digitized speckle images (2048 x 2048 pixels) recorded at different load levels were correlated with the one corresponding to the reference condition using ARAMIS. As described in Chapter 6, an array of in-plane speckle displacements on the target plane (and

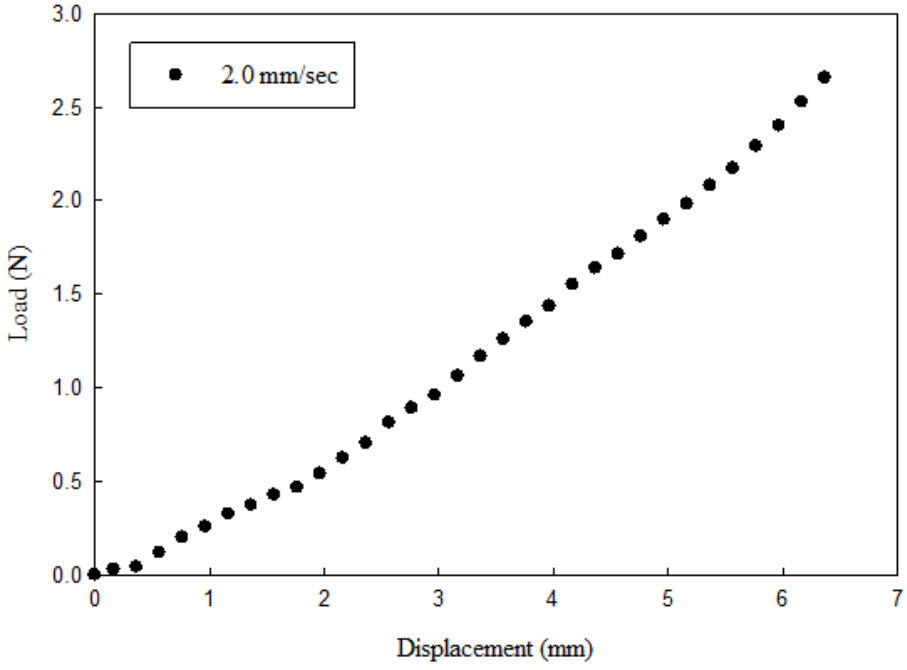

Figure 7.4: Load vs displacement response for Flamant problem at 2 mm/sec crosshead speed.

hence the specimen plane) was evaluated and converted into local angular deflections ϕ_x and ϕ_y. A facet/sub-image size of 75 x 75 pixels and facet step size of 50 pixels (scale factor = 0.021 mm/pixel and the data array size = 39 x39) was used during analysis. Figure 7.4 shows the load vs displacement response recorded for Flamant loading at 2 mm/sec crosshead speed.

7.3 Comparison of Measurements with Analytical Solutions

Speckle images were recorded during deformation of the gel block and correlated with the undeformed image using DIC to obtain displacement components δ_x and δ_y in the *x*- and *y*- directions, respectively. Knowing the gap between the specimen mid-plane and the target plate, the angular deflections in the *x*-*z* and *y*-*z* planes ϕ_x and ϕ_y were evaluated from δ_x and δ_y, respectively, and are proportional to stress gradients (Eqs. (6.6) and (6.7)):

$$\phi_x \approx \frac{\delta_x}{\Delta} = C_\sigma B \frac{\partial(\sigma_{xx} + \sigma_{yy})}{\partial x} \tag{7.1}$$

$$\phi_y \approx \frac{\delta_y}{\Delta} = C_\sigma B \frac{\partial(\sigma_{xx} + \sigma_{yy})}{\partial y} \tag{7.2}$$

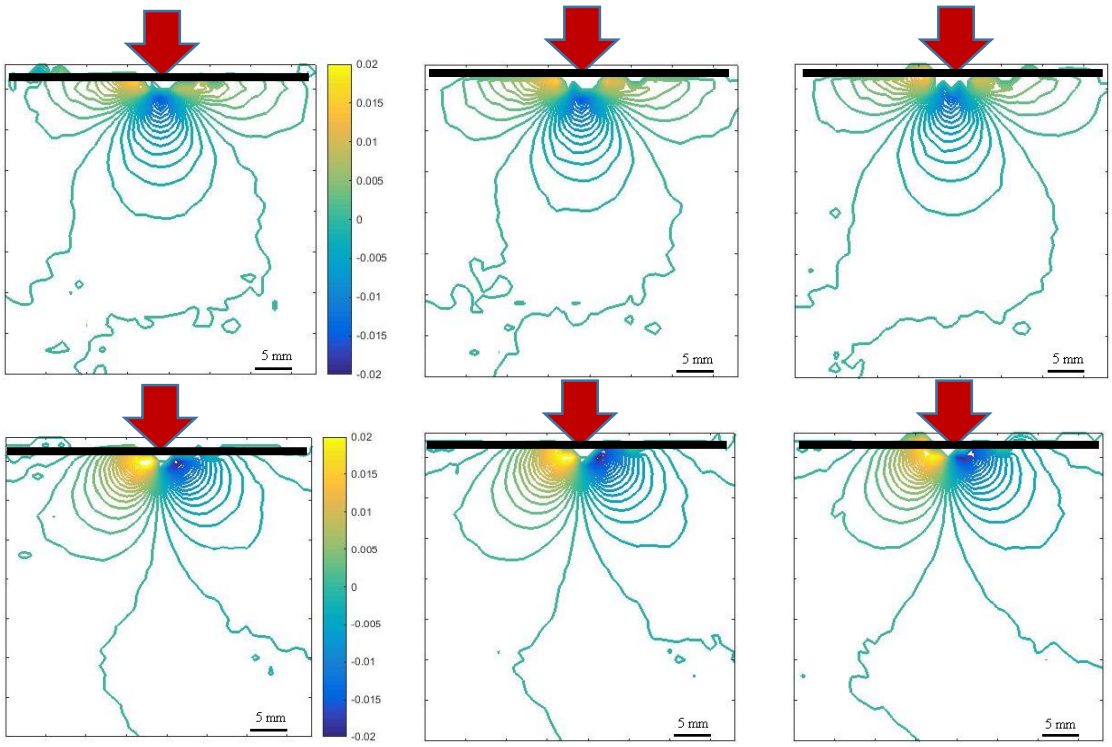

Figure 7.5: Measured ϕ_x (top) and ϕ_y (bottom) contours for a displacement of 1.5 mm at 0.02 (left), 0.2 (middle) and 2 mm/sec (right) respectively. Contour interval = 1 x 10^{-3} radians. Black horizontal line indicates sample edge and red arrow indicates loading point.

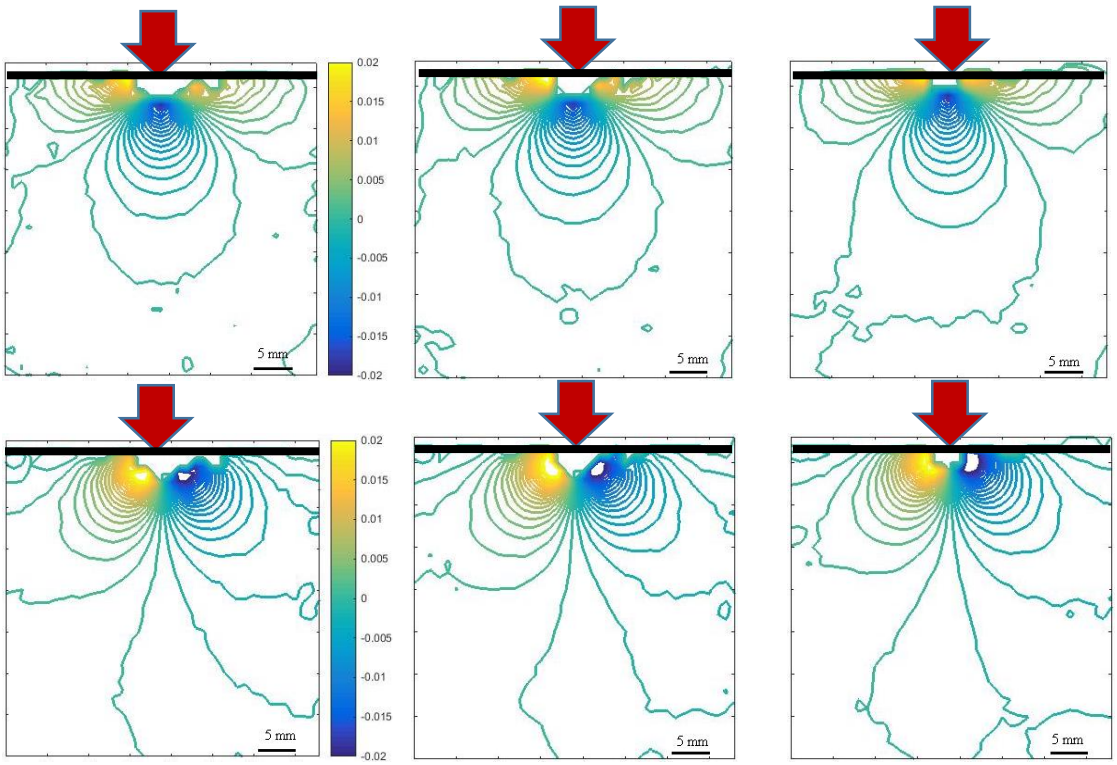

Figure 7.6: Measured ϕ_x (top) and ϕ_y (bottom) contours for a displacement of 2 mm at 0.02 (left), 0.2 (middle) and 2 mm/sec (right), respectively. Contour interval = 1 x 10^{-3} radians.

From Figs. 7.5 and 7.6, it can be observed that the number of contours increases with the applied displacement from 1.5 to 2 mm. The effect of crosshead speed can also observed at both displacement levels in the form of increase in size (and hence number) of contours. Near the loading point the contours are of reasonably good quality, whereas edge effect persist near the side and bottom edges of the sample. Expressions for a line-load acting on the edge of an elastic half-space is described by the Flamant problem [47, 48, 49] are given in Eq. (7.3). The combined normal stress is given by,

$$(\sigma_{xx}+\sigma_{yy})=\sigma_{rr}=-\frac{2F}{\pi B}\frac{\cos(\theta)}{r},\sigma_{\theta\theta}=0,\sigma_{r\theta}=0, \qquad (7.3)$$

where F is the applied load, B is the thickness of the half-space and (r,θ) are the polar coordinates as shown in Fig. 7.2. Knowing,

$$\phi_{x;y} = C_\sigma B \frac{\partial(\sigma_{rr})}{\partial x;\partial y} \tag{7.4}$$

The analytical expressions for angular deflections ϕ_x and ϕ_y can be obtained as,

$$\phi_x = C_\sigma B \frac{2F}{\pi B} \frac{\cos(2\theta)}{r^2} \text{ and } \phi_y = C_\sigma B \frac{2F}{\pi B} \frac{\sin(2\theta)}{r^2} \tag{7.5}$$

The contours of angular deflections from the analytical solutions are plotted in Fig. 7.7 at the same contour increments for comparative purposes. A qualitative agreement is evident between the two despite the finite geometry used in experiments. Very close to the loading point, there are large deformations due to the stress singularity and hence these regions could not be correlated. Elsewhere, the agreement is good despite the edge effects and experimental difficulties while sizing the specimen.

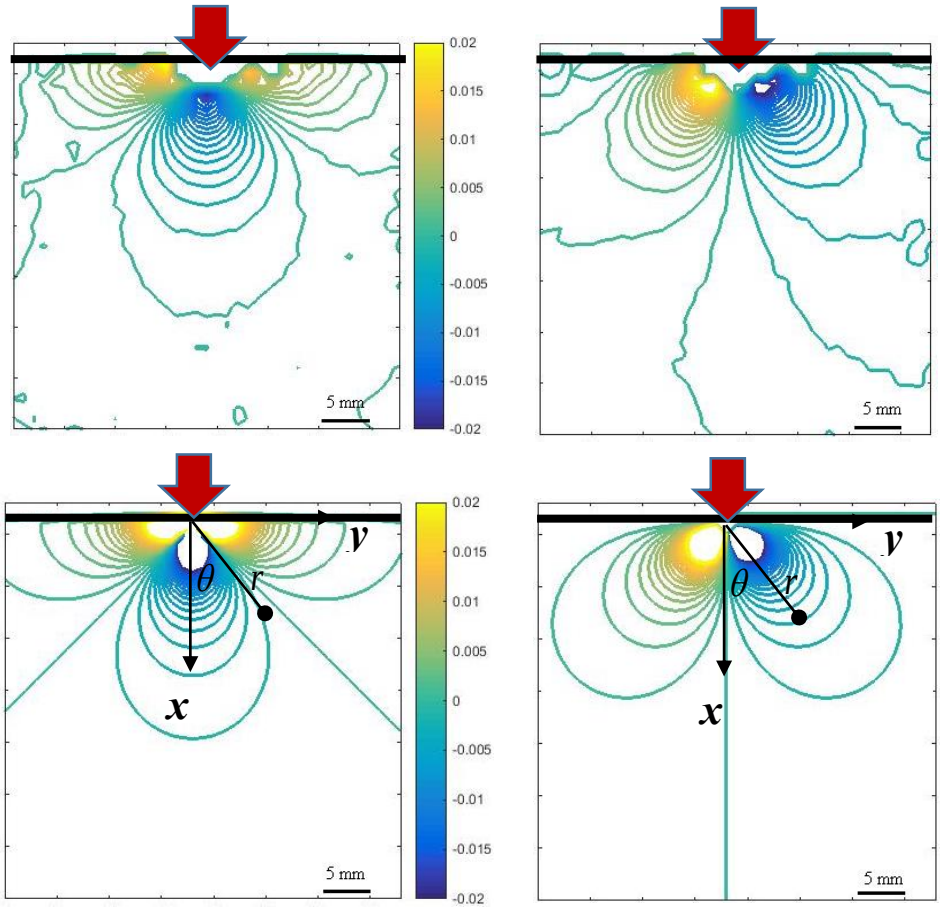

Figure 7.7: Comparison of experimental (top) and analytical (bottom) ϕ_x (left) and ϕ_y (right) contours for 0.02 mm/sec case at a load of 0.55 N. Contour interval = 1×10^{-3} radian.

7.4 Finite Element Simulations

A finite element simulation of the polymer gel block was performed using ABAQUS software package. The model (Fig. 7.8) was discretized into 221184 hexahedral (C3D8RH) elements and 235225 nodes to simulate the mechanical response of the gel.

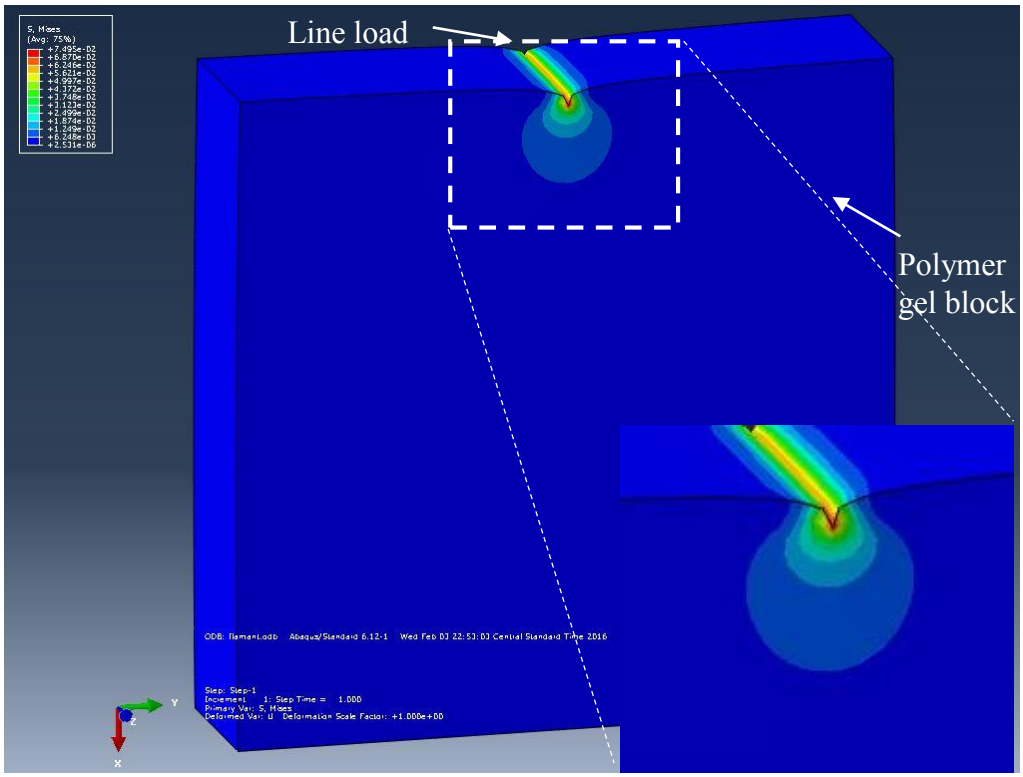

Figure 7.8: Finite element model (Von mises stress contour plot) of a line-load acting on the edge of a planar polymer gel block.

The choice of element type was based on the recommendations in Ref. [50] for incompressible materials. The model was subjected to displacement boundary condition on the top of the gel block and all the bottom nodes were assumed fixed. The stress-strain response of the material was from Eq. (3.7) for the gel.

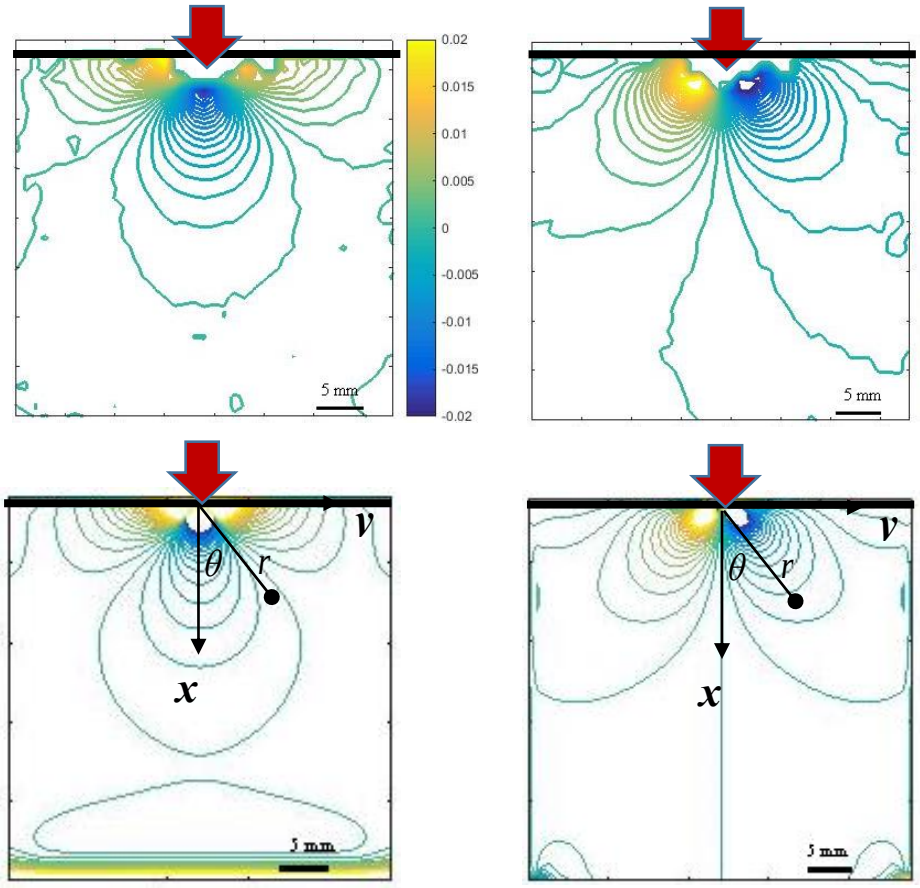

Figure 7.9: Comparison of experimental (top) and FEA (bottom) ϕ_x (left) and ϕ_y (right) contours for 0.02 mm/sec case for a displacement of 2 mm. Contour interval = 1×10^{-3} rad.

In the post-processing stage, spatial derivatives of $(\sigma_{xx} + \sigma_{yy})$ were computed in the *x*- and *y*- directions, respectively, using an in-built differentiation scheme in ABAQUS. As shown in Fig. 7.9, angular deflections were obtained for the simulated results knowing numerically obtained stress gradient data, elasto-optical constant of the gel and the thickness of the sample.

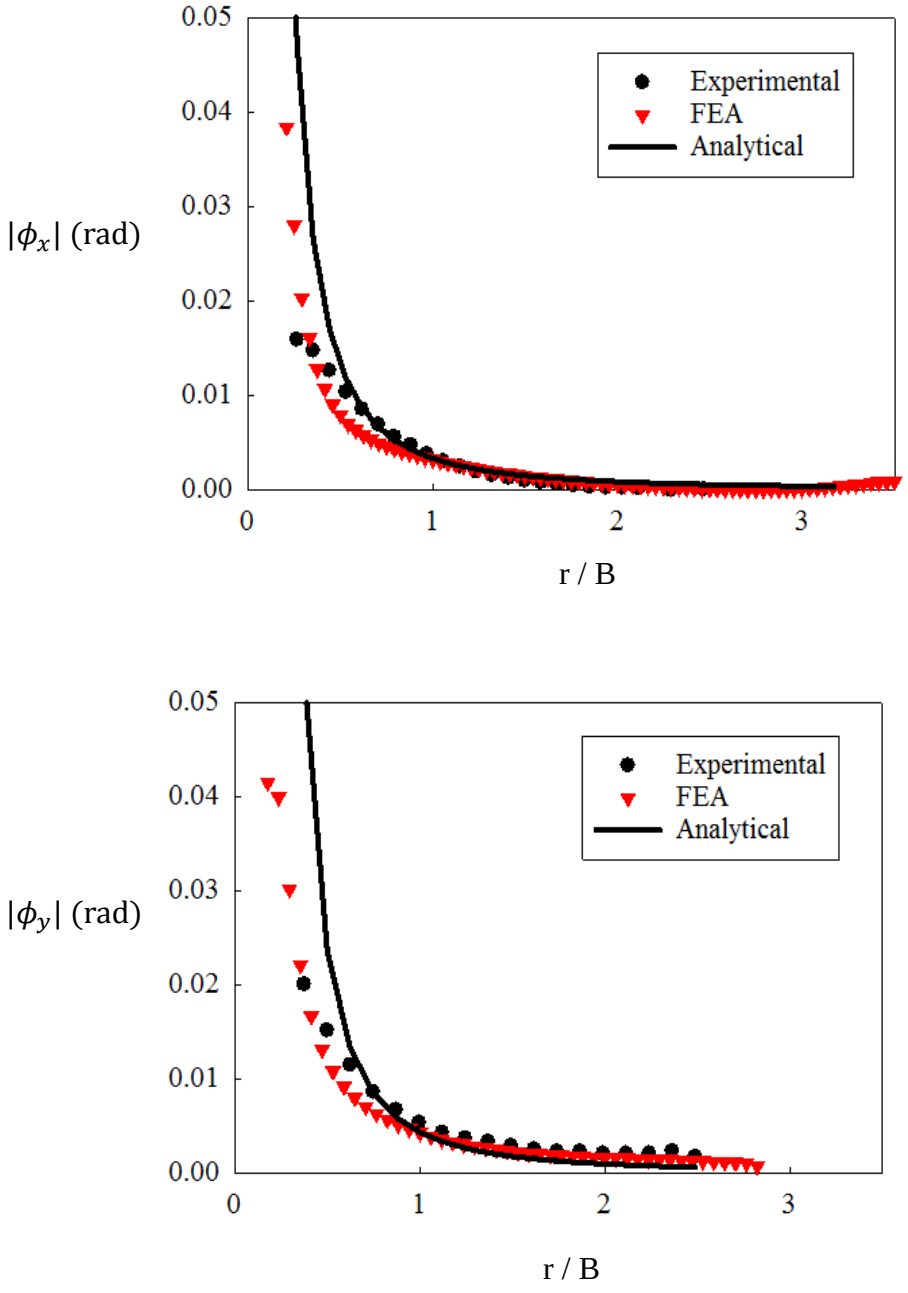

Figure 7.10: Comparison of experimental and FEA values along θ = 0° and θ = 45° for ϕ_x (top) and ϕ_y (bottom) respectively as a function of radial distance normalized with respect to thickness of the sample for 0.02 mm per sec case for a displacement of 2 mm.

In Fig. 7.10, the angular deflections from numerically obtained stress gradient data were compared with DGS. The angular deflection values from simulations and experiments are plotted along θ = 0° and Θ = 45° for ϕ_x and ϕ_y, respectively, as a function of radial distance (r) normalized by the sample thickness (B). There is a reasonably good agreement between the two sets outside the anticipated 3D zone of r/B = 0.5. The analytical results are also included for completeness (solid line).

7.5 Short Term Relaxation

Relaxation of the gel block was expected during loading events that typically lasted several seconds. The effect of this on optical measurements (or stress gradients) was investigated by performing a Flamant experiment for a constant imposed displacement. A polymer gel block with dimensions shown in Fig. 7.11 was subjected to a line-load using a razor blade displaced into the sample edge by 5 mm. (Note that the edge of the gel

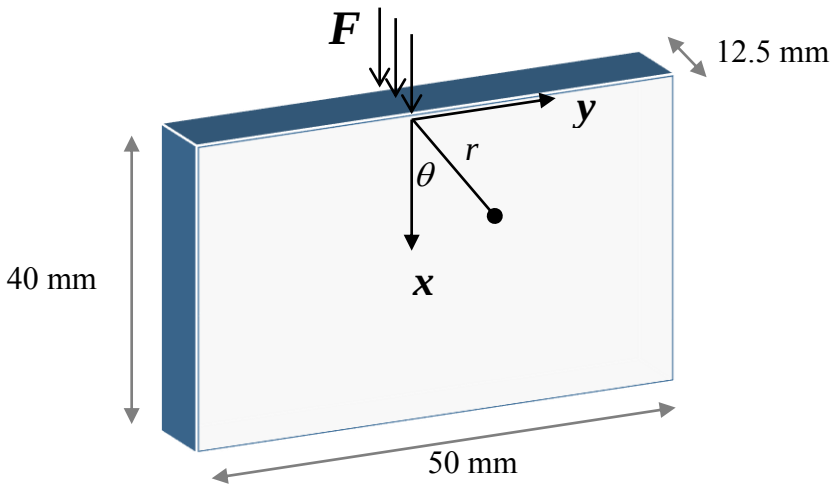

Figure 7.11: Schematic of a polymer gel block used to check for relaxation.

remained uncut by the blade even at this amount of displacement.) In this condition, the speckles on the target were recorded at 50 fps for several seconds.

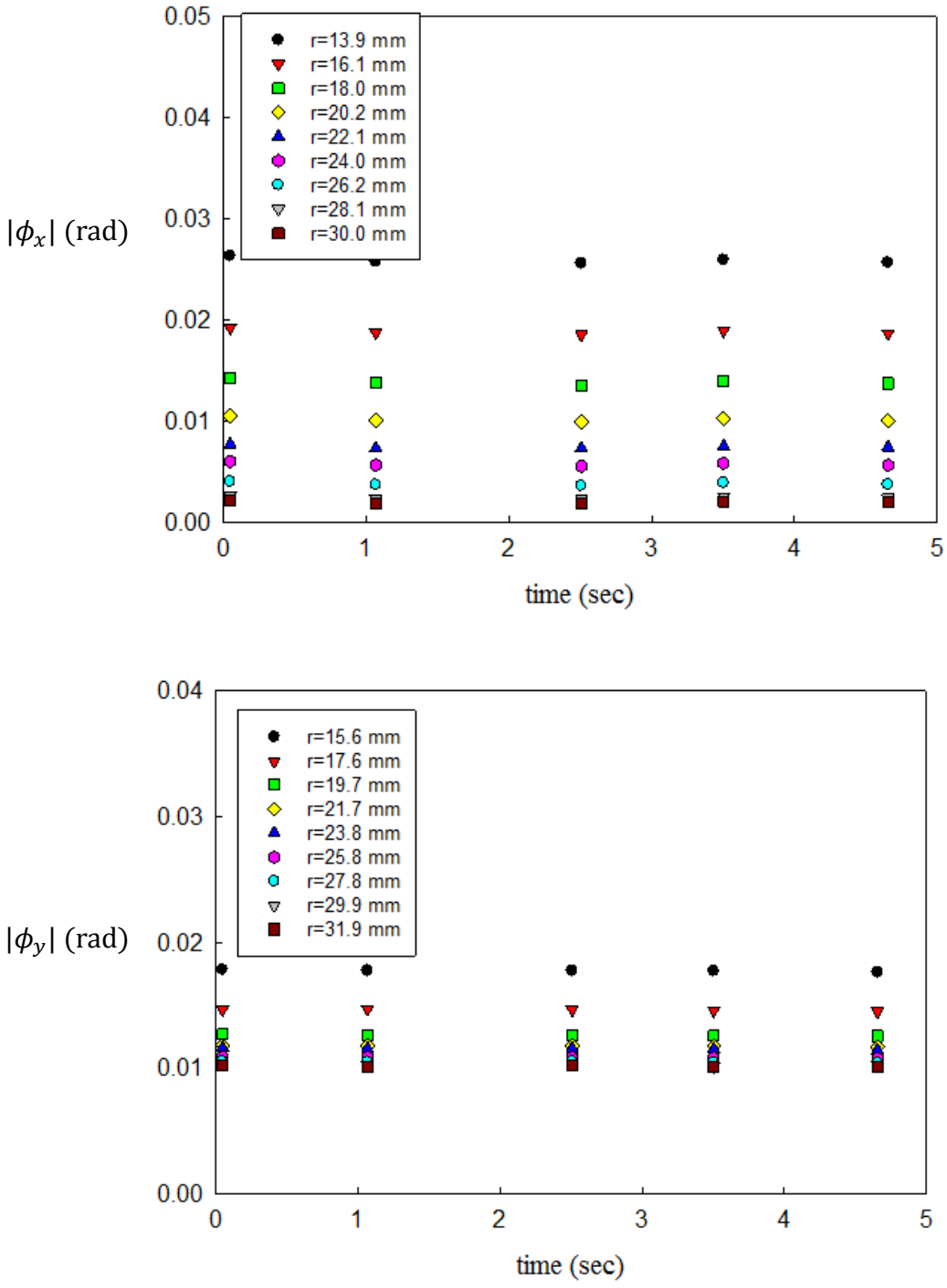

Figure 7.12: Variation of ϕ_x and ϕ_y values at different radial distances from the razor tip with time for an imposed displacement of 5 mm.

Using displacements δ_x and δ_y obtained by correlating each of the deformed images with the one in the undeformed state, ϕ_x and ϕ_y fields were obtained. Then, angular deflection data was measured along $\theta = 0^o$ for ϕ_x and $\theta = 45^o$ for ϕ_y and at different radial distances from the loading point at different time instants *t* after the razor blade had been displaced into the gel by 5 mm. From the measured data in Fig. 7.12, it can be seen that the measurements are essentially constant with respect to time at various radial locations. Hence it was concluded that no change in the measured field was observed for the gel over typical measurement times used in this study.

.

Chapter 8: Small Circular Hole in a Large Tensile Sheet

This chapter provides details regarding DGS method to study classical stress concentration problem of a small circular hole in a large gel sheet subjected to uniaxial tension. This has been investigated rather frequently in the literature. For example, Andersson et al. studied the fracture behavior (stress-intensity factors or (SIFs)) at the tips of a star-shaped contour formed in an infinite tensile sheet with hole [51]. Yan et al. compared the SIFs of a rectangular tensile plate with a single edge crack with that for a crack emanating from an edge of a semi-circular cut-out [52]. Mallick et al. observed the effects on the tensile strength of sheet molding compound (SMC-R50) with the hole stress concentration effects and its mitigation [53].

In the following, particulars about sample preparation, experimental setup, measurements and comparison between measured and analytical quantities near a circular hole in a tensile gel sheet are included. The stress gradient fields are measured using the DGS methodology. The measurements are compared with the analytical counterparts available in the literature.

8.1 Sample Preparation Details

Rectangular gel sheets (6.05 mm thick in this case) devoid of air bubbles and of good surface finish were prepared following the procedure outlined earlier. A hotwire

cutter was used to cut a sample of dimensions 90 mm x 50 mm. A hollow metal tube with an outer diameter (6.3 mm) was machined to make its (inside) edge sharp to punch a circular hole in the middle of the gel sheet. The punch was first heated to 80^{o}C and then carefully pressed into the gel sheet at right angles as it was lying flat on a polycarbonate substrate. The outer surface of the punch was lubricated with hot water while punching the hole. The resulting sample with a circular hole in the gel specimen is shown in Fig. 8.1.

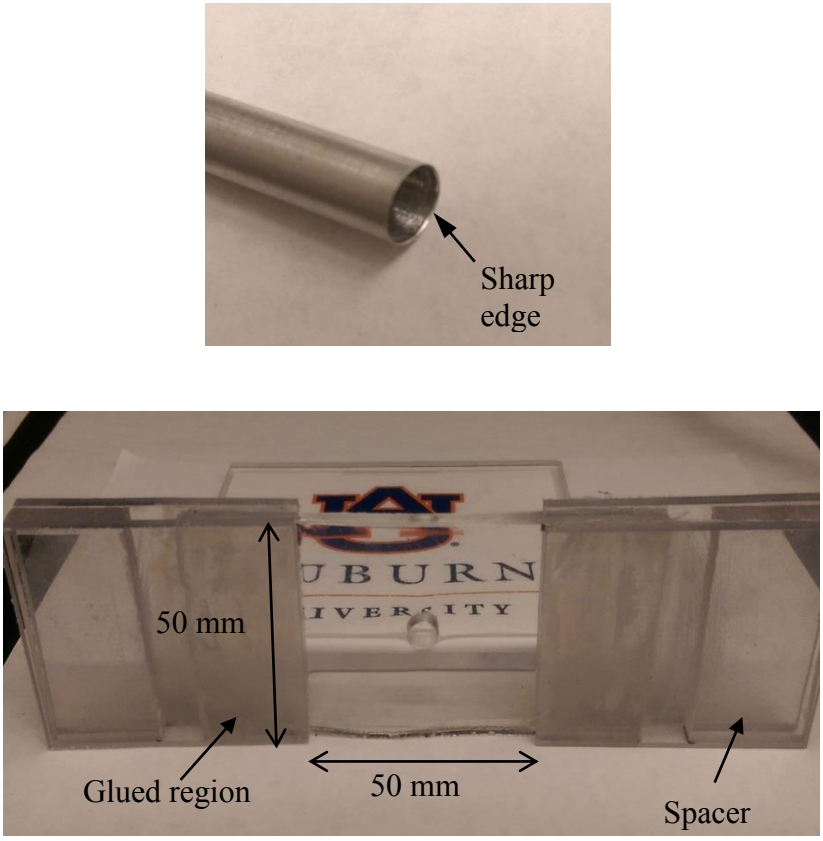

Figure 8.1: Hollow metal tube (top) used to punch out a circular hole and gel sheet sample with a circular hole glued to end tabs (bottom) for conducting tension tests.

The gel sheet with the circular cut-out was then gripped using the method outlined in Chapter 3 for carrying out tension tests (see Section 3.3). That is, in order to grip the

sample in the Instron machine, polycarbonate end tabs were glued to the gel sheet with Loctite 401 glue over a distance of 20 mm along the length (90 mm) direction on both sides of the sample.

In Fig. 8.1, the gel sheet glued to the end tabs made of polycarbonate is shown. Spacers used between the end tabs were also made of polycarbonate and were of the same thickness as the sample. This prevented thickness wise compression of the gel sheet. The entire assembly was gripped in the loading machine and subjected to tension.

8.2 Experimental Setup

A schematic of the experimental setup used in these tests is shown in Fig. 8.2. The specimen used was a rectangular sheet of dimensions 90 x 50 x 6.05 mm^3 with a circular hole of diameter 6.3 mm. The specimen was subjected to displacement controlled tensile loading at three different crosshead speeds 0.02, 0.2 and 2 mm/sec. A target plate painted with random white and black speckles placed at a distance $\Delta = 32$ mm away from specimen mid-plane.

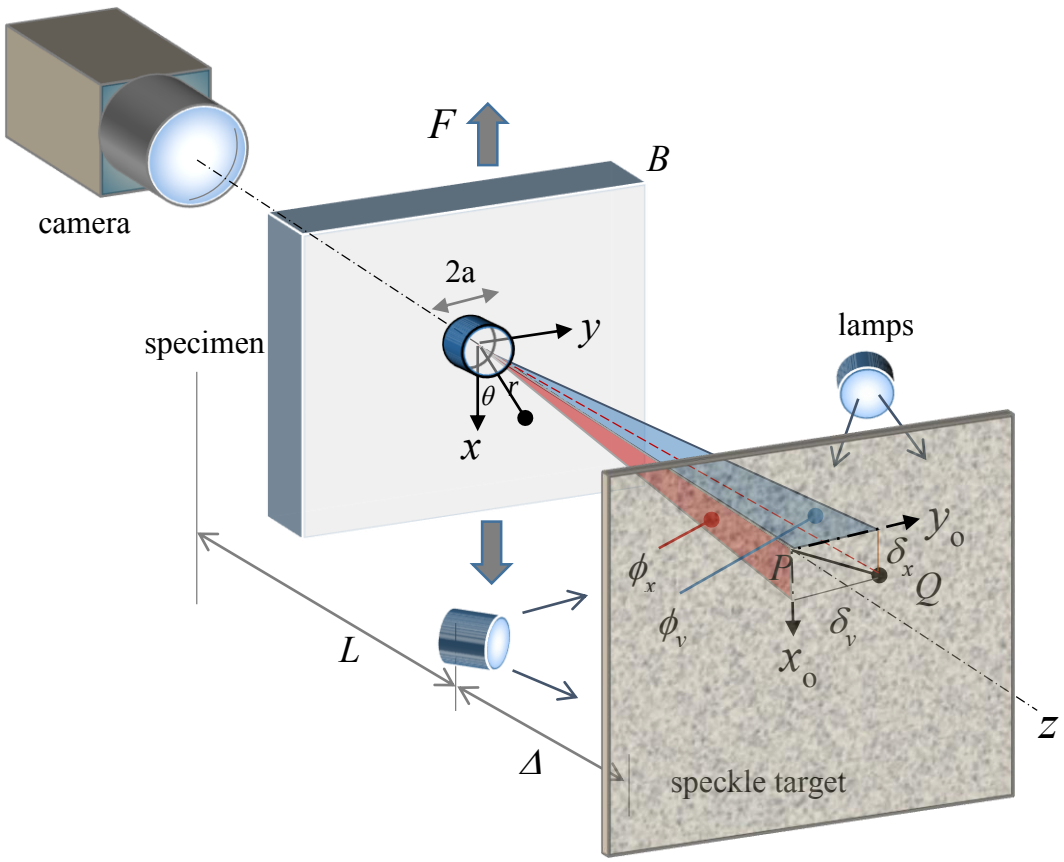

Figure 8.2: Schematic of the experimental setup used for studying stress concentration caused small circular hole in a large tensile polymer gel sheet with DGS.

A Point Grey digital camera (Grasshopper3 GS3-U3-41C6M) fitted with a 18-108 mm focal length zoom lens which was used to record images and was situated at a distance of approx. 550 mm from the specimen. The speckle pattern on the target plate was illuminated using two cool LED lamps. The digital camera was focused on the speckles through the transparent sheet sample and the reference image (undeformed image) was recorded before the sample was loaded. As the load increased gradually, speckle images (deformed images) were recorded at regular time intervals (1-10 frames/sec). The digitized speckle images (2048 x 2048 pixels) recorded at different stages of loading were correlated

with the one corresponding to the reference image using ARAMIS. As described previously, an array of in-plane speckle displacements on the target plane (and hence the specimen plane) was evaluated and converted into local angular deflections of light rays ϕ_x and ϕ_y. A facet/sub-image size of 50 x 50 pixels and facet step size of 30 pixels (scale factor = 0.030 mm/pixel and the data array size = 66 x 59) was used in this analysis. Figure 8.3 shows speckle images recorded at different stages of deformation for 2 mm/sec crosshead speed. The deformation occurs close to the circular hole acting as a stress

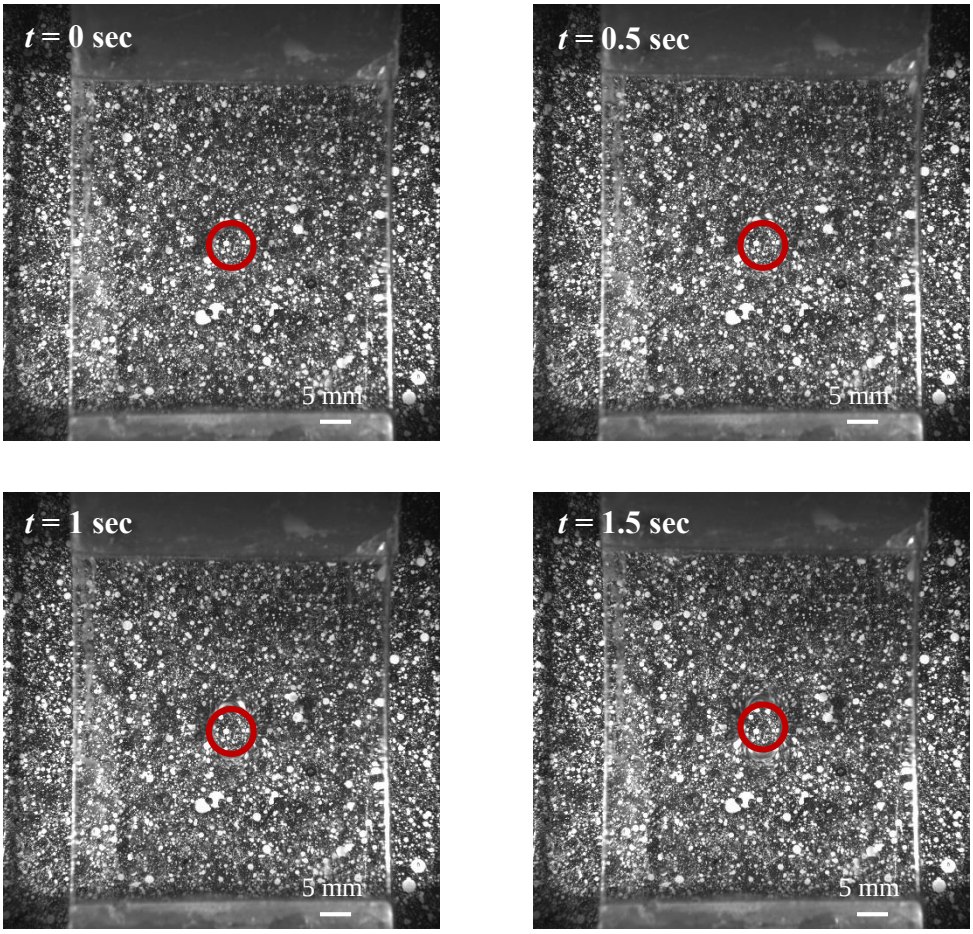

Figure 8.3: Speckle images recorded at different time intervals during the gel sheet stretching experiment at a crosshead speed of 2 mm/sec.

concentration in the tensile sheet sample. The hole is highlighted with a red circle in the figure for clarity.

8.3 Comparison of Measurements with Analytical Solution

When speckle patterns corresponding to the deformed states of the gel were correlated with the reference state, speckle shifts δ_x and δ_y in the *x*- and *y*-directions, respectively, were obtained. The angular deflections ϕ_x and ϕ_y in the *x*-*z* and *y*-*z* planes from δ_x and δ_y, respectively, are proportional to stress gradients as discussed in Chapter 6 (see, Eqs. (6.6) and (6.7)). Figure 8.4 shows the resulting angular deflection contours of ϕ_x and ϕ_y for a crosshead displacement of 1.3 mm at speeds 0.02, 0.2 and 2 mm/sec, respectively.

The analytical expressions for a stress concentration problem of a small circular hole in a large tensile sheet [47, 54] are,

$$\sigma_{rr} = \frac{\sigma}{2}\left(1-\frac{a^2}{r^2}\right)+\frac{\sigma}{2}\left(1+\frac{3a^4}{r^4}-\frac{4a^2}{r^2}\right)\cos 2\theta \tag{8.1}$$

$$\sigma_{\theta\theta} = \frac{\sigma}{2}\left(1+\frac{a^2}{r^2}\right)-\frac{\sigma}{2}\left(1+\frac{3a^4}{r^4}\right)\cos 2\theta \tag{8.2}$$

$$\sigma_{r\theta} = -\frac{\sigma}{2}\left(1-\frac{3a^4}{r^4}+\frac{2a^2}{r^2}\right)\sin 2\theta \tag{8.3}$$

where σ is the applied stress, a is the radius of the circular hole, (r, θ) are the polar coordinates as shown in Fig. 8.2. Knowing that

$$\sigma_{xx} + \sigma_{yy} = \sigma_{rr} + \sigma_{\theta\theta} \tag{8.4}$$

and

$$\cos 2\theta = \cos^2(\theta) - \sin^2(\theta)$$

$$x = r\cos(\theta),\ y = r\sin(\theta) \tag{8.5}$$

$$r^2 = x^2 + y^2$$

we can obtain Eq. (8.6) as

$$(\sigma_{xx} + \sigma_{yy}) = (\sigma_{rr} + \sigma_{\theta\theta}) = \sigma\left(1 - \frac{2a^2}{(x^2+y^2)^2}(x^2 - y^2)\right) \tag{8.6}$$

The expressions for angular deflections ϕ_x and ϕ_y from Eqs. (6.6) and (6.7) can be obtained as,

$$\phi_x = C_\sigma B(-2\sigma a^2)\frac{(6xy^2 - 2x^3)}{(x^2+y^2)^3} \tag{8.7}$$

$$\phi_y = C_\sigma B(-2\sigma a^2)\frac{(-6x^2y + 2y^3)}{(x^2+y^2)^3} \tag{8.8}$$

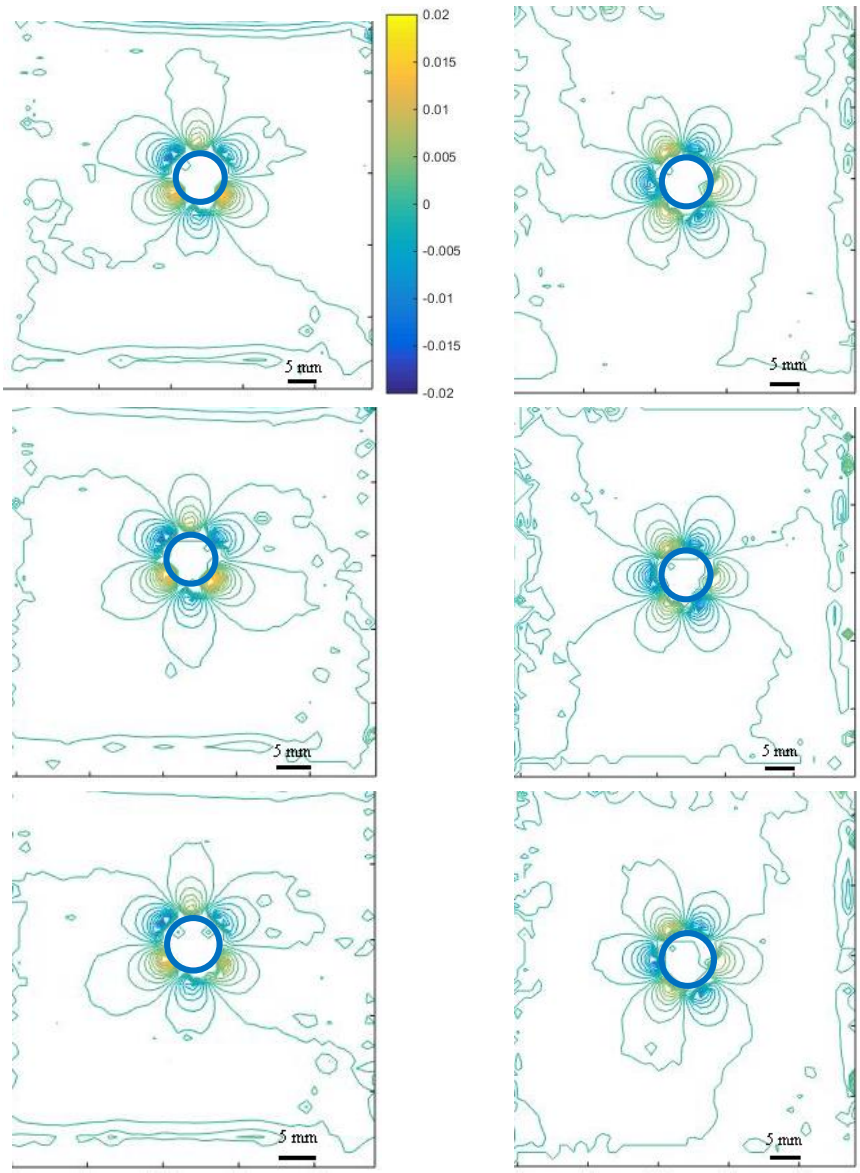

Figure 8.4: Measured ϕ_x (left) and ϕ_y (right) contours for a displacement of 1.3 mm at 0.02 (top), 0.2 (middle) and 2 mm/sec (bottom) respectively. Contour interval = $1x10^{-3}$ radian (blue circle represents the edge of the hole).

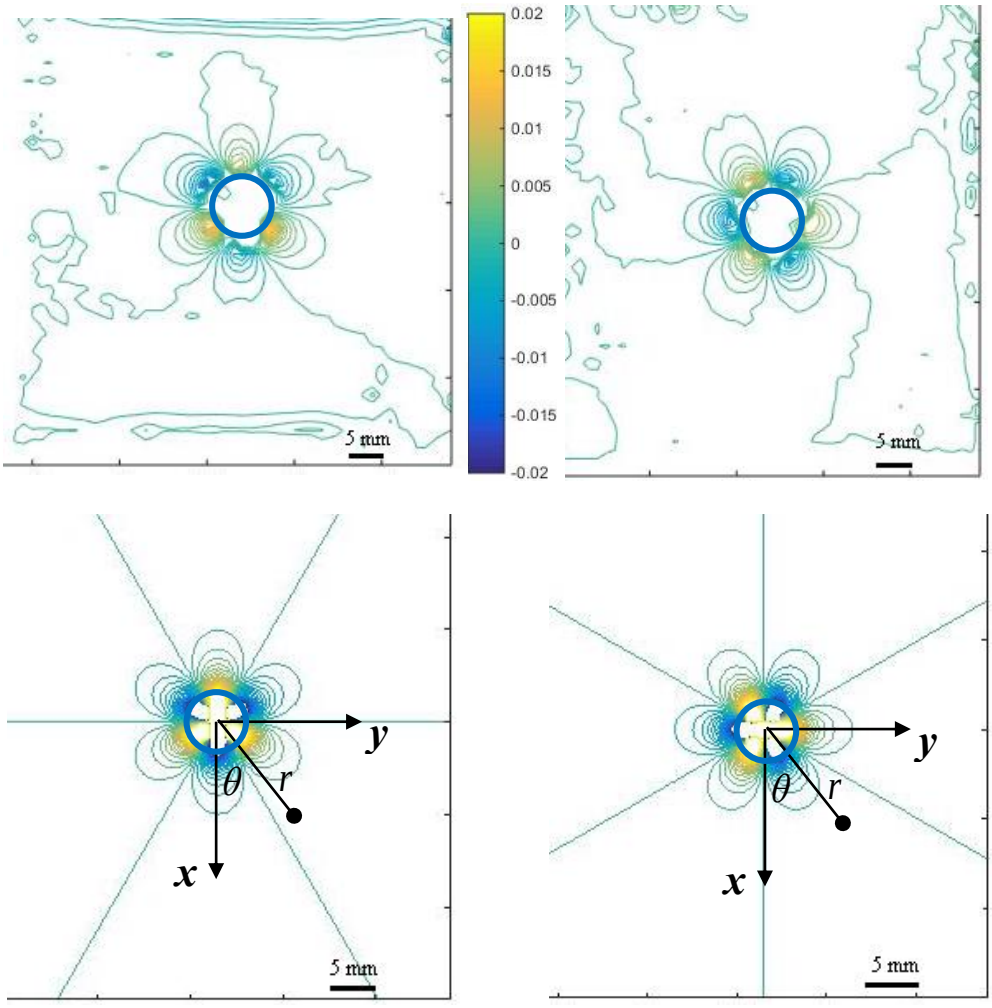

Figure 8.5: Comparison of experimental (top) and analytical (bottom) ϕ_x (left) and ϕ_y (right) contours for 0.02 mm/sec at a load F = 0.61 N. Contour interval = $1\text{x}10^{-3}$ rad.

From Fig. 8.5, there is good qualitative agreement between experimental and analytical contours. Hence, the stress concentration effects due to a hole in the tensile sheet can be studied in gels using DGS methodology.

Chapter 9: Puncture Simulations on Gel

In this chapter, mechanical response of the polymer gel during needle puncture is optically studied using DGS. Both insertion and retraction of a stiff needle into and out of the gel block are studied and the differences in the mechanics are identified. Details regarding sample preparation, experimental setup used, measurements made during insertion and retraction are included. The optical data of two orthogonal stress gradients from DGS are integrated to estimate thickness average stress data over the entire region of interest during both insertion and retraction.

9.1 Experimental details

Rectangular gel sheets devoid of air bubbles and good surface finish were prepared as discussed in the previous chapters. A hot-wire cutter was used to cut rectangular blocks of

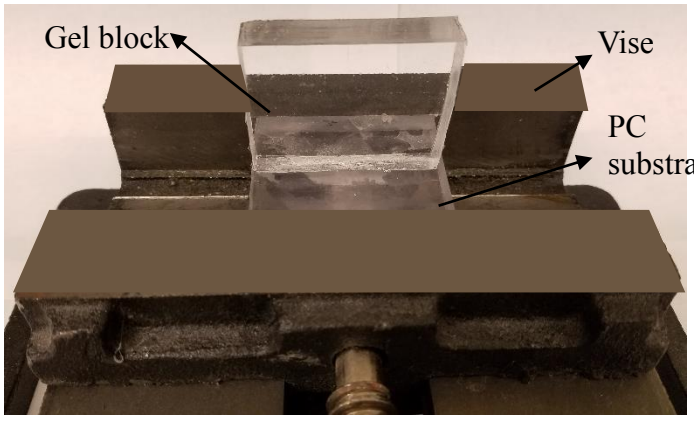

Figure 9.1: Photograph of a rectangular transparent block glued to a polycarbonate substrate and held in a bench vise.

dimensions 50 mm x 40 mm x 12.5 mm. As shown in Fig. 9.1, the bottom face of the gel block was glued to a polycarbonate substrate using Loctite 401 glue and secured in a mechanical vise for stability during penetration and retraction of the needle. A schematic of the experimental setup used for studying the puncture behavior of a planar polymer gel block is shown in Fig. 9.2. It consisted of a digital camera and a target plate painted with random black and white speckles placed at a distance Δ = 32 mm behind specimen mid-plane, as shown. The gel block was punctured using a long steel needle with a conical tip (diameter of shaft = 1.11 mm). The tests were performed at two different crosshead speeds, 0.02 and 2 mm/sec.

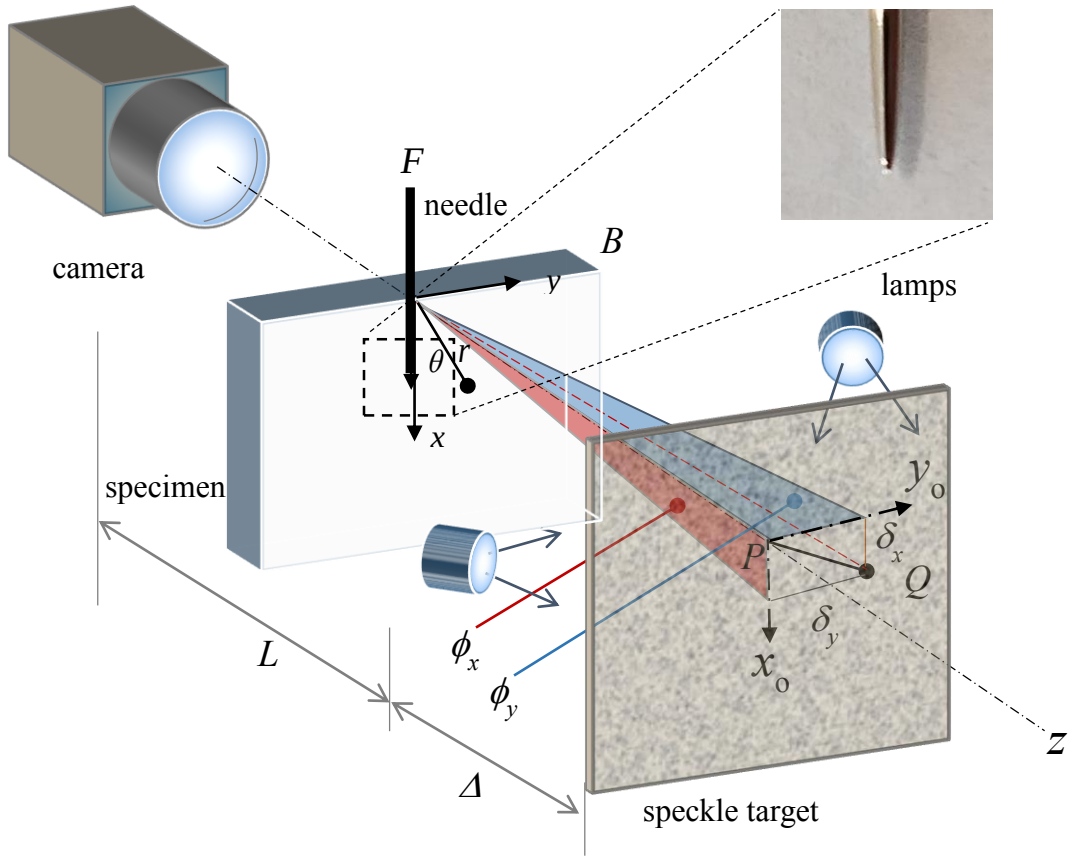

Figure 9.2: Schematic of the DGS setup used for studying puncture of a polymer gel block by a needle.

A Point Grey digital camera (Grasshopper3 GS3-U3-41C6M) fitted with a 18-108 mm focal length zoom lens was used to record images and was situated at a distance of approx. 540 mm from the specimen. The speckle pattern on the target plate was illuminated using two cool LED lamps. The digital camera was focused on the speckles through the rectangular gel sample. A reference speckle image was recorded before the sample was loaded. The needle held in the grips of the testing machine was inserted into the gel block and then retracted back to its original position at the two select crosshead speeds in two different experiments. Speckle images corresponding to various deformed states were recorded at regular time intervals (1-10 frames/sec) as the gel block was being penetrated. Figure 9.3 shows the gel block punctured by the needle at different amounts of displacements during insertion and retraction.

The digitized speckle images (2048 x 2048 pixels) recorded at different load levels were correlated subsequently with the one corresponding to the reference state using a digital image correlation software ARAMIS. As described in Chapter 6, an array of in-plane speckle displacements on the target plane (and hence the specimen plane) was evaluated and converted into local angular deflections of light rays ϕ_x and ϕ_y. A facet size of 125 x 125 pixels and step size of 85 pixels (scale factor = 0.025 mm/pixel and the data array size = 22 x 22) was used during analysis. As shown in Fig. 9.3, 'tenting' phenomenon described by Langevin et al., [19] was observed during different stages of needle insertion and reverse tenting was also observed during retraction.

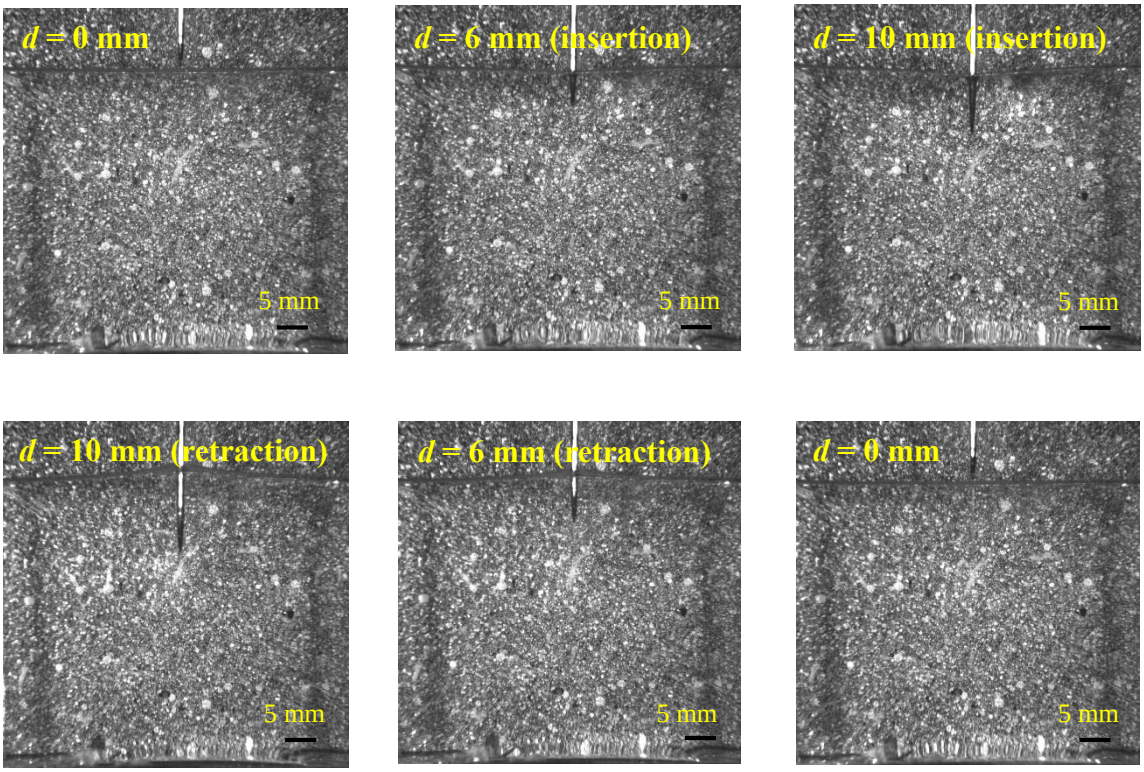

Figure 9.3: Speckle images photographed at different amounts of needle displacement during the experiment at 2 mm/sec crosshead speed.

9.2 Optical Measurements

When the deformed images of speckles were correlated with the undeformed image, displacement components δ_x and δ_y were obtained in the *x*- and *y*- directions, respectively. Knowing the gap between the specimen mid-plane and the target plate, the angular deflections ϕ_x and ϕ_y in the *x*-*z* and *y*-*z* planes were evaluated from δ_x and δ_y, respectively, and are proportional to stress gradients as given by Eqs. (6.4) and (6.5). Figure 9.4 shows the load-displacement responses during insertion and retraction at 2 mm/sec and 0.02 mm/sec. It can be observed that during insertion, the load is compressive, during retraction the load flips and becomes tensile before it finally reduces to zero when the

needle is completely retracted. In addition to rate effects, hysteresis is evident as well. Figures 9.5, 9.6 and 9.7, 9.8 show angular deflections (and hence stress gradient contours) for insertion and retraction at 2 mm/sec and 0.02 mm/sec, respectively:

$$\frac{\partial(\sigma_{xx}+\sigma_{yy})}{\partial x}=\frac{\phi_x}{C_\sigma B} \tag{9.1}$$

$$\frac{\partial(\sigma_{xx}+\sigma_{yy})}{\partial y}=\frac{\phi_y}{C_\sigma B} \tag{9.2}$$

If the angular deflections ϕ_x and ϕ_y are obtained from measurements, and elasto-optical constant C_σ and thickness *B* of the sample are known, then the thickness-average stress $(\sigma_{xx}+\sigma_{yy})$ can be evaluated using a suitable 2D integration scheme [55]. A few select thickness wise average stress distributions are shown in Figs. 9.9 and 9.10 as surface plots.

From Fig. 9.4, it can be observed that individual segments of the load vs needle displacement responses recorded during insertion at 0.02 mm/sec are relatively linear. In the 2 mm/sec case, on the otherhand, the corresponding segments are visibly nonlinear. Evidently there is much higher hysteresis at the faster needle displacement case.

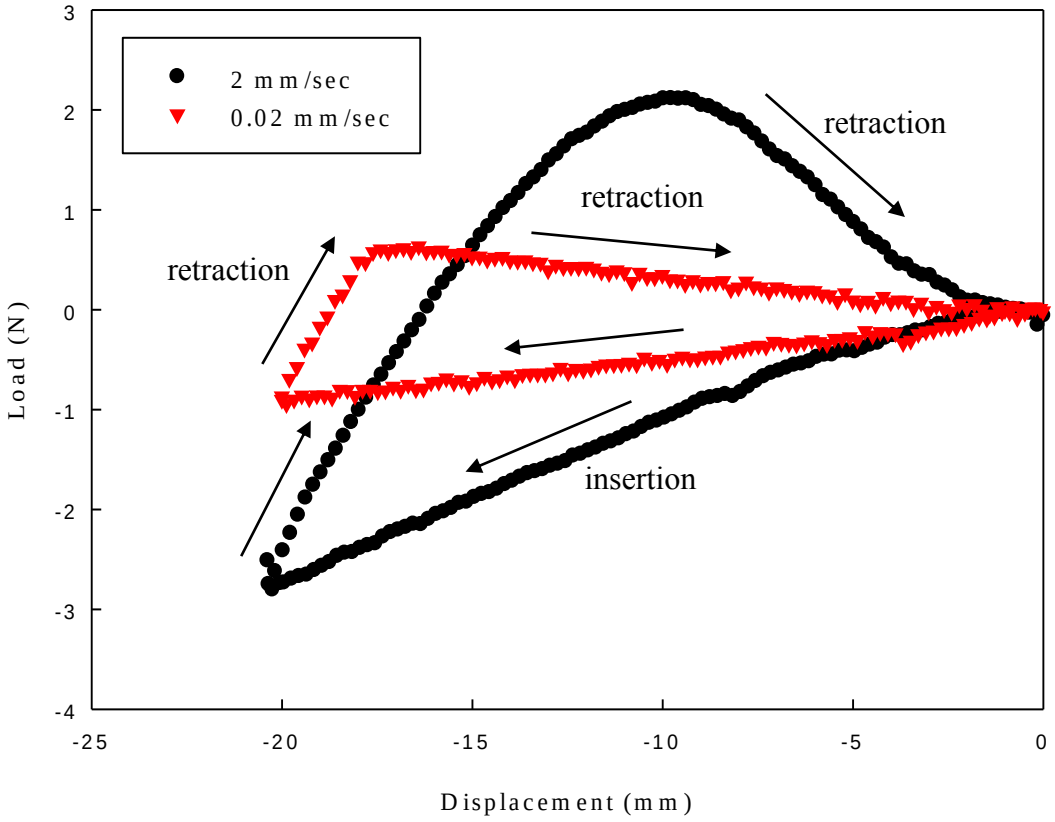

Figure 9.4: Load vs displacement responses to study puncture behavior caused due to a needle in a polymer gel block at 2 mm/sec and 0.02 mm/sec crosshead speeds.

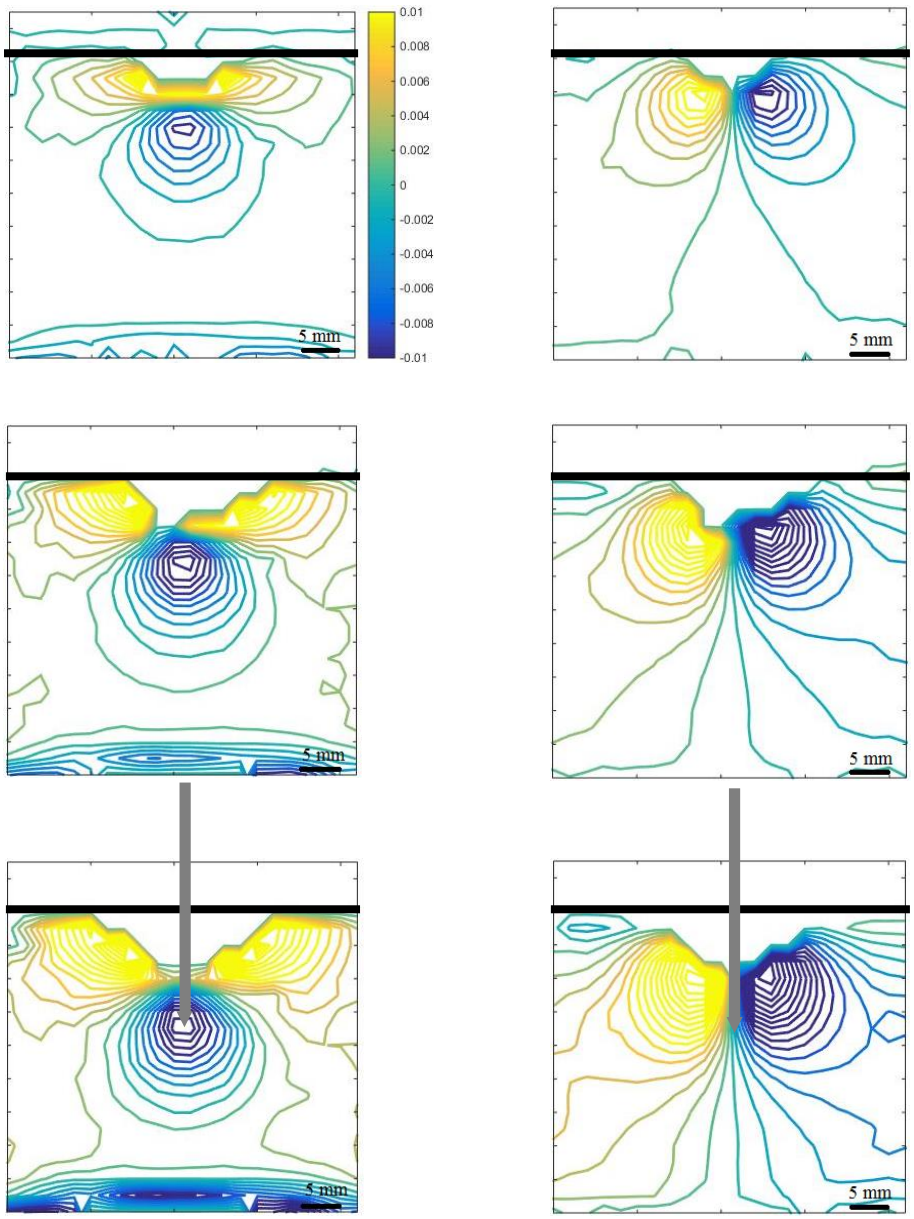

Figure 9.5: Measured ϕ_x (left) and ϕ_y (right) contours for 2 mm/sec insertion at 6 mm (top), 10 mm (middle) and 14 mm (bottom) depths respectively, with respect to the sample edge. Contour interval = 1.5 x 10^{-3} radians. Black horizontal line indicates sample edge.

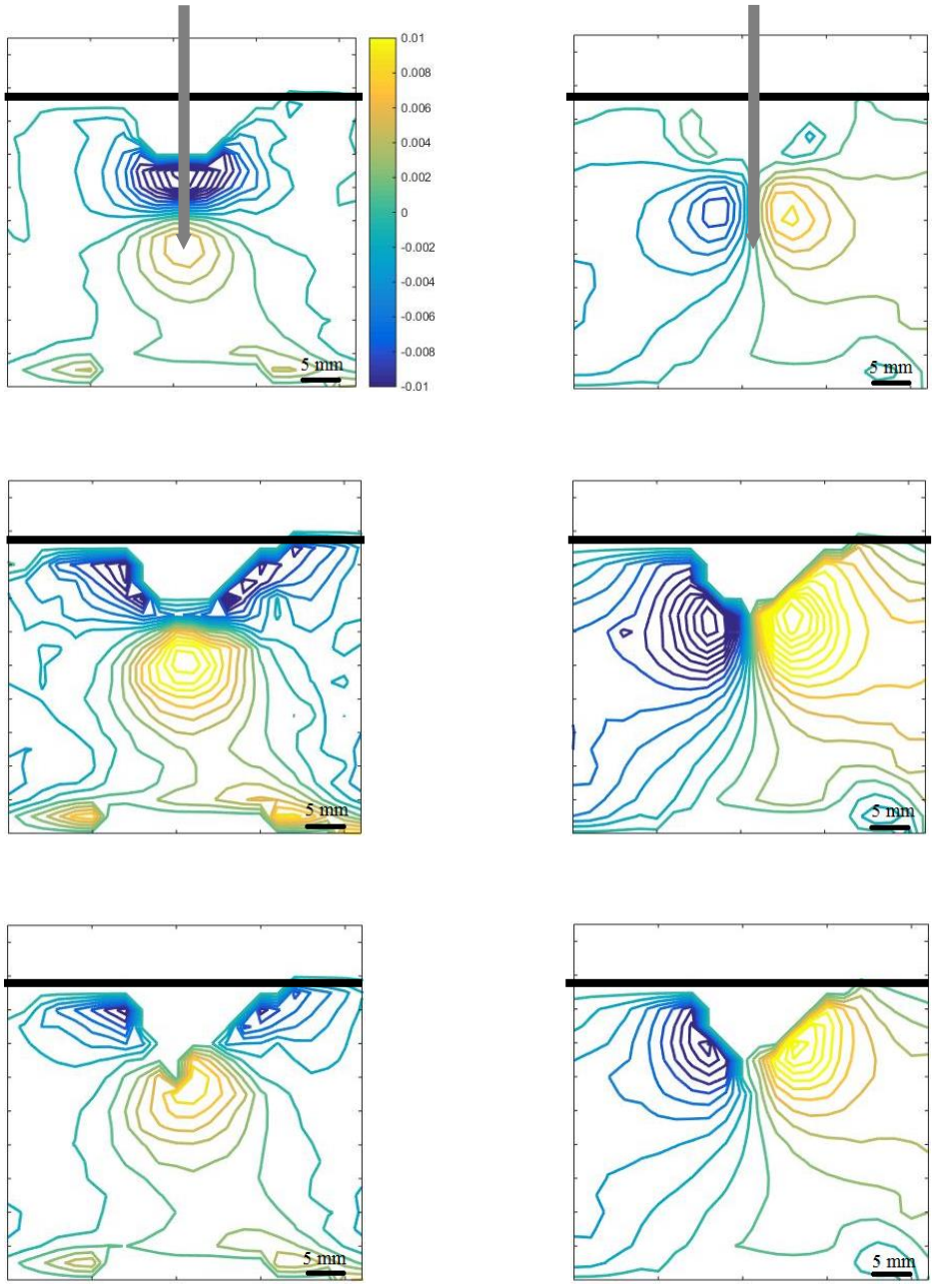

Figure 9.6: Measured ϕ_x (left) and ϕ_y (right) contours for 2 mm/sec retraction at 14 mm (top), 10 mm (middle) and 6 mm (bottom) depths respectively, with respect to the sample edge. Contour interval = 1.5 x 10^{-3} radians.

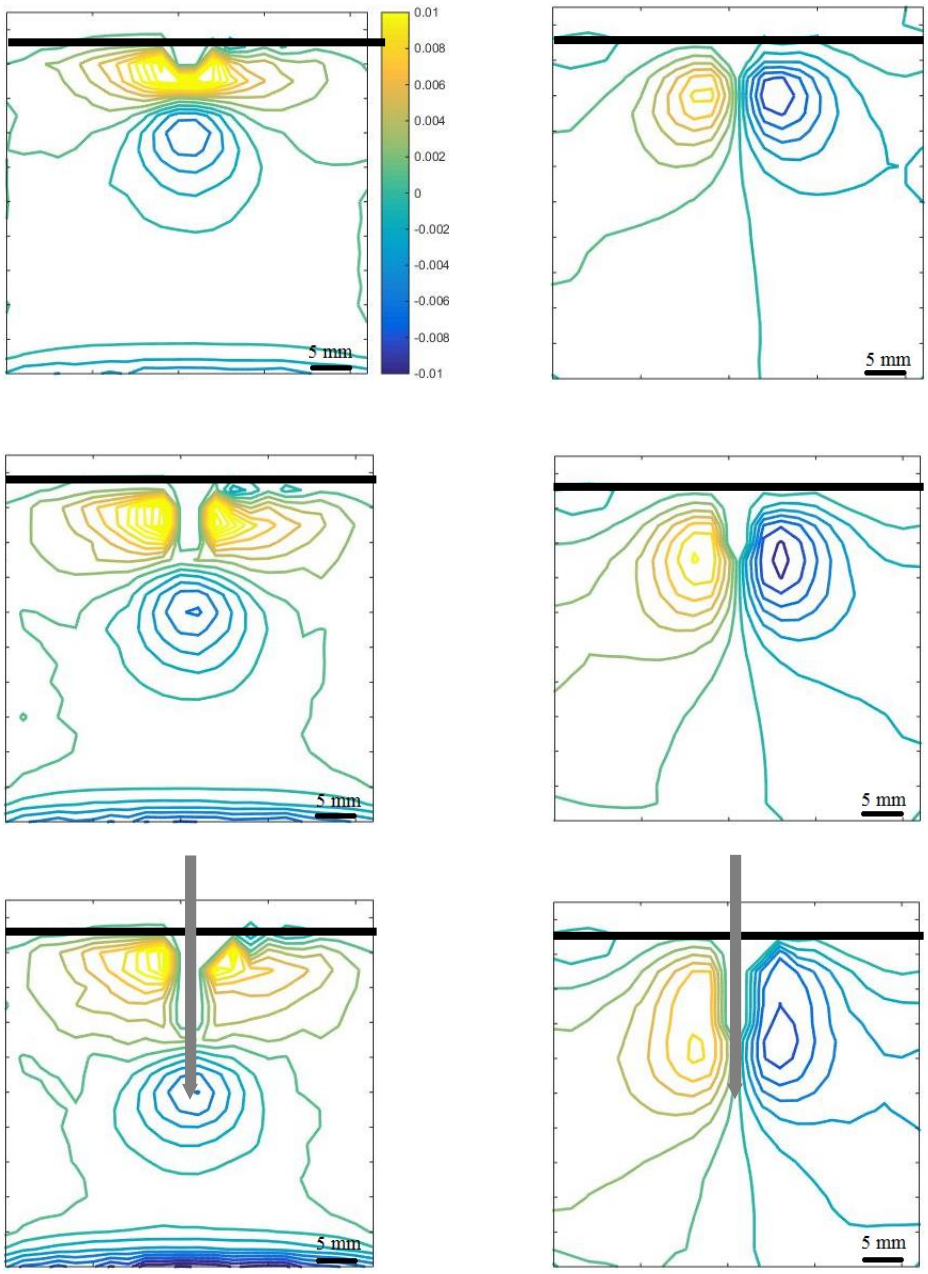

Figure 9.7: Measured ϕ_x (left) and ϕ_y (right) contours for 0.02 mm/sec at 6 mm (top), 10 mm (middle) and 14 mm (bottom) depths respectively, with respect to the sample edge. Contour interval = 1.5 x 10^{-3} radians.

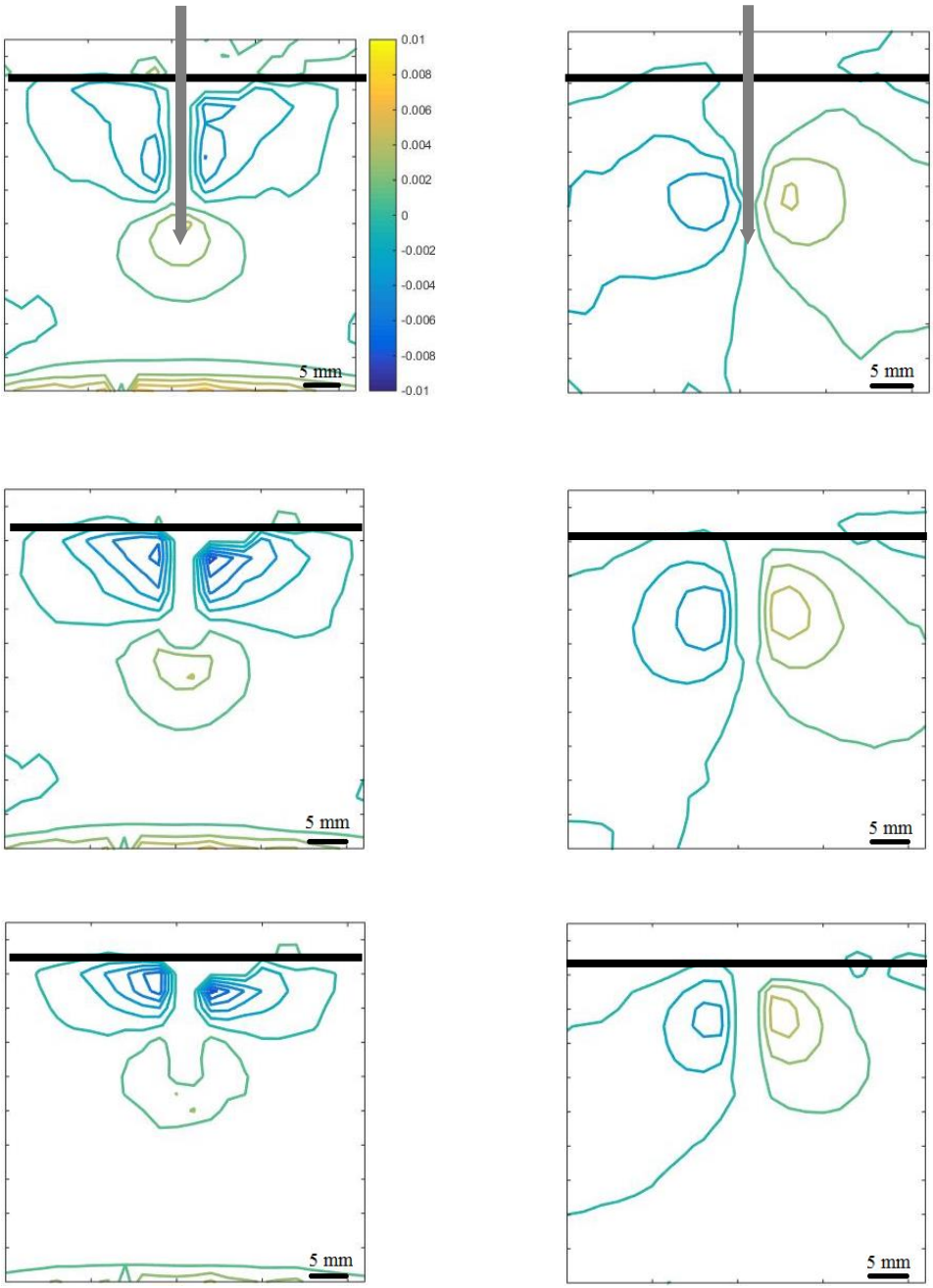

Figure 9.8: Measured ϕ_x (left) and ϕ_y (right) contours for 0.02 mm/sec at 14 mm (top), 10 mm (middle) and 6 mm (bottom) depths respectively, with respect to the sample edge. Contour interval = 1.5 x 10^{-3} radians.

During insertion, the compressive load varies monotonically with the needle displacement. From Figs. 9.5 and 9.7, during insertion, the density of angular deflection contours increases as the needle penetrates the gel block. Effect of the crosshead speed can be observed in terms of the number of contours in both the cases. On the other hand, during retraction, the compressive force diminishes before becoming tensile, reaching a maximum value before becoming zero. From Figs. 9.6 and 9.8, during retraction, initially the contour density is low, it increases when the needle is at an intermediate depth and finally when the needle tip comes close to the surface of the block, contour density reduces further. The positive contours ahead of the needle tip during retraction are more dominant at 2 mm/sec and can be attributed to a greater tensile force at this speed.

At 2 mm/sec, the deformation due to the needle in gel block is localized whereas at 0.02 mm/sec, the deformation is spread over a larger region near the needle. This is evident from the white regions in the contour plots where correlation was not achieved.

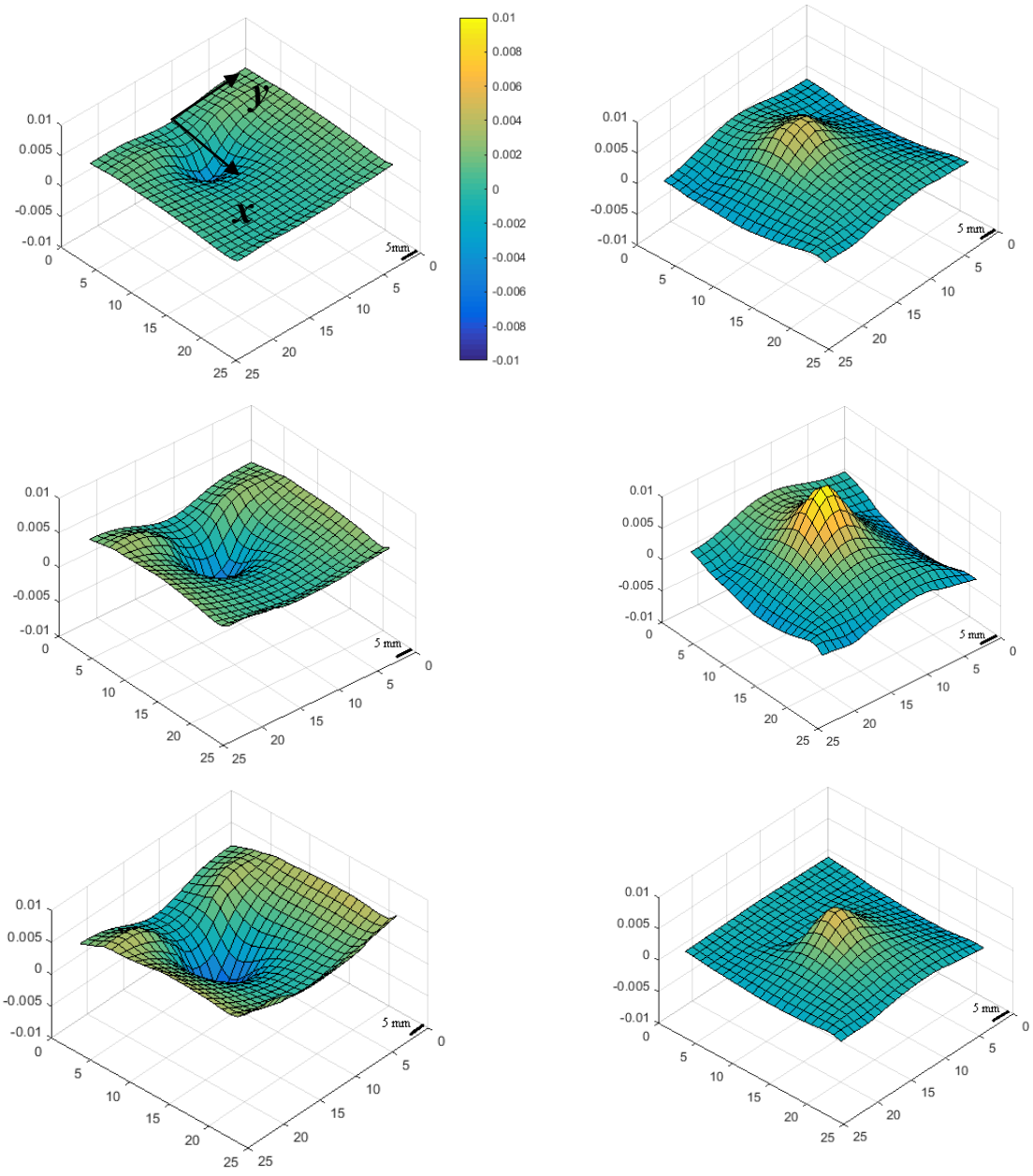

Figure 9.9: Measured $\left(\sigma_x + \sigma_y\right)$ (N/mm^2) values during insertion (left) and retraction (right) at 2 mm/sec at 6 mm (top), 10 mm (middle) and 14 mm (bottom) depths, respectively.

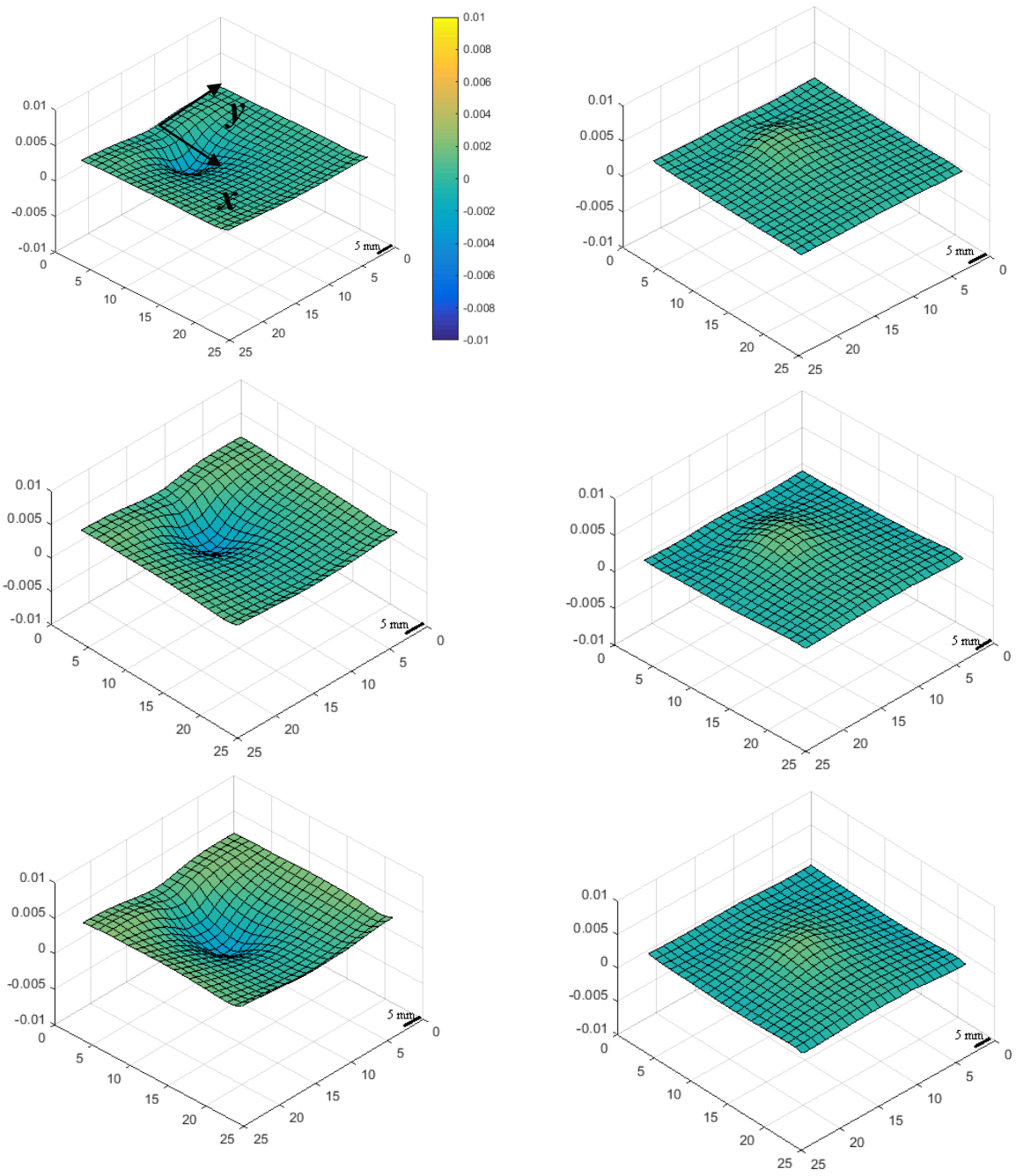

Figure 9.10: Measured $\left(\sigma_x + \sigma_y\right)$ (N/mm^2) values during insertion (left) and retraction (right) at 0.02 mm/sec at 6 mm (top), 10 mm (middle) and 14 mm (bottom) depths, respectively.

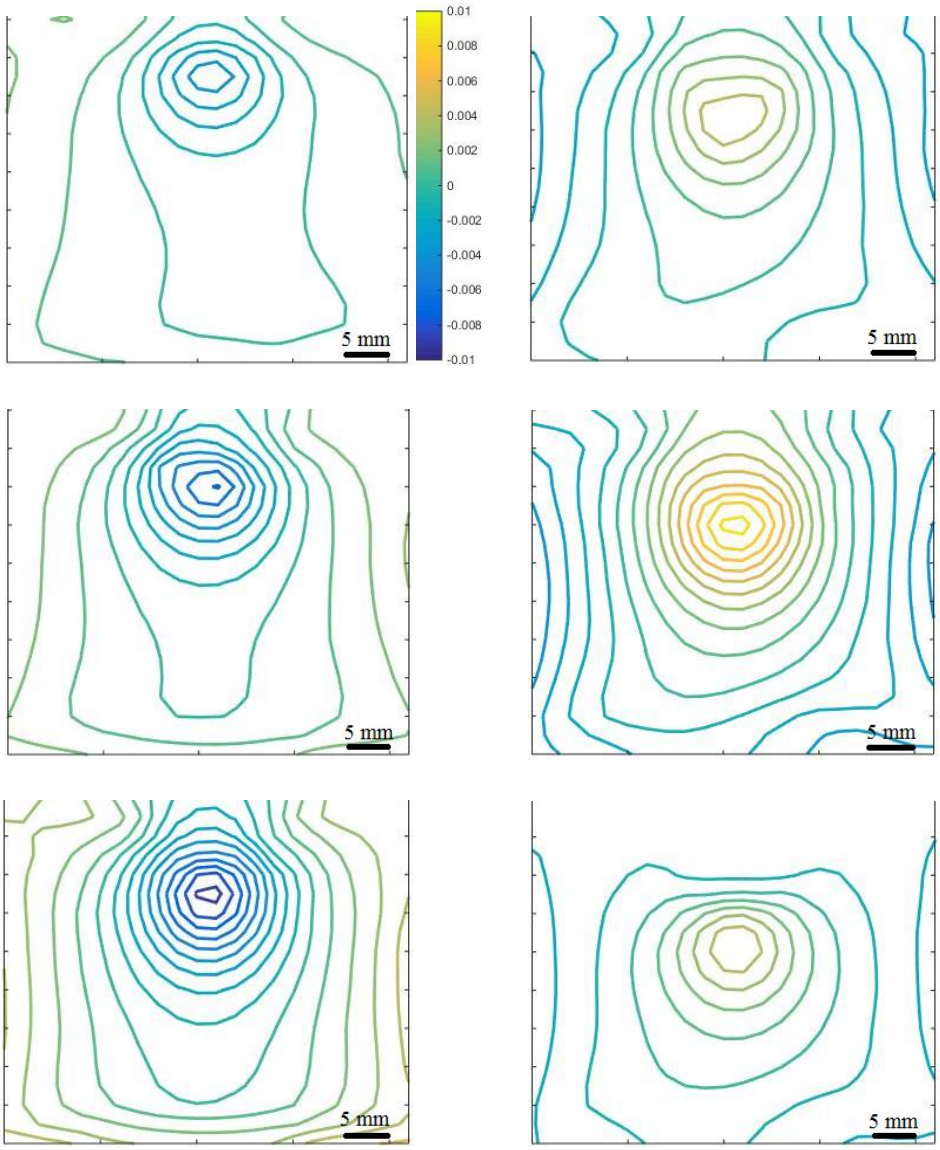

Figure 9.11: Measured $\left(\sigma_x + \sigma_y\right)$ (N/mm^2) contours during insertion (left) and retraction (right) at 2 mm/sec at 6 mm (top), 10 mm (middle) and 14 mm (bottom) depths, respectively. Contour interval = 1 x 10^{-3} MPa.

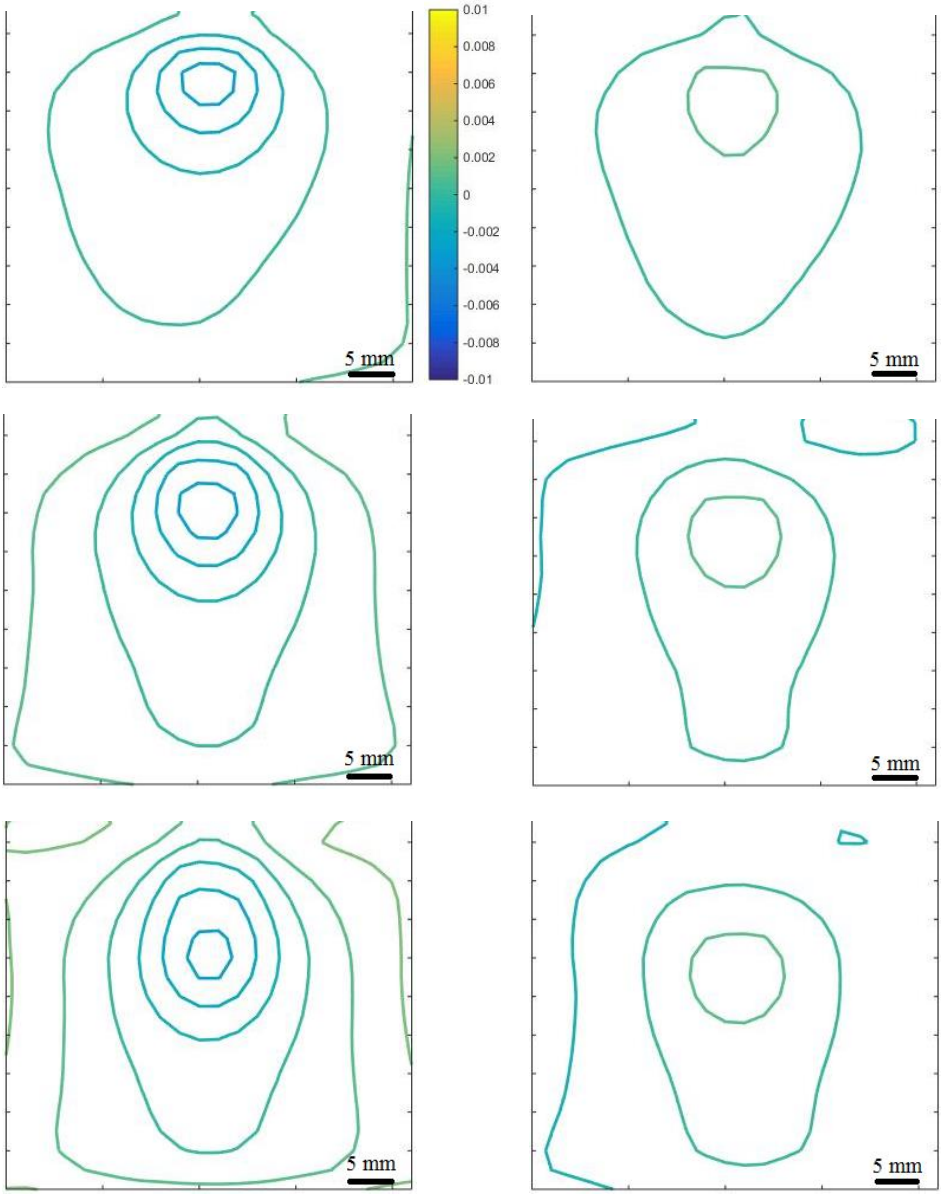

Figure 9.12: Measured $\left(\sigma_x + \sigma_y\right)$ (N/mm^2) contours during insertion (left) and retraction (right) at 0.02 mm/sec at 6 mm (top), 10 mm (middle) and 14 mm (bottom) depths, respectively. Contour interval = 1 x 10^{-3} MPa.

Via global measurements DiMaio et al., have noted that the load distribution is uniform along the needle shaft except for a peak value near the tip of the 17 G Tuohy needle used to puncture Poly Vinyl Chloride (PVC) tissue phantom [23]. In the case of polymer gel results shown in Figs. 9.9, 9.10 (surface contours) and Figs. 9.11, 9.12 (2D contours), the load distribution was rather non-uniform even along the shaft of the needle. The intensity of stress distribution increased as the needle penetrated further into the gel block. During retraction, initially the stress amplification is low, increases when the needle is at an intermediate depth and finally when the needle tip gets close to the surface of the block, the peak stress reduces. This phenomenon can observed more clearly in the 2 mm/sec case when compared to 0.02 mm/sec counterpart due to higher variation in stress with displacement.

Further, when the needle penetrates the gel block, compressive stresses occur ahead of the needle tip whereas close to the edge of the sample tensile stresses develop. During retraction, this phenomenon gets reversed; that is, tensile stresses occur ahead of the needle tip and compressive stresses close to the sample edge. During insertion, the material points are forced away from the needle, and the gel block experiences a compressive reaction force along the bottom edge of the sample and tensile stresses develop on the sides of the gel block. During retraction, this phenomenon is reversed. In addition, cutting, adhesion and frictional forces between the needle and the gel are also responsible for this complex behavior.

Chapter 10: Conclusions and Future directions

In this work, soft transparent polymer gel which can be used as a tissue simulant has been studied both mechanically and optically. Fourier Transform Infra-Red spectroscopy was used to determine the compositional match between the polymer gel and standard materials in the data bank. The gel had a relatively good match with Tygon tubing material.

Samples of different sizes and shapes were prepared using polycarbonate molds. Density of '10%' and '20%' polymer gels were measured as 844 and 867 kg/m^3, respectively. Refractive index of 10% and 20% polymer gel samples were determined using Abbe refractometer and were found to be 1.4728 and 1.4750, respectively. The mechanical behavior of 20% gel in uniaxial tension, compression, and shear were characterized at crosshead speeds of 0.02, 0.2 and 2.0 mm/sec. Strain energy density functions from popular hyperelastic models were used to model stress-strain resposnes. The method of 2D digital image correlation (DIC) was utilized to obtained orthogonal surface strains (axial and transverse) to determine the elastic parameters. MATLAB curve fitting tool box was employed to fit the measured data with Neo-Hookean, Money-Rivlin, Yeoh models to extract the elastic moduli and Poisson's ratios at different loading rates in tension, compression and shear. The Money-Rivlin model had the best goodnesss of fit. The elastic moduli thus determined were found to be in the range of 110 - 140 kPa. Further, the shear

modulus determined from independently conducted shear tests matched the ones based on elastic properties from tension tests. Both the ultimate stress and failure strain in tension increased with the crosshead speed. The latter behavior was unexpected when compared to responses of other common engineering materials.

The polymer gel studied was transparent and could be prepared with good surface finish. Hence, the feasibility of applying a full-field optical technique called Digital Gradient Sensing (DGS) to study stress fields under different loading configurations was explored. The DGS method is capable of measuring the combined effects of refractive index and thickness changes in planar solids as angular deflections of light rays. These measurements in turn can be related to two orthogonal in-plane stress gradients. Accordingly, a circular disk geometry subjected to diametral compression, widely studied in the photoelasticity literature, was adopted to determine the elasto-optical constant of the gel. The values were in the range of -1.18 to -1.47 mm^2/N for crosshead speeds of 0.02 to 2 mm/sec considered. That is, the magnitude of the elasto-optical constant decreased with the crosshead speed.

These property measurements were used to demonstrate the usefulness of the gel used in conjunction with the optical methodology to simulate a few conventional stress concentration problems such as a line-load acting on the edge of a polymer gel block (the Flamant problem) and a uniaxial tensile sheet with a circular cut-out. Experimental measurements in each case were compared with the analytical counterparts. Finite element analysis of the Flamant problem incorporating measured Mooney-Rivlin characteristics was also successfully carried out.

Lastly, the mechanics of a needle puncturing a soft tissue surrogate was examined optically using the gel and DGS. The evolution of thickness average stress gradients in the gel during insertion and retraction phases was attempted. The measured stress gradients were also integrated and stress magnitudes were mapped in the region of interest. The problem on hand being severely 3D in nature, the observations made were somewhat limited. A non-uniform distribution of stresses along the needle shaft and near the needle tip vicinity was observed. The stresses also showed a reversal of stresses from being compressive at the tip during insertion to tension during retraction, the latter being somewhat unexpected.

10.1 Potential Future Directions

Some of the potential topics for future research are as follows:

The research during this research primarily focused on low rates of loading. The behavior of the polymer gel under dynamic loading conditions is yet to be explored. The highly compliant nature of the polymer gel with vastly differing longitudinal and shear wave speeds would likely offer numerous scientific opportunities to understand soft tissue response at high strain rates.

Another area that requires consideration is debonding of the polymer gel from a higher stiffness material (say, polycarbonate or PMMA) to mimic the mechanics of separation of muscle from bone.

Growth and cavitation of air bubbles in polymer gel is also of significant interest to simulate tissue trauma during impact and shockwave loading events.

Applications of polymer gel to simulate the mechanics of needle-tissue interactions involving inhomogenieties and at different loading conditions play a vital role in solving complex problems relevant to the biomedical field. For example, puncturing a polymer gel block cast with multiple layers of different density polymer gels could mimic inhomogeneous tissue response.

References:

1. Peterson, B. "Ballistic Gelatin Lethality Performance of 0.375-in Ball Bearings and MAAWS 401B Flechettes." Army Research Laboratory Technical Report. ARL-TR-4153. (2007).
2. Fackler, M. L., and Dougherty, P. J. "Theodor Kocher and the scientific foundation of wound ballistics." Surgery, Gynecology, and Obstetrics 172:153–160 (1991).
3. Maiden, N. "Historical overview of wound ballistics research." Forensic science, medicine, and pathology 5.2: 85-89 (2009).
4. Juliano, T. F., Forster, A.M., Drzal, P.L., Weerasooriya, T., Moy, P., and VanLandingham, M.R. "Multiscale mechanical characterization of biomimetic physically associating gels." Journal of materials research 21.08: 2084-2092 (2006).
5. Wen, Y, Xu, C., Wang, S. and Batra, R.C. "Analysis of behind the armor ballistic trauma." Journal of The Mechanical Behavior of Biomedical Materials 45: 11-21 (2015).
6. Sallaway, L., Magee, S., Shi, J., Lehmann, O., Quivira, F., Tgavalekos, K., Brooks, D.H., Muftu, S., Meleis, W., Moore, R.H. and Kopans, D. "Detecting Solid Masses in Phantom Breast Using Mechanical Indentation." Experimental Mechanics 54.6: 935-942 (2014).
7. MacPherson, D., Bullet penetration: Modeling the dynamics and the incapacitation resulting from wound trauma. Ballistic, El Segundo, California, USA (2005).

8. Nicholas, N. C., and Welsch, J. R. Institute for Non-Lethal Defense Technologies Report: Ballistic Gelatin. Pennsylvania State Univ University Park, Applied Research Lab, (2004).
9. Moy, P., Weerasooriya, T., and Gunnarsson, C. A. "Tensile deformation of ballistic gelatin as a function of loading rate." Proceedings of the XI International Congress and Exposition June. Vol. 2. No. 5. (2008).
10. Subhash, G., Liu, Q., Moore, D. F., Ifju, P. G., & Haile, M. A., Concentration dependence of tensile behavior in agarose gel using digital image correlation. Experimental Mechanics, 51(2), 255-262 (2011).
11. Nguyen, C. T., & Vu-Khanh, T., Mechanics and mechanisms of puncture by medical needles. Procedia Engineering, 1(1), 139-142 (2009).
12. Misra, S., Reed, K.B., Schafer, B.W., Ramesh, K.T. and Okamura, A.M. "Mechanics of flexible needles robotically steered through soft tissue." The International Journal of Robotics Research (2010).
13. Okamura, A. M., Simone, C., and Leary, M. "Force modeling for needle insertion into soft tissue." Biomedical Engineering, IEEE Transactions on 51.10: 1707-1716 (2004).
14. Rosen, J., Hannaford, B., MacFarlane, M.P. and Sinanan, M.N. "Force controlled and teleoperated endoscopic grasper for minimally invasive surgery-experimental performance evaluation."Biomedical Engineering, IEEE Transactions on 46.10: 1212-1221 (1999).
15. Jiang, S., Li, P., Yu, Y., Liu, J. and Yang, Z. "Experimental study of needle–tissue interaction forces: effect of needle geometries, insertion methods and tissue characteristics."Journal of Biomechanics 47.13: 3344-3353 (2014).

16. Jiang, S., Liu, S., and Feng, W. "PVA hydrogel properties for biomedical application." Journal of the Mechanical Behavior of Biomedical Materials 4.7: 1228-1233 (2011).
17. Mahvash, M., and Dupont, P. E. "Mechanics of dynamic needle insertion into a biological material." Biomedical Engineering, IEEE Transactions on 57.4: 934-943 (2010).
18. Van Gerwen, D. J., Dankelman, J. and van den Dobbelsteen, J. J. "Needle–tissue interaction forces–A survey of experimental data." Medical Engineering & Physics 34.6: 665-680 (2012).
19. Langevin, H. M., Churchill, D.L., Fox, J.R., Badger, G.J., Garra, B.S. and Krag, M.H. "Biomechanical response to acupuncture needling in humans." Journal of Applied Physiology 91.6: 2471-2478 (2001).
20. Kobayashi, Y., Onishi, A., Hoshi, T., Kawamura, K. and Fujie, M.G. "Modeling of conditions where a puncture occurs during needle insertion considering probability distribution." Intelligent Robots and Systems, 2008. IROS 2008. IEEE/RSJ International Conference on. IEEE, (2008).
21. Hing, J. T., Brooks, A. D. and Desai, J. P. "Reality-based needle insertion simulation for haptic feedback in prostate brachytherapy." Robotics and Automation, 2006. ICRA 2006. Proceedings 2006 IEEE International Conference on. IEEE, (2006).
22. Hing, J. T., Brooks, A. D. and Desai, J. P. "A biplanar fluoroscopic approach for the measurement, modeling, and simulation of needle and soft-tissue interaction." Medical Image Analysis 11.1: 62-78 (2007).

23. DiMaio, S. P., and Salcudean, S. E. "Needle insertion modeling and simulation." Robotics and Automation, IEEE Transactions on 19.5: 864-875 (2003).
24. Griffiths, P. R., and De Haseth, J. A. Fourier transform infrared spectrometry. Vol. 171. John Wiley & Sons, (2007).
25. Stuart, B. Infrared spectroscopy. John Wiley & Sons, Inc., (2005).
26. GOM mbH, ARAMIS v6.1 User Manual, Germany (2009).
27. Pickerd, V. Optimisation and Validation of the ARAMIS Digital Image Correlation System for Use in Large-scale High-strain-rate Events. No. DSTO-TN-1203. Defense Science And Technology Organization Victoria (Australia) Maritime Platforms Division, (2013).
28. Green, A. E, and Adkins, J. E., Large Elastic Deformations, Oxford University Press, (1970).
29. Malvern, L. E., Introduction to the Mechanics of a Continuous Medium, Prentice-Hall, (1969).
30. Ogden, R. W., Nonlinear Elastic Deformations, Dover (1998).
31. Macosko, C. W., Rheology: Principles, Measurement and Applications, VCH Publishers (1994).
32. Mooney, M. "A Theory of Large Elastic Deformation." Journal of Applied Physics 11.9: 582-592 (1940).
33. Rivlin, R. S. "Large elastic deformations of isotropic materials. IV. Further developments of the general theory." Philosophical Transactions of the Royal Society of London A: Mathematical, Physical and Engineering Sciences241.835: 379-397 (1948).

34. Yeoh, O. H. "Some forms of the strain energy function for rubber." Rubber Chemistry and Technology 66.5: 754-771 (1993).

35. Inc, A. N. S. Y. S. ANSYS Theory Manual, Release 12.0." (2009).

36. Mendis, K. K., Stalnaker, R. L. and Advani, S. H. "A constitutive relationship for large deformation finite element modeling of brain tissue." Journal of Biomechanical Engineering 117.3: 279-285 (1995).

37. Lally, C., Reid, A. J., and Prendergast, P. J. "Elastic behavior of porcine coronary artery tissue under uniaxial and equibiaxial tension." Annals of Biomedical Engineering 32.10: 1355-1364 (2004).

38. Hu, T., and Desai, J. P. "Characterization of soft-tissue material properties: Large deformation analysis." Medical Simulation. Springer Berlin Heidelberg, 28-37 (2004).

39. Casem, D. T., Dwivedi, A.K., Mrozek, R.A. and Lenhart, J.L. "Compression response of a thermoplastic elastomer gel tissue surrogate over a range of strain-rates." International Journal of Solids and Structures 51.11: 2037-2046 (2014).

40. Kwon, J. and Ghatu S. "Compressive strain rate sensitivity of ballistic gelatin." Journal of Biomechanics 43.3: 420-425 (2010).

41. Periasamy, C., and Tippur, H. V. A Full-Field Digital Gradient Sensing Method for Evaluating Stress Gradients in Transparent Solids, Applied Optics, Vol. 51, No. 12, pp 2088-2097 (2012).

42. Dally, J. W. and Riley W. F., Experimental Stress Analysis, College House Enterprises (2005).

43. Berenbaun, R. and Brodie, I., "Measurement of the Tensile Strength of Brittle Materials," British J. Applied Physics, 10, 281-287 (1959).

44. Shaw, M.C., Braiden, P.M., and DeSlavo, G.J., "The Disk Test for Brittle Materials," J. Engineering for Industry, 77-87 (1975).
45. Shetty, D. K., Rosenfield, A. R., and Duckworth, W. H. "Mixed-mode fracture in biaxial stress state: application of the diametral-compression (Brazilian disk) test." Engineering Fracture Mechanics 26.6: 825-840 (1987).
46. Dong, S., Wang, Y. and Xia, Y. "Stress intensity factors for central cracked circular disk subjected to compression." Engineering Fracture Mechanics 71.7: 1135-1148 (2004).
47. Sadd, M. H., Elasticity – Theory, Applications and Numerics, Academic Press (2009).
48. Budynas, R. G. Advanced strength and applied stress analysis, McGraw-Hill (1998).
49. Tippur, H. V., and Periasamy, C. "A digital gradient sensing method for evaluating orthogonal stress gradients in transparent solids subjected to mechanical loads." SPIE Optical Engineering+ Applications. International Society for Optics and Photonics, (2012).
50. Systèmes, Dassault. ABAQUS 6.12 Theory manual. Dassault Systèmes Simulia Corp., Providence, Rhode Island (2012).
51. Andersson, H. "Stress-intensity factors at the tips of a star-shaped contour in an infinite tensile sheet." Journal of the Mechanics and Physics of Solids, 17.5: 405-406 (1969).
52. Yan, X. "Rectangular tensile sheet with single edge crack or edge half-circular-hole crack." Engineering Failure Analysis, 14.7: 1406-1410 (2007).
53. Mallick, P. K. "Effects of hole stress concentration and its mitigation on the tensile strength of sheet moulding compound (SMC-R50) composites."Composites 19.4: 283-287 (1988).

54. Roylance, D. "Closed-Form Solutions." (2001).

55. Miao, C., and Tippur, H. V. “Measurement of orthogonal surface gradients and reconstruction of surface topography from digital gradient sensing method,” Proceedings of SEM XIII International Congress, Orlando, FL, paper #181, (2016).